Swansea University

Master of Science Thesis

Numerical Modelling of Membrane filtration using Lattice Boltzmann and Finite Volume Methods

Author:
Mahendra Paipuri

Supervisor:
Professor Oubay Hassan

A thesis submitted in partial fulfilment of the requirements for the degree of Master of Science

in the

Zienkiewicz Centre for Computational Engineering (ZC2E)
College of Engineering

June 2014

Declaration of Authorship

I, Mahendra Paipuri, declare that this thesis titled, 'Numerical Modelling of Membrane filtration using Lattice Boltzmann and Finite Volume Methods' and the work presented in it are my own. I confirm that:

- A declaration that the work has not previously been accepted in substance for any degree and is not being concurrently submitted in candidature for any degree.
- A statement that the thesis is the result of your own investigations, except where otherwise stated and that other sources are acknowledged by footnotes giving explicit references and that a bibliography is appended.
- A statement that the student gives consent for the thesis, if accepted, to be available for photocopying and for inter-library loan, and for the title and summary to be made available to outside organisations.

Signed: _____

Date: _____

Simulations are believed by no one except those who conducted them.

Experimental results are believed by everyone except those who conducted them.

Anonymous

SWANSEA UNIVERSITY

Abstract

College of Engineering

Master of Science

Numerical Modelling of Membrane filtration using Lattice Boltzmann and Finite Volume Methods

by Mahendra PAIPURI

The importance of simulations in membrane filtration is discussed. Various models in the literature to simulate different phenomena in membrane filtration like cake formation, osmotic pressure and rejection of salts are briefly reviewed. The origin of Lattice Boltzmann methods from kinetic theory is discussed along with its implementation details. Implementing finite volume scheme to solve convection diffusion equation is discussed in detail along with different differencing schemes used to discretize convective terms on the faces of control volume. The idea of coupling both fluid and solute particles to simulate the membrane filtration process is discussed. Different approaches in implementing coupling between LB-LB and LB-FV for solving fluid and solute particle respectively is discussed. DSPM-DE model is briefly discussed in the context of salt rejection estimation for nano-filtration membranes. Concentration polarisation is taken into account in the rejection modelling by coupling DSPM-DE with solute distribution over the membrane surface. Finally, results of various models are presented and compared to experimental data wherever appropriate.

Acknowledgements

I would like to express my profound gratitude to Professor Oubay HASSANfor being my thesis supervisor. He has been very helpful in guiding me and encouraging me to learn new things, without which, this thesis would not have been possible.

I am thankful to Professor Nidal Hilal for his valuable inputs and support during the thesis.

I am also thankful to European Commission for sponsoring this Erasmus Mundus Master Program and also to International Centre for Numerical Methods in Engineering (CIMNE), Barcelona for forming such wonderful curriculum.

I would also like to thank my course mates Carles and Farhad and other friends for making my stay in Swansea memorable.

I owe my loving thanks to my family and friends. Without their encouragement and understanding it would have been impossible for me to finish this work.

Contents

List of Figures

List of Tables

Abbreviations

MF	**M**icro **F**iltration
UF	**U**ltra **F**iltration
NF	**N**ano **F**iltration
RO	**R**everse **O**mosis
CP	**C**oncentration **P**olarisation
DSPM	**D**onnan **S**etric **P**ore **M**odel
CFD	**C**omputational **F**luid **D**ynamics
CDE	**C**onvection **D**iffusion **E**quation
LBM	**L**attice **B**oltzmann **M**ethod
LB	**L**attice **B**oltzmann
DSPM-DE	**D**onnan **S**etric **P**ore **M**odel **D**ielectric **E**xclusion
PDE	**P**artial **D**ifferential **E**quation
NS	**N**avier **S**tokes
FEM	**F**inite **E**lement **M**ethod
FDM	**F**inite **D**ifference **M**ethod
FVM	**F**inite **V**olume **M**ethod
MD	**M**olecular **D**ynamics
DPD	**D**issipative **P**article **D**ynamics
SPH	**S**moothed **P**article **H**ydrodynamics
RHS	**R**ight **H**and **S**ide
BGK	**B**hatnagar **G**ross **K**rook
EDF	**E**quilibrium **D**istribution **F**unction
FEM	**F**inite **E**lement **M**ethod
LHS	**L**eft **H**and **S**ide

BC	**B**oundary **C**ondition
QUICK	**Q**uadratic **U**pwind **S**treaming **I**nterpolation **C**onvective **K**inetics
TVD	**T**otal **V**ariational **D**iminishing
CV	**C**ontrol **V**olume
OZ	**O**rnstein **Z**ernike
HNC	**H**ypernetted **N**etted **C**hain
PY	**P**ercus **Y**evick
CFL	**C**ourant **F**riedrichs **L**evy
TMP	**T**rans **M**embrane **P**ressure
DLVO	**D**erjaguin **L**andau **V**erwey **O**verbeek
ODE	**O**rdinary **D**ifferential **E**quation

Physical Constants

Universal gas constant	R	=	$8.314\ JK^{-1}$
Constant in Carmen-Kozeny relation	C	=	5
Porosity of randomly packed cake layer	ϵ_e	=	0.4
Boltzmann constant	k	=	$1.34 \times 10^{-23}\ m^2Kgs^{-2}K^{-1}$
Hamaker constant	A	=	$1.65 \times 10^{-21}\ J$
Electronic charge	e	=	$1.6 \times 10^{-19}\ C$
Dielectric constant of water	ϵ_b	=	78.6
Dielectric constant of vaccum	ϵ_0	=	$8.834 \times 10^{-19}\ Fm^{-1}$
Avagadro constant	N_A	=	6.023×10^{23}
Faraday constant	F	=	$9.6485 \times 10^4\ Am^{-1}$

Symbols

ΔP	Applied pressure	Pa
ΔP_c	Critical pressure	Pa
ρ	Density	Kgm^{-3}
$\mathbf{u}$	Velocity vector	ms^{-1}
t	Time	s
$\mathbf{x}$	Position vector	m
p	Pressure	Pa
τ^s	Stress tensor	Pa
e	Internal energy	J
$\mathbf{b}$	Body force	N
$\dot{q}$	Heat source	J
ΔP_c	Critical pressure	Pa
$\mathbf{p}$	Momentum	Ns
f	Particle distribution function	
N	Number of molecules	
$\mathbf{F}$	External force	N
f^{eq}	Equilibrium distribution function	
T	Temperature	K
Dm	Dimension in space	
τ	Relaxation time	
$\mathbf{e}_\alpha$	Direction vector	
w_α	Weights of lattice	
ϵ	Knudsen number	

L	Mesoscopic length scale	m
L_h	Macroscopic length scale	m
c_s	Speed of sound	
ν	Kinematic viscosity	$m^2 s^{-1}$
$\mathbf{x}_f$	Fluid lattice node	
$\mathbf{x}_w$	Boundary wall lattice node	
$\mathbf{x}_b$	Boundary lattice node	
χ	Weight in curved boundary treatment in LBM	
R_m	Membrane resistance	m^{-1}
ϕ	Conservative field variable	
V	Volume of control volume	m^3
A	Area of face of control volume	m^2
$\mathbf{n}$	Normal vector to the face of control volume	
ϕ_W	West control node	
ϕ_E	East control node	
ϕ_N	North control node	
ϕ_S	South control node	
ϕ_w	West face of control node	
ϕ_e	East face of control node	
ϕ_n	North face of control node	
ϕ_s	South face of control node	
Δx	Grid spacing in x-direction	m
Δy	Grid spacing in y-direction	m
F	Convective flux	$m^3 s^{-1}$
Γ	Diffusive flux	$m^3 s^{-1}$
Pe	Peclet number	
S_u	Source term	$m^3 s^{-1}$
η	Dynamic viscosity	Pas
η_0	Dynamic viscosity of pure solvent	Pas
R_c	Specific cake resistance	m^{-2}
$\dot{\gamma}$	Shear rate	s^{-1}

a	Radius of solute particle	m
$\Delta\Pi$	osmotic pressure	Pa
σ_0	Reflection coefficient	
n	Number density of solute particles	
$g(r)$	Radial distribution function	
$E(r)$	Interaction energy	J
η	Dynamic viscosity	Pas
$h(r)$	Total correlation function	
$c(r)$	direct correlation function	
z_p	Charge number on solute particle	
κ	Inverse Debye screening length	m^{-1}
C_{EL}	Concentration of background electrolyte	M
$K(\phi)$	Sedimentation coefficient	
$D(\phi)$	Gradient diffusion coefficient	
$Z(\phi)$	Osmotic compressibility	
C_p	Permeate concentration	$molem^{-3}$
C_w	Wall concentration	$molem^{-3}$
C_b	Bulk concentration	$molem^{-3}$
R	Rejection coefficient	
c_i	Pore concentration of i^{th} ion	$molem^{-3}$
J_v	Flux	ms^{-1}
K_i	Convective hindrance factor of i^{th} ion	
D_i	Diffusive hindrance factor of i^{th} ion	
z_i	Valency of $i^{th}ion$	
ψ	Potential	V
λ_i	Steric hindrance factor of i^{th} ion	
$r_{i,s}$	Radius of $i^{th}ion$	m
r_p	Pore radius	m
ϕ_i	Steric partition coefficient	
$\Delta\psi_D$	Donnan exclusion potential	V
ΔW_i	Dielectric exclusion energy	J

ϵ_p	Dielectric constant of pore	Fm^{-1}
X_d	membrane charge density	$molem^{-3}$
Re	Reynolds number	
ζ	Zeta potential of membrane	V

Dedicated to my parents and well wishers

Chapter 1

Introduction

1.1 Filtration and its importance

Filtration is one of the most important processes in the present industrial world. According to the study conducted by Dr. E. Rabinowicz of M.I.T., presented at the American Society of Lubrication Engineers, Bearing Workshop, in 1981, 70% of components replacements are due to surface degradation. In hydraulic and lubricating systems, 20% of these replacements result from corrosion, with 50% resulting from mechanical wear. Proper filtration reduces the wear in a fluid system, thereby extending machine parts lifetime. Also, minimising wear reduces the maintenance costs of the plant and helps the system to achieve high performance levels. Apart from this, filtration process is the backbone in several important processes like waste-water management, treatment of drinking water etc. Scarcity of fresh water in certain parts of the world driving people to look for alternative sources. Desalination is one of the attractive techniques to produce fresh water for human consumption and irrigation. Economically, it is expensive than the conventional sources but it is one of the few rainfall-independent water sources.

The most common forms of desalination are distillation, ion exchange process and membrane process. Distillation involves heating the salt water above its boiling temperature, capturing the steam and condensing it. In ion exchange process, cations and anions in the salt water are exchanged for carbonate cations and calcium anions which can be precipitated leaving behind fresh water. Distillation involves high energy consumption while ion exchange process is not suitable for feed water with high salt concentration. Membrane filtration can be seen as a

process which can address these limitations. In the subsequent sections membrane filtration is discussed in brief.

1.2 Membrane filtration

Membrane filtration involves the flow of feed over a semi-permeable membrane where the solute particles bigger than the pore size of the membrane are trapped allowing only clean water. There are two types of membrane filtration namely dead end and cross flow membrane filtration. They are illustrated in the Fig. 1.1. Cross-flow has the feed flow in the tangential direction to membrane surface while the dead-end filtration has the flow normal to the membrane surface.

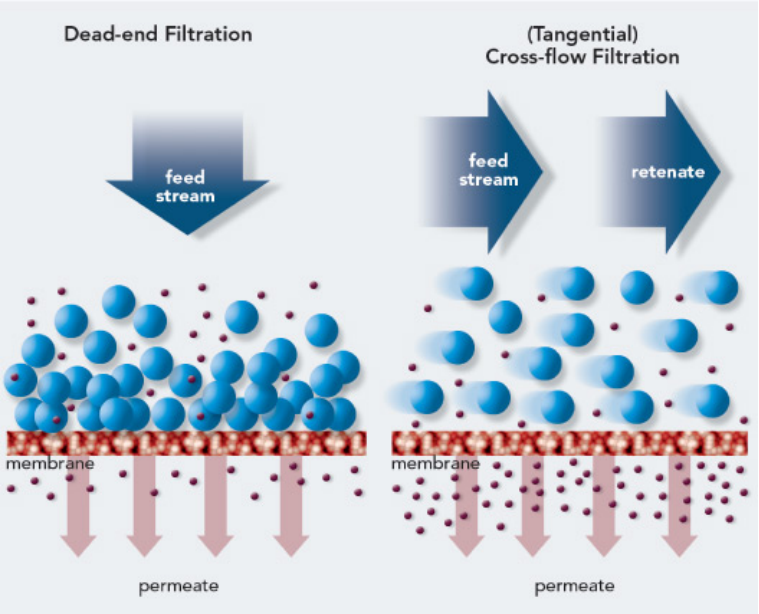

FIGURE 1.1: Dead end and cross-flow filtration

Cross-flow has the obvious benefit over dead end filtration in the performance of the filtration process. Membrane filtration can also be classified based on the type of solute particles the membrane surface retain. Microfiltration (MF), Ultrafiltration (UF), Nanofiltration (NF) and Reverse Osmosis (RO) are common types. The differences in operating conditions are tabulated in Table 1.1

RO can remove almost all of the dissolved salts, but the operating pressure is quite high which involves high energy consumption. On the other hand, NF can remove most of divalent ions and some of monovalent ions and can be operated at much lower pressures. This makes NF an attractive option for desalination process. It is also used in many other processes like waste-water management, ground

TABLE 1.1: Characteristics of Membrane processes

Process	Size of particles (microns)	Operating Pressure (psi)	Applications
RO	0.0001-0.001	400-1200	Dewatering
NF	0.001-0.01	100-600	Desalination
UF	0.01-1	25-150	Purification of suspended solids,macromolecules
MF	1-10	20-150	Bacteria removal

water treatment, removal of natural organic matter etc. Therefore, optimization of membrane filtration process like NF is an active research area and at the same time a huge challenge.

A major limiting factor in membrane filtration is formation of Concentration Polarisation (CP) and cake layer. Feed water passing through the membrane exerts a drag force on the solute particles bringing them to the membrane surface. These particles are rejected and retained near the membrane surface. As clean water is passed through the membrane pores, the concentration of solute particles become higher near the membrane surface as compared to the concentration in the bulk solution as shown in Fig.1.2.

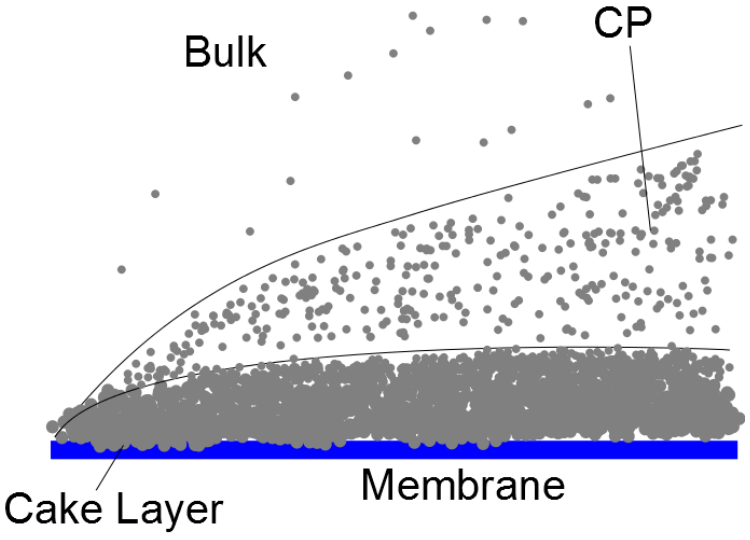

FIGURE 1.2: Concentration Polarisation and Cake Layer formation

The concentration of the solute particles is highest near the membrane surface and decreases with the distance away from the surface. This concentration gradient causes the solute to go back to the bulk solution based on the Fick's law of diffusion. The back transport of solute is an interesting phenomenon as it can be by

several ways. Some of them are shear-induced diffusion, Brownian diffusion and inertial lift. The way solute particles diffuse depends on its size. In addition to diffusion, another transport mechanism is cross-flow. The feed cross-flow can take the particles away from membrane by convection mechanism. Peclet number is an important parameter quantifying the relative strength of convection and diffusion. Cake layer can be formed near membrane surface in absence of sufficient diffusion of solute particles. It severely deteriorates the flux through the membrane. Although concentration polarisation decreases the performance of the membrane, it is a temporary phenomenon and disappears when filtration stops. But this is not the case with cake layer and it is a permanent phenomenon. Special treatments of membrane surface is needed to get rid of cake layer.

Another important phenomenon in membrane filtration process is osmotic pressure. Due to the development of polarized layer over the membrane surface, an osmotic pressure is created due to difference of concentration of water on the opposite sides of membrane. Osmotic pressure acts opposite to applied pressure and decreases the net flux coming out of the membrane. Song [1] developed a parameter critical pressure which is determined solely from the thermodynamics properties of the solution. This represents the maximum value of osmotic pressure at a given critical filtration number (N_{FC}) for non-interacting particles. If the driving pressure was smaller than the critical pressure ($\Delta P < \Delta P_c$) the colloidal particles would not deposit and concentration polarization would be the dominating mechanism. On the other hand if the driving pressure were greater than the critical pressure, cake formation would occur and the concentration polarization layer above it would be at maximal value ΔP_c.

A lot of experiments are being conducted in membrane filtration to study the phenomenon of concentration polarisation and cake layer and to optimize the process. Experimental study of membrane characteristics is generally very complex and time consuming procedure. A typical experimental procedure consists of determining the size of solute particle, treating solute particles with an appropriate solvent and treating membranes. This process usually takes long time and each experiment with different input parameters needs a lot of work. Therefore, one obvious replacement for this is development of computational models. In the following section, different models developed for membrane

1.3 Membrane filtration models

Flux prediction and rejection prediction are two important parameters in modelling a full-scale laboratory experiments. Flux prediction is important when the organic and inorganic solute particles are involved. These particles tend to form cake layer severely deteriorating flux through membrane. When the solute particles are ions, tendency of the cake layer formation is almost zero. This can be attributed due to charge effects between ions and membrane surface and relatively small size of ions when compared to pore size of the membrane. Rejection is amount of solute particles that are retained by the membrane surface. This is one of the important factors in studying the characteristics of different NF membranes. There are different models developed to predict flux and rejection.

1.3.1 Membrane pore models

The performance of NF membranes depends on pore size (steric effect) and effective charge density (Donnan effect) of the semi-permeable membrane. The fundamental relationship governing the transport of ionic species through membrane pores is the extended Nernst-Planck equation. Tsuru et al. [2] first proposed the model based on extended Nernst-Planck equation to describe the transport of the ions through membrane pores. This model included the convective, diffusive and electrostatic effects of ions in solution. Bowen [3] developed a model to account for steric effects along with charge effects. It uses the extended Nersnt-Planck equation at membrane surface and hindered nature of transport inside the membrane pores. Later, Bowen et al. [4] developed Donnan-steric-pore model (DSPM) that takes the hindrance effects for diffusion and convection flow inside the membrane pores.

These models were successful in predicting the rejection of dissolved salts in NF to a good accuracy. One apparent drawback of these models is inability to predict the permeate flux. Permeate flux depends on the concentration on feed side and permeate side of the membrane by Vant Hoff equation. Several models assume that the membrane wall concentration is same as the bulk concentration which is valid only when the bulk concentration is very dilute. But when bulk concentration is high, concentration polarisation should be taken into account. These models consider the concentration of the ions is same all along the length of the membrane surface. But in theory, due to the existence of concentration polarisation layer the concentration varies over the length of the membrane. Another complication

arises when multi-component salts where the rejection coefficient and concentration polarisation are coupled phenomenon. For instance, a mixture of monovalent and bivalent salts in NF process will exhibit different rejection ratios. Therefore, concentration polarisation models were developed to address this limitation.

1.3.2 Concentration polarisation models

Concentration polarisation models deal with predicting the concentration of solute and permeate flux along the length of membrane in the polarised layer. This model solves steady-state convection diffusion equation with appropriate boundary conditions. The variation of the flux along the length is obtained by use of either thermodynamic (osmotic pressure model) or hydrodynamic (filtration theory) approaches. In the absence of cake layer, the above mentioned approaches yield same result.

Bhattacharjee et al. [5] coupled concentration polarisation model with membrane pore model to predict both permeate flux and ion rejection in NF membranes. They could predict axial dependence of ion rejection and flux along the membrane length. The analytical and semi-analytical models available in literature are formulated by simplifying governing equations which makes them easy to study the effects of different parameters on the performance of membrane systems.

Kim et al. [6] developed an analytical model which predicts the flux taking into account the solute-solute interactions. Their model is cell based which depends on the distance between the solute particles at the balance of different interaction forces. This model assumes a fixed structure for concentration polarisation while computing interactions. The model developed by Bhattacharjee et al. [7] overcome this limitation. In this model they incorporated the interaction forces into diffusion coefficient and osmotic pressure by use of statistical mechanics. None of these models take cake layer into consideration and hence valid for only dilute solutions. Another limitation of these models is they do not account the hydrodynamic effects of feed flow. Concentration polarisation and cake layer formation affects the crossflow which influences permeate flux. Some of the above mentioned limitations can be addressed by using CFD models. Most of the above stated models uses a simplified form of convection-diffusion equation (CDE). The simplification are made upon some assumptions that made possible to obtain a closed form of solution to CDE. Therefore, these models are not robust and cannot be applied to every filtration process.

1.3.3 CFD models

Development of a model with widespread applicability to membrane systems requires robust techniques like CFD. There have been few attempts at modelling membrane systems in CFD. This is due to the complexity of the problem and the fact that empirical approaches described previously are computationally very efficient. However, CFD models are needed if the flow in complex geometries, which include recirculation, are to be studied.

Huang and Morrissey [8] used the finite element technique to solve for the concentration field with an approximate solution to velocity field while Lee [9] did a similar analysis using finite difference scheme. Hansen et al. [10] used a spectral method to solve Navier-Stokes equation for cross-flow and it can be applied to complex geometries easily. Geraldes et al. [11] used finite volume simulations for crossflow for a simple channel flow. They solved both flow and concentration fields but they needed very fine mesh to get grid independent solution.

The main advantage of doing a CFD analysis is able to predict the permeate flux for complex geometries and optimize the design to achieve higher flux. Empirical models assume a fixed structure for cake formation and concentration polarisation. CFD techniques can be used to predict the shape of cake layer and its thickness which could be an important parameter in studying the fouling. The apparent drawback in these models is the computational cost. Extremely refined meshes are needed near membrane surfaces as cake layer and concentration polarisation layer are thin compared to filter dimensions. Modelling of solute-solute interactions, Donnan and steric effects is quite difficult with the CFD approach.

Kromkamp et al. [12] developed a model for micro-filtration using Lattice Boltzmann methods (LBM) which is based on kinetic theory of gases to predict both hydrodynamics of crossflow and concentration polarisation. This model solves Navier-Stokes equation for crossflow hydrodynamics and convection-diffusion equation for solute back-transport mechanism.The method has the added advantage of dealing with complex geometries and multiphase flow. LB schemes can be implemented on a parallel computer relatively easily which increases the computational efficiency.

1.4 Objectives of the research

The objective of this study is to model the membrane filtration process using appropriate numerical techniques. After doing an extensive study of above stated models, LBM model proposed by Kromkamp et al. is chosen. The reason for this choice is the simplicity of LBM formulation and its robustness. This model simulates the filtration process by solving solute and fluid in a coupled manner . The details of this coupling will be explained in the subsequent chapters. Therefore, this model can be considered as the extension of Kromkamp's micro-filtration model to nano-filtration making appropriate changes. The development of this framework can be split into following components:

- Validate the implemented LBM code for micro-filtration with the results of Kromkamp et al.
- Implement a osmotic pressure governed model for interacting solute particles in nano-filtration
- Validate the implemented osmotic pressure NF model with the results available in the literature.
- Implement a cake predicting model for nano-filtration using coupled Lattice Boltzmann methods and finite volume techniques.
- Validate the cake model for nano-filtration with some experimental data available in the literature
- Implement a rejection prediction model in nano-filtration for ionic salts using DSPM-DE model
- Validate the results of DSPM-DE model with experimental results by fitting necessary parameters from experimental data

1.4.1 Thesis layout

This thesis is divided into 6 chapters. The description of each chapter is given below

Chapter 1 deals with some of important phenomena governing cross-flow membrane filtration process. Various models to simulate the filtration process are discussed in a brief literature review followed by objectives of the research.

Chapter 2 discusses the theory of Lattice Boltzmann methods. It starts with a very brief introduction to various techniques in CFD and briefs about the kinetic theory of gases. Evolution of Lattice Boltzmann methods from kinetic theory of gases is given. The implementation procedure of LBM is discussed in detail along with implementation of different types of boundary conditions in LBM.

Chapter 3 gives the theory of finite volume methods and the implementation details of finite volume schemes for solving convection diffusion equation. Different types of differencing schemes for convective term are discussed.

Chapter 4 discusses the different implementation strategies using LB schemes and finite volume techniques to model different cases in micro-filtration and nano-filtration given in the objectives of the research.

Chapter 5 discusses the results of the implemented models. The chapter starts with results of benchmark problems used to validate the both LB and finite volume solvers followed by results of different cases in micro-filtration and nano-filtration.

Chapter 6 discusses the remarks that can be made on the different models in terms of their versatility, applicability and shortcomings. The scope for additional research and further development are given.

Chapter 2

Theory of Lattice Boltzmann methods

2.1 Computational fluid dynamics (CFD)

Computational fluid dynamics is the study of transport phenomenon by solving the partial differential equations (PDEs) using appropriate numerical methods. Over the past five decades several methods have been proposed to solve Navier-Stokes (NS) equations in discrete space and time. A brief overview of traditional CFD is discussed.

For Newtonian fluids, the NS equations in Einstein notation are given as follows:

$$\frac{\partial \rho}{\partial t} + \frac{\partial (\rho u_i)}{\partial x_i} = 0 \tag{2.1}$$

$$\frac{\partial (\rho u_i)}{\partial t} + \frac{\partial (\rho u_i u_j)}{\partial x_j} = -\frac{\partial p}{\partial x_i} + \frac{\partial \tau^s_{ij}}{\partial x_j} + \rho b_i \tag{2.2}$$

$$\frac{\partial (\rho e)}{\partial t} + (\rho e + p)\frac{\partial u_i}{\partial x_i} = \frac{\partial (\tau_{ij} u_j)}{\partial x_i} + \rho b_i u_i + \frac{\partial (\dot{q}_i)}{\partial x_i} \tag{2.3}$$

where ρ is density of fluid, u_i is the velcoity in i^{th} direction, τ^s_{ij} is stress tensor, b_i is body force, e is internal energy, $\dot{q}$ is heat source. Eq. 2.1 is mass conservation, Eq. 2.2 is conservation of momentum and Eq. 2.3 is energy conservation. Eq. 2.2

is obtained by using Newton's second law which is conservation of momentum to a control volume. When combined with conservation of mass and energy, these equations describe the bulk transport of the macroscopic properties of a fluid.

Finite difference methods (FDM), finite element methods (FEM) and finite volume methods are most popular in numerical discretization techniques. The idea of FDM is to approximate derivatives using Taylor's series. Forward difference, backward difference and central difference being most common. FDM works best with a regular grid when the geometry is highly structured. In FEM the solution is calculated in all the elements in the domain using basis functions. The accuracy of the solution is highly dependent on the basis functions. However, FEM are not locally conservative and also have stability issues in compressible flows. The most popular and successful technique in CFD is finite volume method (FVM). In this method, the whole domain is subdivided into control volumes. By applying divergence theorem to transport equations yields the discretised equation which is the flux balance equation. It can applied to unstructured geometries and various kinds of PDEs. But the limitation is implementation of higher order schemes (higher than second order) is difficult in FVM.

All these techniques use NS equations which are considered as macroscopic view of fluid flow. Unlike the above methods, there exits microscopic methods like Molecular Dynamics (MD) simulations, Dissipative Particle Dynamics method (DPD), Smoothed Particle Hydrodynamics (SPH) and Lattice Boltzmann methods (LBM) etc.

2.2 Lattice Boltzmann methods (LBM)

In the last two decades, the Lattice Boltzmann methods (LBM) have emerged as a promising tool for modelling fluid flow problems. It is fundamentally based on kinetic theory of gases which is explained in detail in subsequent sections.

2.2.1 Kinetic Theory of Gases

In a dilute gas where particles are moving at high velocity, it would be possible to know the dynamic state of the system by knowing the position vector ($\mathbf{x}$) and momentum ($\mathbf{p}$) of each individual particle at some instant in time. By using classical mechanics principles, using the present state of the system future states can be predicted. A system can be described by a distribution function $f^N(\mathbf{x}^N, \mathbf{p}^N, t)$

where N is the number of particles. The function f is the distribution function of a particle occupying the space with co-ordinates given by $\mathbf{x}$ at time t with a momentum of ($\mathbf{p}$). This level of description is not practical as there will be as many as 10^{23} molecules in a litre of any gas at atmospheric conditions. Also, the interactions at the microscopic level are not of much practical importance when considering the bulk effect.

To overcome the above stated shortcomings, concept of ensemble is used in first order distribution functions. The distribution $f^1(\mathbf{x}, \mathbf{p}, t)$ gives the probability of finding a particle with a given position and momentum and the positions and momenta of the remaining molecules need not be specified. This is the single particle distribution function.

The probability of number of molecules with positions between $\mathbf{x} \pm \mathbf{dx}$ and momentum $\mathbf{p} \pm d\mathbf{p}$ is given by $f^1(\mathbf{x}, \mathbf{p}, t)d\mathbf{x}d\mathbf{p}$. Let an external force $\mathbf{F}$ that is small relative to intermolecular forces is applied to the system. At time $t + dt$, the new positions of molecules starting at $\mathbf{x}$ are $\mathbf{x} + \mathbf{dx}$ and the new momenta are $\mathbf{p}$ + d$\mathbf{p}$. Thus, when the positions and momenta are known at a particular time t, incrementing them allows us to determine f^1 at a future time $t + dt$.

$$f^1(\mathbf{x} + d\mathbf{x}, \mathbf{p} + d\mathbf{p}, t + dt)d\mathbf{x}d\mathbf{p} = f^1(\mathbf{x}, \mathbf{p}, t)d\mathbf{x}d\mathbf{p} \tag{2.4}$$

There are however collisions that result in some points starting at ($\mathbf{x}$, $\mathbf{p}$) not arriving at ($\mathbf{x}$ + d$\mathbf{x}$, $\mathbf{p}$+ d$\mathbf{p}$) and some not starting at ($\mathbf{x}$, $\mathbf{p}$) arriving there too. We set $\Gamma^{(-)}d\mathbf{x}d\mathbf{p}dt$ equal to the number of molecules that do not arrive in the expected portion of phase space due to collisions during time dt. Similarly, we set $\Gamma^{(+)}d\mathbf{x}d\mathbf{p}dt$ equal to the number of molecules that start somewhere other than (x, p) and arrive in that portion of phase space due to collisions during time dt. If we start with Eq. 2.4 and add the changes in f^1 due to these collisions we obtain

$$f^1(\mathbf{x} + d\mathbf{x}, \mathbf{p} + d\mathbf{p}, t + dt)d\mathbf{x}d\mathbf{p} = f^1(\mathbf{x}, \mathbf{p}, t)d\mathbf{x}d\mathbf{p} + [\Gamma^{(+)} - \Gamma^{(-)}]d\mathbf{x}d\mathbf{p}dt \tag{2.5}$$

Using Taylor series expansion for LHS in Eq. 2.5 gives the Boltzmann equation. The velocity vector is denoted by $\boldsymbol{\xi}$ in Eq. 2.6.

$$\boldsymbol{\xi} \cdot \nabla_{\mathbf{x}} + \mathbf{F} \cdot \nabla_{\mathbf{p}} f^1 + \frac{\partial f^1}{\partial t} = \Gamma^{(+)} - \Gamma^{(-)} \tag{2.6}$$

2.2.2 Discretization of the Boltzmann Equation

A brief overview of time and space discretization of the Boltzmann equation is given here. For detailed explanation, Li-Shi [13] work can be referred.

In the Boltzmann equation, Eq. 2.6, the collision operator on the RHS is complex. By appropriate choice of collision operator in Boltzmann equation, Navier-Stokes equations can be recovered. One of the most frequently used simplifications for collision operator is linearisation which was first proposed by Bhatnagar, Gross and Krook (BGK) [14]. The BGK approximation assumes that the effect of the collision between particles is to drive the fluid in a linear fashion towards a local equilibrium state, f^{eq}. This approximation simplifies Boltzmann equation to

$$\boldsymbol{\xi} \cdot \nabla_{\mathbf{x}} + \mathbf{F} \cdot \nabla_{\mathbf{p}} f + \frac{\partial f}{\partial t} = -\frac{1}{\tau}(f - f^{eq}) \tag{2.7}$$

where τ in Eq. 2.7 is relaxation time and equilibrium distribution function (EDF), f^{eq} can be described by the Maxwell-Boltzmann distribution

$$f^{eq}(\mathbf{x}, \boldsymbol{\xi}, t) = \frac{\rho(\mathbf{x}, t)}{(2\pi k T(\mathbf{x}, t))^{Dm/2}} \exp\left[\frac{-(\mathbf{u}(\mathbf{x}, t) - \boldsymbol{\xi})^2}{2kT(\mathbf{x}, t)}\right] \tag{2.8}$$

where in Eq. 2.8, k is the Boltzmann constant, Dm is the dimension of the space, and ρ, $\mathbf{u}$ and T are the microscopic density of mass, velocity and temperature respectively. Macroscopic variables can be expressed as moments of the distribution function, f

$$\rho = \int f d\boldsymbol{\xi} = \int f^{eq} \boldsymbol{\xi} \tag{2.9a}$$

$$\rho \mathbf{u} = \int \boldsymbol{\xi} f d\boldsymbol{\xi} = \int \boldsymbol{\xi} f^{eq} \boldsymbol{\xi} \tag{2.9b}$$

$$\rho e = \frac{1}{2} \int (\boldsymbol{\xi} - \mathbf{u})^2 f d\boldsymbol{\xi} = \int (\boldsymbol{\xi} - \mathbf{u})^2 f^{eq} \boldsymbol{\xi} \tag{2.9c}$$

2.2.2.1 Discretization in time

Eq. 2.7 can be rewritten in the form of an ordinary differential equation

$$\frac{df}{dt} + \frac{1}{\lambda} f = \frac{1}{\lambda} f^{eq} \tag{2.10}$$

where $\frac{d}{dt} = \frac{\partial}{\partial t} + \xi \cdot \nabla$ is the time derivative in the characteristic line ξ. Eq. 2.10 can be integrated over the time step of Δt and simplifying the resulting equation using the Taylor series yields

$$f(\mathbf{x} + \boldsymbol{\xi}\Delta t, \boldsymbol{\xi}, t + \Delta t) - f(\mathbf{x}, \boldsymbol{\xi}, t) = -\frac{1}{\tau}[f(\mathbf{x}, \boldsymbol{\xi}, t) - f^{eq}(\mathbf{x}, \boldsymbol{\xi}, t)] \tag{2.11}$$

where τ in Eq. 2.11 is dimensionless relaxation time. Eq. 2.11 is obtained by neglecting the terms of order $O(\Delta t^2)$ and is therefore first order accurate.

The evaluation of moments in Eq. 2.9 needs appropriate discretization in momentum space. They can be calculated numerically using quadrature upto a certain degree of accuracy.

2.2.2.2 Discretization in space

The equilibrium distribution function can be obtained by using Taylor's series and truncating it to low velocities (i.e. Low Mach number approximation) is given in Eq. 2.12.

$$f^{eq}(\mathbf{x}, \boldsymbol{\xi}, t) = \frac{\rho(\mathbf{x}, t)}{(2\pi RT(\mathbf{x}, t))^{Dm/2}} \exp\left[-\boldsymbol{\xi}^2/2RT(\mathbf{x}, t)\right]\{1 + \frac{(\boldsymbol{\xi} \cdot \mathbf{u})}{RT} + \frac{(\boldsymbol{\xi} \cdot \mathbf{u})^2}{2(RT)^2} - \frac{(\mathbf{u})^2}{2RT}\} + O(\mathbf{u}^3) \tag{2.12}$$

The space discretization is governed by important considerations. The discretization should result in a lattice structure and quadrature used in evaluating the moments should be accurate enough to conserve mass, momentum and energy. Calculating the hydrodynamic moments of f^{eq} is equivalent to evaluating the following integral

$$I = \int \Psi(\boldsymbol{\xi}) f^{eq} d\boldsymbol{\xi} \tag{2.13}$$

where $\Psi(\xi)$ is a polynomial of ξ. The above integral can be evaluated by using Guassian-type quadrature. The choice of space discretization depends on choice of $\Psi(\xi)$. Some popular choices are as follows

Two dimensional 6-bit and 7-bit triangular lattice

$$\Psi_{m,n}(\boldsymbol{\xi}) = (\sqrt{2RT})^{m+n} \zeta^{m+n} cos^m\theta sin^n\theta \tag{2.14}$$

where in Eq.2.14, $\zeta = \xi/\sqrt{2RT}$

Two dimensional 5-bit and 9-bit Square lattice

$$\Psi_{m,n}(\boldsymbol{\xi}) = \xi_x^m \xi_y^n \tag{2.15}$$

where in Eq. 2.15, ξ_x and ξ_y are the components of ξ and m and n are the degree of polynomial in x and y directions respectively.

By employing appropriate weights, in a 9-bit square lattice the equilibrium distribution function can be simplified as follows:

$$f_\alpha^{eq} = w_\alpha \rho\{1 + \frac{3(\mathbf{e}_\alpha \cdot \mathbf{u})}{c^2} + \frac{9(\mathbf{e}_\alpha \cdot \mathbf{u})}{2c^4} - \frac{3\mathbf{u}^2}{2c^2}\} \tag{2.16}$$

where in Eq. 2.16, w is weight in each direction, e referred as ξ in Eq. 2.6 is velocity vector in each direction and c is the speed of sound i.e. $\sqrt{3RT}$ whereas subscript α denotes the different directions in the lattice.

The direction vectors and weights in a 9-bit square lattice are as follows

$$e_\alpha = \begin{cases} (0,0), & \alpha = 0 \\ (cos\theta_\alpha, sin\theta_\alpha)c, \theta_\alpha = (\alpha-1)\pi/2, & \alpha = 1,2,3,4 \\ \sqrt{2}(cos\theta_\alpha, sin\theta_\alpha)c, \theta_\alpha = (\alpha-5)\pi/2 + \pi/4, & \alpha = 5,6,7,8 \end{cases} \tag{2.17}$$

$$w_\alpha = \begin{cases} 4/9, & \alpha = 0 \\ 1/9, & \alpha = 1,2,3,4 \\ 1/36, & \alpha = 5,6,7,8 \end{cases} \tag{2.18}$$

The arrangement of 9-bit square lattice is shown schematically in Fig. 2.1.

The next step is to correlate the LBM with traditional CFD in which Navier-Stokes equations are solved. This correlation is done using Chapman-Enskog theory which is discussed in next section.

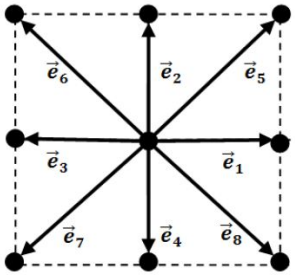

FIGURE 2.1: Two Dimensional 9-bit model

2.3 Chapman-Enskog Theory

As it is stated earlier, Lattice Boltzmann schemes describe in the mesoscopic scale while the Navier-Stokes equations in macroscopic scale. In order to connect these scales, Chapman-Enskog expansion can be used to recover Navier-Stokes equation from the Lattice Boltzmann equation in continuum limit. This can be done by the introduction of a new dimensionless number called Knudsen number. It is defined as the ratio of mesoscopic (L) length scale and macroscopic length scale (L_h).

$$\epsilon = \frac{L}{L_h} \tag{2.19}$$

An asymptotic analysis is carried out to show the coupling between Navier-Stokes and Lattice Boltzmann equations. Consider Eq.2.7 and expand LHS in Taylor series around (x, t). The distribution function is expanded in an asymptotic series near equilibrium as following

$$f = f^{eq} + \epsilon f^{(1)} + O(\epsilon^2) \tag{2.20}$$

The RHS of the Eq. 2.7 is also expanded similar to Eq. 2.20. The macroscopic and mesoscopic scaling for time and space is established using Knudsen number. Now both LHS and RHS of Eq. 2.7 expanded in terms of ϵ. Using asymptotic theory, it follows that all terms of same order in ϵ have to be equal. Now equating the corresponding coefficients and taking the moments will give the macroscopic conservation of mass and momentum Eq. 2.9. Now comparing them with Navier-Stokes equations gives

$$p = c_s^2 \rho \tag{2.21a}$$

$$\nu = \rho c_s^2 \Delta t (\tau - \frac{1}{2}) \tag{2.21b}$$

In the Eq. 2.21, c_s is speed of sound and is equal to $c/3$, ρ is density and p is pressure. Also, it gives the relation between kinematic viscosity of Navier-Stokes and relaxation time of lattice Boltzmann methods. It is obvious from the relation that the relaxation time should be more than 0.5 to avoid negative viscosity which is non-physical.

2.4 Implementation of LBM

This section focuses on how to implement the Lattice Boltzmann schemes to solve the flow problems. Going back to Lattice Boltzmann equation with BGK approximation, Eq. 2.7, the whole equation can be seen in two different stages. The LHS term in the equation is commonly referred as 'streaming' step while the RHS term is called 'collision step'. Thus, algorithmically, LBM can be implemented in two different stages. They can be represented as follows

$$CollisionStep : f(\mathbf{x}, t_+) = f(\mathbf{x}, t) - \frac{1}{\tau}[f(\mathbf{x}, t) - f^{eq}(\mathbf{x}, t)] \tag{2.22}$$

followed by streaming step

$$StreamingStep : f(\mathbf{x} + \mathbf{e}_\alpha \delta_t, t) = f(\mathbf{x}, t_+) \tag{2.23}$$

where t_+ is the imaginary intermediate time step. Schematically, it can be shown as in Fig. 2.2.

The macroscopic fluid density and velocities are computed by taking the moments of the particle distribution function. They are as follows

$$\rho(\mathbf{x}, t) = \sum_{i=0}^{8} f_i(\mathbf{x}, t) \tag{2.24}$$

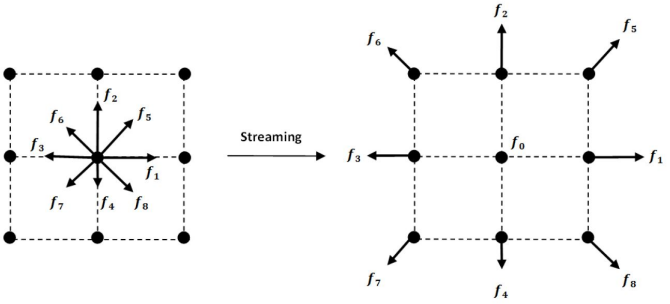

FIGURE 2.2: Streaming step in LBM

$$u(\mathbf{x},t) = \frac{1}{\rho}\sum_{i=0}^{8} \mathbf{e}_i f_i(\mathbf{x},t) \tag{2.25}$$

This process of collision and streaming is applied to all lattice points in the domain for every time step. The simplicity of the algorithm lies in the streaming step which is the non-linear advection term in Navier-Stokes equation. Also, pressure is computed using ideal gas equation in LBM while it is calculated using pressure-poisson equation in traditional finite volume techniques which involves iterative strategy. The whole algorithm is shown in Algorithm 1.

input : Lattice points, Initilization of ρ, u, f
output: ρ, u, p

for $i \leftarrow 1$ **to** nx **do**
  for $j \leftarrow 1$ **to** ny **do**
    Compute f^{eq} *from Eq. 2.16*
    Collision Step from Eq. 2.22
    Streaming step from Eq.2.23
    Compute macroscpic ρ*,u from* $\hat{f}$ *from Eq. 2.24, 2.25*
  end
end

Algorithm 1: Lattice Boltzmann Algorithm

During the streaming and collision step, the boundary nodes need special treatment on the distribution functions in order to satisfy the imposed macroscopic boundary conditions.

2.5 Boundary conditions

The two most widely used boundary conditions are no slip boundary conditions and velocity or pressure boundary conditions. No slip BC is referred as bounce-back BC in LBM literature.

2.5.1 Bounce-back BCs

The no-slip boundary condition occurs at the interface of the fluid and the stationary solid wall. The no-slip boundary condition can be implemented by the bounce back method which reflects the particle distribution functions at boundary nodes in the direction of incidence. However the bounce-back boundary condition is only first order accurate in most of the situations. It can be applied in two steps which gives second order accuracy. It is called second order bounce back BC.

2.5.1.1 First order Bounce back BC

The nodes lying within the wall region are called solid nodes and the nodes in the fluid region are fluid nodes. The single step bounce back method is applied at the fluid nodes just before the solid nodes. The post collision distribution functions ready to be streamed to the solid nodes are redirected in the opposite direction instead being streamed. The single step bounce back procedure is shown in Fig. 2.3

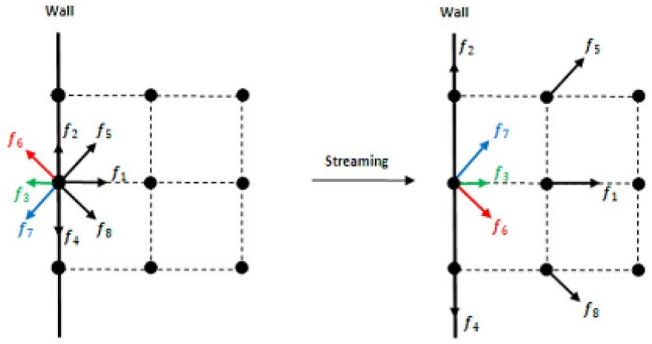

FIGURE 2.3: First order Bounce back BC

2.5.1.2 Second order Bounce back BC

The two step bounce back boundary condition is implemented in two time steps and at the solid nodes placed just adjacent to the boundary. As indicated in Fig. 2.4 the particle distribution function at fluid nodes are relaxed at time t resulting in three particle distributions pointing towards the respective solid nodes. They are propagated to the solid nodes during the streaming process. The bounce-back condition is then enforced on all the solid nodes by modifying the relaxation process by reversing the direction of each of the distributions at these nodes. Then the standard streaming process is performed so that the functions pointing in the direction of the fluid are streamed back to the fluid node. Thus at time $t + 2$ the reflected particle distribution functions are at the fluid nodes where they started ready to be relaxed. The advantage of the two step approach is that it is not required to define the fluid boundary nodes. As the physical boundary is assumed to lie halfway between the fluid node and the solid node the two step bounce back condition is found to be second order accurate.

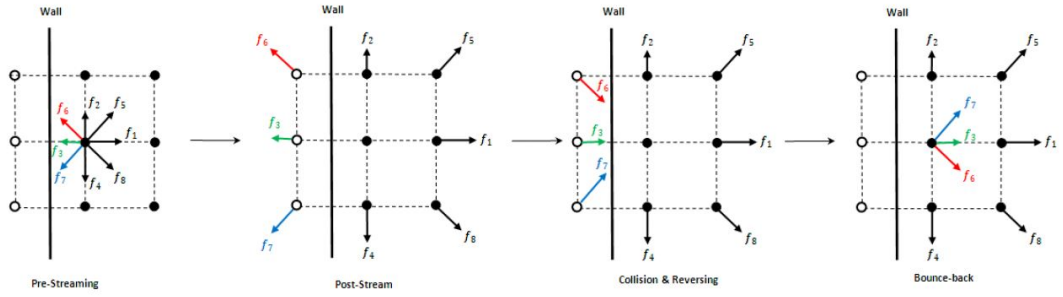

FIGURE 2.4: Second order Bounce back BC

2.5.2 Pressure and velocity BCs

The pressure and velocity BCs discussed here are proposed by Zou and He [15]. Same as in the case of bounce back BCs, particle distribution functions are calculated from the macroscopic variables on the boundary nodes. It is explained in the case of inflow for both velocity and pressure.

2.5.2.1 Velocity BCs

Consider the velocity u_x and u_y are prescribed on the inlet side of the domain as shown in Fig. 2.5. After streaming, the distributed functions which are coming inside the domain are unknown namely, f_1, f_5, f_8 along with ρ.

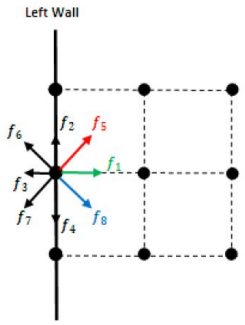

FIGURE 2.5: Velocity BC on the left side

Mass and momentum conservation equations can be written as follows

$$f_1 + f_5 + f_8 = \rho - (f_0 + f_2 + f_4 + f_3 + f_6 + f_7) \tag{2.26a}$$
$$f_1 + f_5 + f_8 = \rho u_x + (f_3 + f_6 + f_7) \tag{2.26b}$$
$$f_5 - f_8 = \rho u_y - f_2 + f_4 - f_6 + f_7 \tag{2.26c}$$

From Eqs. 2.26a and 2.26b, by eliminating f_1, f_5, f_8, density ρ can be calculated.

$$\rho = \frac{1}{1 - u_x}[f_0 + f_2 + f_4 + 2(f_3 + f_6 + f_7)] \tag{2.27}$$

There are 4 unknowns and only 3 equations. This system of equations is closed using the fourth equation that is obtained by the assumption that the bounce back rule holds for the non-equilibrium part of the particle distribution function normal to the boundary. The equation is

$$f_1 - f_1^{eq} = f_3 - f_3^{eq} \tag{2.28}$$

Using Eqs. 2.28 and 2.26 and also expressions for equilibrium parts of f_1^{eq} and f_3^{eq} rest of unknowns can be determined.

$$f_1 = f_3 + \frac{2}{3}\rho u_y \tag{2.29a}$$
$$f_5 = f_7 - \frac{1}{2}(f_2 - f_4) + \frac{1}{6}\rho u_x + \frac{1}{2}\rho u_y \tag{2.29b}$$
$$f_8 = f_6 - \frac{1}{2}(f_2 - f_4) + \frac{1}{6}\rho u_x - \frac{1}{2}\rho u_y \tag{2.29c}$$

2.5.2.2 Pressure BCs

As stated earlier, the pressure is related to density through ideal gas equation in LBM. Therefore, specifying pressure is equivalent to specifying density at the boundaries. Following the same steps as in the case of velocity BCs, the unknown particle distributions on left hand side along with velocity u_x can be obtained. They are

$$u_x = 1 - \frac{[f_0 + f_2 + f_4 + 2(f_3 + f_6 + f_7)]}{\rho_{in}} \tag{2.30a}$$

$$f_1 = f_3 + \frac{2}{3}\rho_{in}u_x \tag{2.30b}$$

$$f_5 = f_7 - \frac{1}{2}(f_2 - f_4) + \frac{1}{6}\rho_{in}u_x \tag{2.30c}$$

$$f_8 = f_6 + \frac{1}{2}(f_2 - f_4) + \frac{1}{6}\rho_{in}u_x \tag{2.30d}$$

The BCs discussed above suit well for structured and straight boundaries. But in reality, the geometries are very complicated and it is practically impossible to go to a scale that will result in lattice points on the boundary of domain. Therefore, there is a necessity to treat the curved boundaries separately in LBM. This is briefed in next section.

2.6 Curved boundary conditions

There are two main difficulties in dealing with curved boundaries. Firstly, lattice site is not necessarily located on boundary and it can be arbitrarily anywhere between fluid and solid lattice. Secondly, density or velocity cannot be obtained from conservation laws like in the case of straight boundaries as there are too many unknowns and not enough equations to solve.

There are two different approaches in treating curved boundary conditions. The first one is analagous to bounce back scheme, first proposed by Lallemand et al. [16] which is the modification of bounce back by Junk [17] and reflection back scheme with modification of velocity gradient to the non-equilibrium distribution by Chen [18]. The second approach is based on the fitting of the distribution function at the boundary nodes of the curved boundary. This was first proposed by Filippova [19].

2.6.1 Boundary fitting by Filippova-Hanel

Fig. 2.6 is adopted from Mei's [20] paper illustrates boundary fitting concept by Filippova [19]. The subscripts f denotes fluid lattice, w denotes wall and b stands for boundary node. The important parameter to be defined in this context is Δ. It is defined as

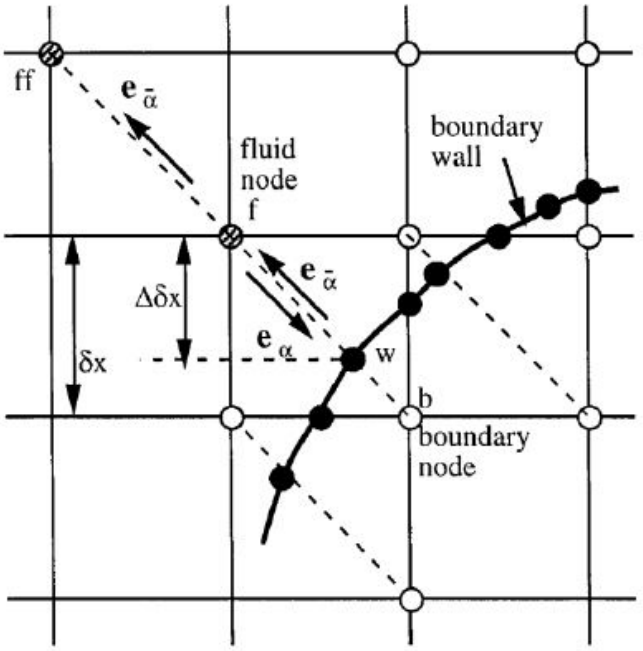

FIGURE 2.6: Curved boundary condition treatment

$$\Delta = \frac{|\mathbf{x}_f - \mathbf{x}_w|}{|\mathbf{x}_f - \mathbf{x}_b|} \tag{2.31}$$

After collision step, the distributed function in the direction from the solid to fluid at the boundary node is interpolated from the post collision distribution function in the opposite direction at the first fluid node and a fictitious distribution function similar to equilibrium distribution function.

$$\hat{f}_\alpha(t, \mathbf{x}_b) = (1-\chi)\hat{f}_\alpha(t, \mathbf{x}_f) + \chi\hat{f}^\star_\alpha(t, \mathbf{x}_b) + 2w_\alpha\rho(t, \mathbf{x}_f)\frac{\mathbf{u}(t, \hat{f}(t, \mathbf{x}_w)) \cdot \mathbf{e}_\alpha}{c_s^2} \tag{2.32}$$

When the wall velocity $u(t, \mathbf{x}_w)$ is zero, final term in Eq. 2.32 goes zero. The fictitious distribution function is given as

$$f_\alpha^\star(t,\mathbf{x}_f) = w_\alpha \rho(t,\mathbf{x}_f)(1 + \frac{\mathbf{e}_\alpha \cdot \mathbf{u}(t,\mathbf{x}_b)}{c_s^2} + \frac{(\mathbf{e}_\alpha \cdot \mathbf{u}(t,\mathbf{x}_f))^2}{2c_s^4} - \frac{\mathbf{u}^2(t,\mathbf{x}_f)}{2c_s^2}) \tag{2.33}$$

where $\mathbf{u}(t,\mathbf{x}_b)$ is given as follows

$$\mathbf{u}(t,\mathbf{x}_b) = \begin{cases} \mathbf{u}(t,\mathbf{x}_f), & \Delta < 1/2 \\ \frac{\Delta-1}{\Delta}\mathbf{u}(t,\mathbf{x}_f) + \frac{1}{\Delta}\mathbf{u}(t,\mathbf{x}_w), & \Delta \geq 1/2 \end{cases} \tag{2.34}$$

The weight χ is determined by set of assumptions and using Taylor expansion. The result obtained is as follows

$$\chi = \begin{cases} \frac{2\Delta-1}{\tau-1}, & \Delta < 1/2 \\ \frac{2\Delta-1}{\tau}, & \Delta \geq 1/2 \end{cases} \tag{2.35}$$

One of the obvious stability problem by above concept occurs when τ is close to 1. This is addressed by Mei [20] by using $\mathbf{u}(t,\mathbf{x}_{ff})$ instead of $\mathbf{u}(t,\mathbf{x}_f)$ when $\Delta < 1/2$.

2.7 Porous media modelling in LBM

The method used in the present study is adopted from Freed [21] which is an improvement on the model of Spaid and Phelan [22]. The idea is to include the external forces into the fluid by changing velocities during collision step.

If $\mathbf{F}$ is the external body force and $\mathbf{u}$ is the pre-collision velocity, then new pre-collision velocity including the force effect is

$$\mathbf{u}^n = \mathbf{u} + \frac{\mathbf{F}}{2\rho} \tag{2.36}$$

In the case of porous media, external force depends on the resistance of the membrane. If R_m is the resistance of porous media, the new velocity field can be expressed as

$$\mathbf{u}^n = (1 - \frac{1}{2\tau})\mathbf{u} + \frac{1}{2\tau}\grave{\mathbf{u}} \tag{2.37}$$

where $\grave{\mathbf{u}}$ is defined as $G \cdot \mathbf{u}$ where G is called velocity adjustment vector. It depends on resistance and τ. It is given by Eq. 2.38

$$G = \frac{1 - (\tau - 1/2)R_\alpha}{1 + 1/2R_\alpha} \tag{2.38}$$

where R_α is $R_m \nu$ and ν is kinematic viscosity.

Chapter 3

Finite Volume Methods for Convection Diffusion Problems

The distribution of suspended particles in the membrane filtration process is governed by two different phenomena namely convection and diffusion. Convection is the transport of particle due to bulk motion of the fluid whereas diffusion is the movement of the particle due to concentration difference. Both phenomena are collectively described by convection diffusion equation.

$$\frac{\partial \phi}{\partial t} + \nabla \cdot (\mathbf{u}\phi) = \nabla \cdot (D \nabla \phi) \tag{3.1}$$

In Eq. 3.1, ϕ is the conserved quantity and it could be concentration, volume fraction or mass fraction. $\mathbf{u}$ is the velocity vector and D is diffusion coefficient.

3.1 Basics of finite volume methods

In a finite volume scheme the domain is divided into small parts (the control volumes) and governing equations are integrated inside the control volumes. The most basic and simplest way is to divide a structured domain into finite number of rectangular sub domains. Nodal points are used within these control volumes for interpolating the field variable and usually, a single node at the centre of the control volume is used for each control volume. By application of the Gauss-divergence and integrating over each control volume will result the conservation equations into flux balance equation.

$$\frac{d}{dt}\int_{\delta V}\phi dV + \int_{\delta S}\mathbf{n}\cdot\mathbf{u}\phi dV = \int_{\delta S}\mathbf{n}\cdot D\nabla\phi dV \tag{3.2}$$

Eq. 3.2 can be interpreted as flux balance inside the control volume where V is the volume and A is the area of the face. The rate of change of the ϕ in δV is equal to the rate of transport of ϕ through δS by convective flux and diffusive flux. Eq. 3.2 is for any arbitrary shape for the control volume. If the rectangular control volume is chosen, the equation simplifies even further resulting in algebraic equation. This is explained in subsequent sections.

3.2 Finite volume discretization

Consider a rectangular domain divided into rectangular finite volumes as shown in Fig. 3.1. The conservative field variable is calculated at the center of each finite volume i.e. at P and hence it is cell centered.

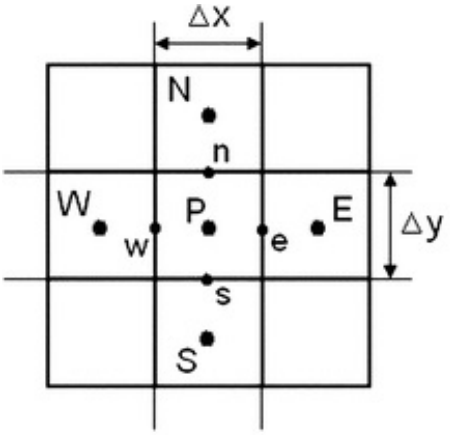

FIGURE 3.1: Finite volume discretization

Let Δx and Δy be the grid spacing in x and y direction respectively. W, E, N and S corresponds to west, east, north and south of the point P where the variable is being calculated. Similarly, w, e, n, s corresponds to the faces in different directions to point P. Now, taking the steady state convection-diffusion equation in 2-D and then integrating through the control volume gives

$$\int_{A}\mathbf{n}\cdot\phi\mathbf{u}dA = \int_{A}\mathbf{n}\cdot(D\nabla\phi)dA \tag{3.3}$$

Eq. 3.3 represents the flux balance in a control volume. The left hand side gives the net convective flux and the right hand side contains the net diffusive flux.

The principle problem in the discretization of the convective terms is the calculation of the value of transported variable at the control volume faces and its convective flux across these boundaries. There are several methods available for discretizing convective terms like central difference, hybrid scheme, flux limiting schemes etc. An important point to mention here is diffusion process affects the distribution of a transported quantity along its gradient in all directions, whereas convection spreads influence only in the flow direction. This crucial difference limits the grid size and the limit depends on relative strength of convection and diffusion.

Eq. 3.3 can be simplified into a algebraic equation by replacing the integral with flux terms.

$$(u_x A\phi)_e - (u_x A\phi)_w + (u_y A\phi)_n - (u_y A\phi)_s = (DA\frac{d\phi}{dx})_e - (DA\frac{d\phi}{dx})_w + (DA\frac{d\phi}{dy})_n - (DA\frac{d\phi}{dy})_s \tag{3.4}$$

where in Eq. 3.4 the terms in the parenthesis are flux in convection and diffusion and subscripts refer to the walls in different directions with respect to point P. It is convenient to two different variables F and Γ to represent convective and diffusive fluxes.

$$F = Au \tag{3.5a}$$

$$\Gamma = A\frac{D}{\Delta x} \tag{3.5b}$$

Throughout, these symbols are used with appropriate subscripts to indicate different directions. Eq. 3.4 can be further simplified into the following

$$F_e\phi_e - F_w\phi_w + F_n\phi_n - F_s\phi_s = \Gamma_e(\phi_E - \phi_P) - \Gamma_w(\phi_P - \phi_W) + \Gamma_n(\phi_N - \phi_P) - \Gamma_s(\phi_P - \phi_S) \tag{3.6}$$

As the field variable is calculated at cell centers, $\phi_E, \phi_W, \phi_N, \phi_S$ are well defined. As stated earlier, different strategies are possible in calculating $\phi_e, \phi_w, \phi_n, \phi_s$.

3.2.1 Central difference scheme

One of the simplest way to compute the face values for the convective terms is to linearly interpolate the cell center values on each side of the face. For a uniform grid considered,

$$\phi_e = \frac{\phi_P + \phi_E}{2} \tag{3.7a}$$
$$\phi_w = \frac{\phi_W + \phi_P}{2} \tag{3.7b}$$
$$\phi_n = \frac{\phi_P + \phi_N}{2} \tag{3.7c}$$
$$\phi_s = \frac{\phi_S + \phi_P}{2} \tag{3.7d}$$

Substituting Eq. 3.7 into Eq. 3.6 and rearranging results in the following equation.

$$\left[\left(\Gamma_w - \frac{F_w}{2}\right) + \left(\Gamma_e + \frac{F_e}{2}\right) + \left(\Gamma_s - \frac{F_s}{2}\right) + \left(\Gamma_n + \frac{F_n}{2}\right)\right]\phi_P = \left(\Gamma_w + \frac{F_w}{2}\right)\phi_W + \left(\Gamma_e - \frac{F_e}{2}\right)\phi_E + \left(\Gamma_s + \frac{F_s}{2}\right)\phi_S + \left(\Gamma_n - \frac{F_n}{2}\right)\phi_N \tag{3.8}$$

Eq. 3.8 can be further simplified into the following simple algebraic equation.

$$a_P\phi_P = a_W\phi_W + a_E\phi_E + a_S\phi_S + a_N\phi_N \tag{3.9}$$

where coefficients in Eq. 3.9 are defined as

$$a_W = \Gamma_w + \frac{F_w}{2} \tag{3.10a}$$
$$a_E = \Gamma_e - \frac{F_e}{2} \tag{3.10b}$$
$$a_S = \Gamma_s + \frac{F_s}{2} \tag{3.10c}$$
$$a_N = \Gamma_n + \frac{F_n}{2} \tag{3.10d}$$
$$a_P = a_W + a_E + a_S + a_N + (F_e - F_w) + (F_n - F_s) \tag{3.10e}$$

When the velocity field is known in the entire domain, Eq. 3.10 can be applied to each control volume which will result in the system of equations. The matrix equations upon assembling are sparse and can be solved using suitable numerical methods like LU decomposition methods.

3.2.1.1 Limitations of Central difference scheme

The fundamental properties any discretization scheme should posses are conservativeness, boundedness and transportiveness. In order to ensure the field variable is conserved in the entire domain, the flux leaving the face of one control volume should be same as the flux entering the adjacent control volume. This can be achieved only through consistent flux interpolation formulae. The central difference scheme satisfies the conservativeness while the quadratic interpolation would not result in conservative interpolation.

The field variable being solved should be bound within the boundary values of the domain. This can be ensured by having the diagonal dominance in the matrix system of equations. If the condition of diagonal dominance is not satisfied, the calculated solution will have overshoots and undershoots around the physical result. In the case of central difference scheme, boundedness is satisfied when Peclet number, $Pe = F/\Gamma$ is less than 2. When $Pe > 2$, east coefficient become negative and violates boundedness requirement.

When the flow is from left to right, the point P is solely influenced by its west neighbour. Similarly, when flow is from right to left, P is influenced by east neighbour. Ability of the interpolation scheme to identify the flow direction is an important requirement to get physically realistic results. In central difference scheme, the point P has its influence from both east and west neighbouring points. Hence it cannot recognise the direction of flow and may fail at high Pe number.

Some of the above limitations of central difference scheme are addressed in Upwind scheme which is discussed.

3.2.2 Upwind differencing scheme

One of the main drawback of the central differencing scheme is its inability to identify the direction of flow. In a strongly convective flow from left to right, the point P should get more influence from W then E. In upwind scheme, the direction of flow is taken into account when computing the value at the cell face.

This is done by making the value of field variable ϕ at a cell face to be equal to the value at the upstream cell center. Mathematically, it is done in 1-D as follows

When the flow is in positive direction in both x and y directions, $F_w > 0, F_e > 0, F_n > 0, F_s > 0$, upwind scheme sets to

$$\phi_w = \phi_W \tag{3.11a}$$
$$\phi_e = \phi_P \tag{3.11b}$$
$$\phi_s = \phi_S \tag{3.11c}$$
$$\phi_n = \phi_P \tag{3.11d}$$

and the discretized equation becomes

$$F_e\phi_P - F_w\phi_W + F_n\phi_P - F_s\phi_S = \Gamma_e(\phi_E - \phi_P) - \Gamma_w(\phi_P - \phi_W) + \Gamma_n(\phi_N - \phi_P) - \Gamma_s(\phi_P - \phi_S) \tag{3.12}$$

and upon rearranging to write in standard form gives

$$a_P\phi_P = a_W\phi_W + a_E\phi_E + a_S\phi_S + a_N\phi_N \tag{3.13a}$$
$$a_W = \Gamma_w + max(F_w, 0) \tag{3.13b}$$
$$a_E = \Gamma_e + max(0, -F_e) \tag{3.13c}$$
$$a_S = \Gamma_s + max(F_s, 0) \tag{3.13d}$$
$$a_N = \Gamma_n + max(0, -F_n) \tag{3.13e}$$
$$a_P = a_W + a_E + a_N + a_S + (F_e - F_w) + (F_n - F_s) \tag{3.13f}$$

Upwind scheme uses consistent formulae to compute fluxes through faces and hence is conservative. As long as the flow field is conservative, the scheme results in diagonally dominant matrix. This property satisfies the requirement of boundedness. As the scheme accounts the direction of flow, it ensures the transportiveness property is satisfied. The main drawback of the scheme is only being a first-order accurate on the basis of Taylor's series truncation error. Another drawback can be observed when the flow is not aligned with the axis. The field variable will get smeared in that situation which is commonly termed as 'artificial

diffusion'. At higher Reynolds number, this artificial diffusion is high enough to give physically unrealistic results.

3.2.3 Hybrid differencing scheme

Hybrid differencing scheme is the combination of central and upwind differencing schemes. When the Peclet number is small, $Pe < 2$, central differencing scheme is used and when $Pe > 2$, upwind scheme is used. Mathematically, it can expressed as

$$a_P\phi_P = a_W\phi_W + a_E\phi_E + a_S\phi_S + a_N\phi_N \tag{3.14a}$$

$$a_W = max\left[F_w, \left(\Gamma_w + \frac{F_w}{2}\right), 0\right] \tag{3.14b}$$

$$a_E = max\left[-F_e, \left(\Gamma_e - \frac{F_e}{2}\right), 0\right] \tag{3.14c}$$

$$a_S = max\left[F_s, \left(\Gamma_s + \frac{F_s}{2}\right), 0\right] \tag{3.14d}$$

$$a_N = max\left[-F_n, \left(\Gamma_n - \frac{F_n}{2}\right), 0\right] \tag{3.14e}$$

$$a_P = a_W + a_E + a_N + a_S + (F_e - F_w) + (F_n - F_s) \tag{3.14f}$$

Hybrid differencing scheme posses the favourable properties of the upwind and central differencing schemes. The scheme is fully conservative, unconditionally bounded and also has the transportiveness property. Hybrid scheme is chosen over central difference scheme in the present work. Even though there are several higher order methods like QUICK, flux limiting schemes (TVD) etc., hybrid scheme is chosen because of its relative simplicity and implementation and computational costs.

3.3 Boundary conditions

The two widely used boundary conditions in the case of solving convection diffusion equation is fixed value of field variable i.e. Dirichlet boundary condition and free outflow which is Neumann boundary condition. These BCs are incorporated into the systems of equations as an external source term which goes on right hand side of the system.

3.3.1 Dirichlet BC

Consider the left side of the domain have a prescribed value of ϕ_A. Therefore, there is no need to interpolate the face value of west side of the control volumes sharing the left boundary as shown in Fig. 3.2. In this example, central difference scheme is used to demonstrate the implementation of BC.

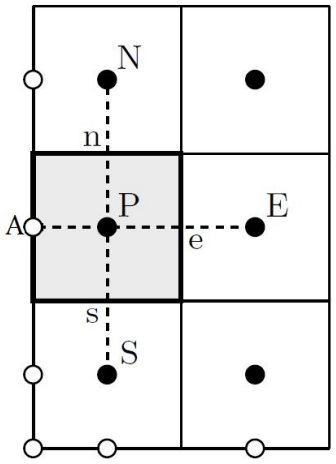

FIGURE 3.2: Boundary condition implementation in FV

Now going back to discretized Eq. 3.6 and applying the BC yields

$$\frac{F_e}{2}(\phi_P + \phi_E) - F_A\phi_A + \frac{F_n}{2}(\phi_P + \phi_N) - \frac{F_s}{2}(\phi_P + \phi_S) = \Gamma_e(\phi_E - \phi_P) - 2\Gamma_w(\phi_P - \phi_A) + \Gamma_n(\phi_N - \phi_P) - \Gamma_s(\phi_P - \phi_S) \quad (3.15)$$

From Eq. 3.15 it is clear that the west face convective flux term is $F_A\phi_A$. The diffusive flux on the west face has a factor of 2. This can be explained from Fig. 3.2 that the distance from node P to other nodes N, E, S is Δx and Δy respectively, while distance from P to west face, w is only $\Delta x/2$. Now rearranging this equation into standard form gives

$$a_P\phi_P = a_W\phi_W + a_E\phi_E + a_S\phi_S + a_N\phi_N + S_u \quad (3.16a)$$

$$a_P = a_W + a_E + a_N + a_S + (F_e - F_w) + (F_n - F_s) - S_P \quad (3.16b)$$

$$S_u = (2\Gamma + F)\phi_A \quad (3.16c)$$

$$S_P = -(2\Gamma - F) \quad (3.16d)$$

in Eq. 3.16 rest of the coefficients have their usual meaning. The same procedure can be applied to any boundary and deduce the discretized equation in form of Eq. 3.16.

3.3.2 Neumann BC

When the condition at the outlet is not known before, Neumann BC can be applied. Mathematically, it can be written $\frac{\partial \phi}{\partial x} = 0$. Using Taylor's series, derivative of ϕ can be approximated as

$$\frac{\partial \phi}{\partial x} = \frac{\phi_n - \phi_{n-1}}{h} \tag{3.17}$$

Consider the right part of the domain is applied with free flow boundary condition. Then according to the approximation in Eq. 3.17, $\phi_B = \phi_P$ where ϕ_B is the boundary value of field variable and ϕ_P is the value of the node of control volume sharing its east face with the domain boundary. Using the same approach as in the case of Dirichelet BC, the flux balance equation becomes,

$$\begin{aligned} F_B\phi_B - \frac{F_w}{2}(\phi_P + \phi_W) + \frac{F_n}{2}(\phi_P + \phi_N) - \frac{F_s}{2}(\phi_P + \phi_S) = \\ 2\Gamma_e(\phi_B - \phi_P) - \Gamma_w(\phi_P - \phi_A) + \Gamma_n(\phi_N - \phi_P) - \Gamma_s(\phi_P - \phi_S) \end{aligned} \tag{3.18}$$

Now replacing ϕ_B with ϕ_P and rearranging the equation gives the following

$$a_P\phi_P = a_W\phi_W + a_E\phi_E + a_S\phi_S + a_N\phi_N + S_u \tag{3.19a}$$
$$a_P = a_W + a_E + a_N + a_S + (F_e - F_w) + (F_n - F_s) - S_P \tag{3.19b}$$
$$a_E = 0 \tag{3.19c}$$
$$S_u = 0 \tag{3.19d}$$
$$S_P = 0 \tag{3.19e}$$

3.3.3 Robin BC

Combination of Dirichlet and Neumann BCs constitute Robin BC. In the case of convection diffusion equation it can be expressed as

$$\alpha u_x \phi + \frac{\partial \phi}{\partial x} = \beta \tag{3.20}$$

where in Eq. 3.20, α and β are scalar constants. If $\alpha = 1$ and $\beta = 0$, then the boundary condition represents wall boundary condition. Physically, it can explained as the convective flux coming to the wall is equal to the diffusive flux and there by no particle accumulation on the wall. This particular BC is used as membrane BC in the present work and its implementation is given below for any arbitrary α and $\beta = 0$.

Lets consider ϕ_m is the field variable value at the boundary and ϕ_P is the node center value of control volume sharing its face with the boundary. Now, rewriting Eq. 3.20 in semi discretized form yields

$$\phi_m = \frac{2\Gamma \phi_P}{2\Gamma - \alpha F} \tag{3.21}$$

Now, Eq. 3.21 can be used in the discretized equation of control volume and replacing the wall field value with the above expression.

3.4 Time discretization

Integration of transient convection diffusion equation in a control volume over a time interval from t to $t + \Delta t$ gives

$$\int_t^{t+\Delta t} \int_{CV} \frac{\partial \phi}{\partial t} dV dt + \int_t^{t+\Delta t} \int_{CV} \nabla \cdot (\mathbf{u}\phi) dV dt = \int_t^{t+\Delta t} \int_{CV} \nabla \cdot (D \nabla \phi) dV dt \tag{3.22}$$

The unsteady term in LHS in Eq. 3.22 can be discretized as follows

$$\int_{CV} \left(\int_t^{t+\Delta t} \frac{\partial \phi}{\partial t} dt \right) dV = (\phi - \phi^0) \Delta V \tag{3.23}$$

where in Eq. 3.23, ϕ and ϕ^0 are the field variables at time t and $t + \Delta t$ respectively. This is first-order backward differencing scheme obtained from Taylor's expansion. Higher order differencing schemes can be used to discretize the unsteady term. The more general time discretization expressed is given as follows

$$I_T = \int_t^{t+\Delta t} \frac{\partial \phi}{\partial t} dt = \left[\theta\phi^0 + (1-\theta)\phi\right] \Delta t \tag{3.24}$$

where θ is weighting parameter. Different values of integrals I_T for different values of θ are tabulated below

TABLE 3.1: Time discretization for convection diffusion equation using finite volume

θ	0	1/2	1
I_T	$\phi_0 \Delta t$	$\frac{1}{2}(\phi + \phi_0)\Delta t$	$\phi \Delta t$

In Table 3.1, when θ is 0 it is explicit time integration scheme where only field variable at old time step is needed to know to compute the new value at present time step. When $\theta = 1$ the method is implicit and when $\theta = 1/2$, the method is called Crank-Nicolson scheme. Both implicit and Crank-Nicolson schemes needs information at the present time step to compute the field variable. Hence they result in a system of equations which has to be solved using numerical techniques. This is discussed in next section. Explicit time stepping is relatively simple to implement and computationally less expensive when compared to implicit and Crank-Nicolson schemes. But explicit scheme is conditionally stable where as implicit and Crank-Nicolson schemes are unconditionally stable. In the present work, implicit time stepping is used.

3.5 System of equations

The final stage in solving any physical problem using numerical techniques is solving the system of equations resulting from application of any discretization technique. As outlined in previous sections, application of finite volume techniques results in a algebraic equation for each control volume in the following form

$$a_P \phi_P + \sum_c a_C \phi_C = S_u \tag{3.25}$$

where in Eq. 3.25, c represents the directions of neighbouring control volumes. Globally, i.e., for all control volumes $CV_i (i = 1, ..., N)$ of the problem domain, this gives a linear system of N equations.

$$a_P^{i,j}\phi_P^{i,j} + \sum_c a_C^{i,j}\phi_C^{i,j} = S_u^{i,j} \tag{3.26}$$

for the N unknown nodal values of $\phi^{i,j}$ in the CV centers. Consider there are N CVs in the direction of x and M in the direction of y as shown in Fig. 3.3.

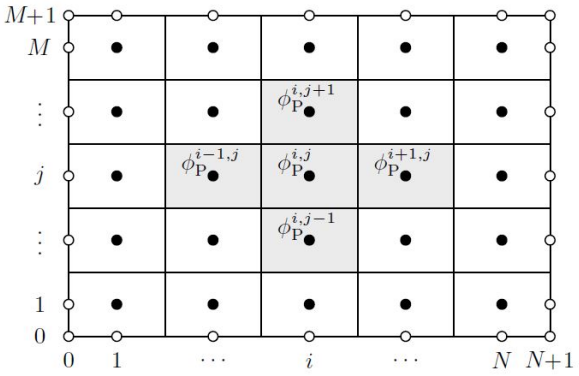

FIGURE 3.3: Arrangement of CVs and nodes in 2-D

By numbering the CVs columnwise, the arrangement of unknown field variables $\phi^{i,j}$ results in the system matrix $\mathbf{A}$ as follows

$$\begin{bmatrix}
a_P^{1,1} & -a_N^{1,1} & \cdots & 0 & \cdots & -a_E^{1,1} & \cdots & \cdots & 0 \\
-a_S^{1,2} & \ddots & \ddots & & & & \ddots & \cdots & \vdots \\
\vdots & \ddots & \ddots & \ddots & & & & \ddots & \\
0 & & \ddots & \ddots & \ddots & & & & -a_E^{N-1,M} \\
-a_W^{1,2} & & & \ddots & \ddots & \ddots & & & \vdots \\
 & \ddots & & & \ddots & \ddots & \ddots & & 0 \\
\vdots & & \ddots & & & \ddots & \ddots & \ddots & \vdots \\
\vdots & & & \ddots & & & \ddots & \ddots & -a_N^{N,M-1} \\
0 & \cdots & & \cdots & -a_W^{N,M} & 0 & \cdots & -a_S^{N,M} & -a_P^{N,M}
\end{bmatrix} \tag{3.27}$$

Linear solution methods can broadly be classified into two categories, direct or iterative. Direct methods, such as Gauss elimination, LU decomposition etc. If there are N CVs, then direct methods need N^2 entries to be stored while only $5N$ of them are non-zero. They also do not take advantage of any initial guess of the solution. Iterative methods on the other hand, can easily be formulated to take advantage of the matrix sparsity. Since these methods successively improve the solution by the application of a fixed number of operations, we can stop the process when the solution at any given outer iteration has been obtained to a

sufficient level of accuracy. As the outer iterations progress and we have better initial guesses for the iterations of the linear solver, the effort required during the linear solution also decreases.

The above formulation results in a sparse unsymmetric matrix. HSL [23] library subroutines are used to solve the resulting matrix **A**. MA41 is used in the present work. The method in the subroutine is based on Gaussian elimination. It uses multifrontal approach and is discussed in detail by Duff [24].

Chapter 4

Methodology

This chapter focuses on the implementation of LBM and FV techniques to simulate the cross-flow membrane filtration process. The present work deals with 3 different models. They are

- Model based on cake formation phenomenon in cross-flow micro- and nano-filtration process
- Concentration polarisation model for inorganic and interacting solute particles in nano-filtration
- Rejection prediction model in cross-flow nano-filtration process

Different strategies were employed to implement the above models. Thereafter, water in the filtration process is referred to as solvent and the particles to be filtered are referred to as solute particles. In the case of cake formation, solute particles are suspended substances in the water where as in the case of rejection models solute particles are dissolved salts. Solvent is simulated by solving Navier-Stokes equation and solute movements in the solvent are simulated by solving convection-diffusion equation.

4.1 LBM solute-solvent model

In this model both NS equations and convection-diffusion are solved using LB schemes. Both set of equations are solved coupled in each time step. The coupling

is done through viscosity in NS equations and velocity vector used in convection diffusion equation. The implementation details of LBM for NS equations is discussed in Chapter 2. The implementation details for convection diffusion equation similar to the case of NS.

4.1.1 LBM for convection diffusion equation

Just like in the case of NS equations, the particle distribution function represents field variable in the case of convection diffusion equation. If f is the particle distribution function, then

$$\phi = \sum_i f_i \tag{4.1}$$

Similarly second moment of distribution function gives convective flux, $\mathbf{u}\phi$. The relaxation time in the case of convection diffusion depends on diffusion coefficient, D.

$$D = c_s^2 \left(\tau - \frac{1}{2}\right) \Delta t \tag{4.2}$$

where in Eq. 4.2, c_s is the speed of sound and Δt is the time step. The lattice models used for NS implementation can be used for convection diffusion too. Most common are D2Q5, D2Q9, D3Q27. In the present work, D2Q5 model is used. The equilibrium distribution function in the case of convection diffusion equation is as follows

$$f_\alpha^{eq}(\mathbf{x}, t) = w_\alpha \phi \left(1 + 3\mathbf{u} \cdot \mathbf{e}_\alpha\right) \tag{4.3}$$

where in Eq. 4.3, $\mathbf{u}$ is the velocity, $\mathbf{e}_\alpha$ is the direction vector of the lattice. Solving the equation is as same as in the case of NS equations where streaming step is followed by collision step with the distribution function given in Eq. 4.3.

Boundary conditions are applied in the same way as NS scheme of LBM. Common BCs in convection diffusion equation is constant field variable, flux boundary condition. In the case of constant ϕ BC at the left boundary, only one particle distribution function going out of domain is unknown and rest of the them are known post streaming. If f_0, f_2, f_3, f_4 are known post streaming and ϕ_{in} is the boundary field variable, then using Eq. 4.1

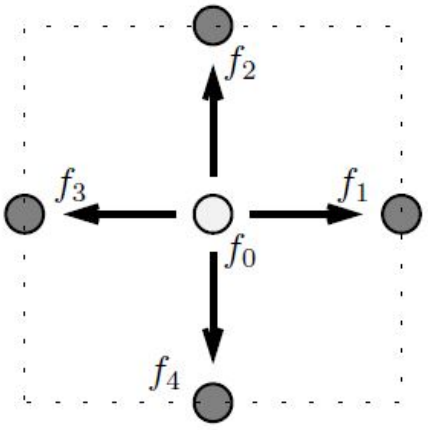

FIGURE 4.1: D2Q5 lattice structure

$$f_1 = \phi_{in} - (f_0 + f_2 + f_3 + f_4) \tag{4.4}$$

Similarly, flux boundary condition can be applied. Taking the first moment of particle distribution function gives

$$u_x\phi = f_1 - f_3 \tag{4.5a}$$
$$u_y\phi = f_2 - f_4 \tag{4.5b}$$

If the flux is specified at the boundary, using Eq. 4.5 there is only one unknown particle distribution function. It can be computed by using flux value and known particle distribution function.

4.1.2 Implementation of model

As stated in earlier sections, the coupling from NS to convection diffusion is done by using velocity vector obtained by NS at each lattice point. The coupling from convection diffusion to NS is achieved by viscosity which depends on the field variable, ϕ at each lattice point.

$$\nu(\phi) = \nu_0 \left[1 + 1.5\frac{\phi}{\left(1 - \frac{\phi}{0.6}\right)}\right]^2 \tag{4.6}$$

where in Eq. 4.6, ν_0 is the kinematic viscosity of pure solvent, ϕ is volume fraction of solute. This is first proposed by Romero and Davis [25].

Typically, in one time step, first NS equations are solved using LBM at all lattice points. Then the computed velocity is used in solving convection diffusion equation to compute the volume fraction. The new volume fraction is used to update the viscosity using Eq. 4.6 for the next time step. Diffusion coefficient depends on the filtration process and is discussed in detail in further chapters.

input : Lattice points, Initilization of ρ, $\mathbf{u}$, f, g, D, ν
output: ρ, u, p, ϕ

for $\Delta t \leftarrow ntimesteps$ **do**
  for $i \leftarrow 1$ **to** nx **do**
    for $j \leftarrow 1$ **to** ny **do**
      Solve NS equations for solvent
      ↓
      Compute macroscopic variables
      ↓
      Solve CD equation using velocity field obtained from NS
      ↓
      Compute volume fraction ϕ
      ↓
      Update viscosity for next time step using Eq. 4.6 compute the additional resistance offered by cake using Eq. 4.7
    end
  end
end

Algorithm 2: Coupling of solvent and solute using LBM

4.1.3 Cake predicting model

The above model needs special treatment for cake predicting model. As discussed in Chapter 1, cake layer formation is inevitable when the suspended particles cannot diffuse back to bulk solution fast enough. In this present model when the volume fraction at the membrane surface reaches 0.6, it is assumed that cake layer is formed. This assumption is in agreement with the maximum random packing fraction which is around 0.64 for hard spheres. As the suspended particles are not perfectly spherical a value of 0.6 is used in present computations.

When the volume fraction at a lattice node exceeds 0.6, the node is treated as wall while solving for solute and it is treated as porous media while solving for solvent. Mathematically, first order bounce back is applied for convection diffusion solver

and hydraulic resistance is added to NS solver. The value of resistance is obtained through Carman-Kozeny relation.

$$R_c = \frac{C(1-\epsilon_c)^2 S_c^2}{\epsilon_c^3} \tag{4.7}$$

In Eq. 4.7, constant $C = 5$, S_c is specific surface, $S_c = 3/a$ where a is the radius of the suspended particle and ϵ_c is the porosity of randomly packed cake layer and is assumed to be 0.4.

Another important parameter in implementing the model is diffusion coefficient. Choosing the appropriate diffusion coefficient is the key to the effective implementation of the model. As stated in Chapter 1, type of diffusion depends on the size of the suspended particles. Shear induced diffusion and Brownian motion are two important types considered in this work. Cho [26] determined the cross over size of the particle where Brownian motion dominates over shear induced diffusion. When the particle size is less than $0.1\mu m$, Brownian motion dominates while shear induced diffusion dominates when size is more than $0.1\mu m$. Therefore, in this present work shear induced diffusion is used in micro-filtration modelling as the size of particles is around $5\mu m$ and Brownian diffusion is used in the case of nano-filtration when size of particles is in the scale of nm. Shear induced diffusion coefficient can be obtained by the knowledge of particle size and shear rate in the filtration device.

$$D = 0.33\dot{\gamma}a^2\phi^2(1 + 0.5e^{8.8\phi}) \tag{4.8}$$

In Eq. 4.8, a is the radius of the particle, ϕ is the volume fraction of the solute and $\dot{\gamma}$ is the shear rate. The shear rate is computed at each time step from the velocity field inside the domain and is used in computing diffusion coefficient.

Brownian diffusion comes from the Brownian motion of the particles and this can be quantified by Stokes-Einstein equation.

$$D = \frac{kT}{6\pi\eta a} \tag{4.9}$$

where in Eq. 4.9, k is the Boltzmann constant, T is the absolute temperature, η is the solvent viscosity and a is the particle radius. This relation quantifies the diffusion of a single particle. But in this work volume fraction is being used and

therefore the variation of diffusion with volume fraction, ϕ needs to be established. This is discussed in the next section.

4.1.4 Concentration polarisation of interacting solute particles model

Solute-solute interactions are prominent in nano-filtration (NF) and relatively negligible in micro-filtration (MF). The interactions at nanoscale are more prominent than microscale. In the present model non-ionic particles are considered.

The two important phenomenon in this model are osmotic pressure and diffusion coefficient. Osmotic pressure ($\Delta\Pi$) acts in the opposite direction of applied pressure (ΔP) due to the difference in particle concentration on either side of the membrane. When the polarized layer exists, the permeate flux v_w can be expressed as

$$v_w = \frac{\Delta P - \sigma_0 \Delta\Pi}{\eta R_m} \tag{4.10}$$

In Eq. 4.10, σ_0 is the reflection coefficient and is assumed to be 1, η ($\rho\nu$) is the dynamic viscosity of solvent and R_m is the resistance of the membrane. Osmotic pressure can be obtained from Vant-Hoff equation for ionic solute particles, but for non-ionic particles it is complex non-linear function of membrane solute concentration. It can be calculated by virial equation of state [27].

$$\Pi = nkT - \frac{2}{3}\pi n^2 \int_0^\infty r^3 g(r) \frac{dE}{dr} dr \tag{4.11}$$

where in Eq. 4.11, k is Boltzmann constant, T is the temperature, r is the radial position, $g(r)$ is the radial distribution function and $E(r)$ is the pair interaction energy of the solute particles and n is the number density of particles ($3\phi/4\pi r_p^3$). $g(r)$ and $E(r)$ has to be determined to compute osmotic pressure of the solute from Eq. 4.11. Radial distribution function can be obtained using Ornstein-Zernike (OZ) integral equation.

Ornstein-Zernike (OZ) integral equation is solved with hypernetted chain (HNC) closure for solute particles to obtain radial distribution function. The radial distribution function is probability of finding particles as a function of distance measure from the particle itself. Therefore, radial distribution function tends to zero at very

low distances as two particles cannot occupy same space and at larger distances it tends to one as it represents bulk solution. OZ integral solves for total correlation function which is related to radial distribution function. Total correlation function is the influence of one particle on another particle in the solution. This influence can be divided into direct influence characterised by direct correlation function and indirect influence characterised by indirect correlation function. Integrating this correlation function for whole solution gives the positions of particles relative to each other which is radial distribution function.This integral equation has two unknowns and need another closure to solve. Commonly used closures are Percus-Yevick approximation (PY), well adapted for particles with an impenetrable core, and the hypernetted-chain equation (HNC), widely used for softer potentials. The interaction potential used in the closures gives the equilibrium solution structure. This integral is convolution in nature and is solved using Fourier sine transforms.

4.1.4.1 Solution to OZ integral equation

The present work uses integral equation method to solve for the radial distribution function using OZ equation.

$$h(r) = c(r) + n \int h(r')c(r - r')dr' \tag{4.12}$$

where in Eq. 4.12, $h(r) = g(r) - 1$ is the total correlation function and $c(r)$ is the direct correlation function. Eq. 4.12 has two unknowns and therefore it needs one more equation to close it. HNC closure is chosen in present work.

$$c(r) = \exp[-\beta E(r) + \gamma(r)] - \gamma(r) - 1 \tag{4.13}$$

where in Eq. 4.13, $E(r)$ is the pair potential between solute particles. The two important forces acting between the particles are van der Waals forces and electrostatic double layer forces. Therefore, $E(r)$ can be expressed as sum of the above two potentials

$$E(r) = -\frac{A}{12}\left[\frac{1}{R^2} + \frac{1}{R^2 - 1} + 2ln\left(1 - \frac{1}{R^2}\right)\right] + \frac{z_p^2 e^2}{4\pi\epsilon_0\epsilon_r}\frac{\exp(-\kappa(r - \sigma))}{r(1 + \kappa\sigma/2)^2} \tag{4.14}$$

where in Eq. 4.14, R is the dimensionless center to center distance (r/σ) and σ is diameter of the particle, A is Hamaker constant, z_p is the charge number on the solute particle, e is the electronic charge, ϵ_r is the dielectric constant of the solvent, ϵ_0 is the dielectric constant of vacuum and κ is the inverse Debye screening length. Debye screening length can be determined from following relation.

$$\kappa^{-1} = \left(\frac{\epsilon_0 \epsilon_r kT}{2000 N_A e^2 z^2 C_{EL}} \right)^{1/2} \tag{4.15}$$

where in Eq. 4.15, N_A is the Avagadro number and C_{EL} is the molar concentration of the electrolyte. The numerical solution to OZ integral equation is discussed in Appendix.B.

4.1.4.2 Gradient diffusion coefficient

Osmotic pressure can be obtained for any solute concentration once OZ integral is solved numerically for radial distribution function. As stated earlier that in the case of NF, Brownian diffusion is the dominant phenomenon and there is a necessity to build a concentration dependence of the diffusion coefficient. This can be computed by the theory of batch sedimentation process. The concentration dependence can be expressed as follows

$$D(\phi) = D_\infty K(\phi) \frac{d[\phi Z(\phi)]}{d\phi} \tag{4.16}$$

where in Eq. 4.16, D_∞ is the diffusion coefficient of single solute particle and can be obtained from Eq. 4.9, $K(\phi)$ is the sedimentation coefficient and $Z(\phi)$ is the osmotic compressibility (Π/nkT).

Sedimentation coefficient can be expressed as a function of the solute volume fraction.

$$K(\phi) = (1 - \phi)^\alpha \tag{4.17}$$

and coefficient α in Eq. 4.17 is expressed as follows

$$\alpha = 5 + 3 \int_2^\infty [1 - g_{ss}] s ds - \int_2^\infty [A_{11} + A_{12} + 2(B_{11} + B_{12}) - 3(1 + 1/s) g_{ss} s^2 ds] \tag{4.18}$$

The coefficients in Eq. 4.18 are as follows

$$g_{ss}(r) = exp\left(-\frac{E(r)}{kT}\right) \tag{4.19a}$$

$$A_{11} = 1 - \frac{60}{16s^4} \tag{4.19b}$$

$$A_{12} = \frac{3}{2s} - \frac{1}{s^3} \tag{4.19c}$$

$$B_{11} = 1 \tag{4.19d}$$

$$B_{12} = \frac{3}{4s} + \frac{1}{2s^3} \tag{4.19e}$$

$$s = \frac{r}{r_p} \tag{4.19f}$$

Substituting Eq. 4.19 in Eq. 4.18 and integrating gives α. Note that the function g_{ss} depends of the radial distribution function, so sedimentation coefficient depends on $g(r)$. Once $K(\phi)$ and $Z(\phi)$ are computed, $D(\phi)$ can be calculated numerically and can be fitted to curve to obtain a polynomial function.

4.1.4.3 Implementation of model

The implementation of model is pretty much the same as given in Algorithm 2. The only difference being updating the applied pressure after each time step depending on the concentration on the membrane surface. Hence, the model is solved as a transient problem and solved till it reaches a pseudo steady state where the change in the concentration in the domain is very small. The implementation is given in Algorithm 3.

The residual used in this work is $L2$ norm and a tolerance of 10^{-5} is specified. Both $\Pi(\phi)$ and $D(\phi)$ are fitted into polynomial curves using MATLAB^{TM}.

This model is only valid for non-ionic solute particles and cannot be used for ionic solutes. Osmotic pressure depends directly on the radius of solute particle and becomes negligible when the particle radius is few hundereds nanometer. In that case, osmotic pressure can be safely ignored without losing significant accuracy.

input : Lattice points, Initilization of ρ, $\mathbf{u}$, f, g, $D(\phi)$, ν, $\Pi(\phi)$
output: ρ, u, p, ϕ

while $iter \leftarrow maxiterandres > tolerance$ **do**
  for $i \leftarrow 1$ **to** nx **do**
    for $j \leftarrow 1$ **to** ny **do**
      Solve NS equations for solvent
      ↓
      Compute macroscopic variables
      ↓
      Solve CD equation using velocity field obtained from NS
      ↓
      Compute volume fraction ϕ
      ↓
      Update viscosity using Eq.4.6 and flux using Eq.4.10 for next time step
      ↓
      Calculate Residual, $res = \sum_{i,j}(\phi_n - \phi_{n+1})^2$
    end
  end
end

Algorithm 3: Coupling of solvent and solute using LBM for Osmotic pressure model

4.2 LBM - FV model

One obvious limitation of solving convection diffusion equation using LB schemes is when diffusion coefficient is low. For example, when particle radius is around $50nm$, diffusion coefficient is in the order of 10^{-12}. Eq. 4.2 gives a relaxation time of close to 0.5 for such a low diffusion coefficient which makes the model unstable. A typical filtration set up will be around $1cm$ in channel height and the thickness of cake formed will be around $1\mu m$. Therefore, to capture the cake formation process, it is necessary to go to very fine scale which demands high computational costs. Also, another disadvantage in LBM is the time step depends on grid spacing unlike other numerical techniques. A grid spacing of 10^{-5} will result in a time step of $u_{conv}10^{-5}$ where u_{con} is the conversion factor for velocity. An experiment lasting for $100min$ of engineering time will need approximately $6\text{x}10^6$ time steps which is impractical.

To address the above limitation for the nano-filtration cake model, LBM solver for solvent is coupled with a finite volume technique to solve for solute particles. An implicit time stepping scheme is used to march forward in time in bigger steps.

4.2.1 Cake predicting model for nano-filtration

As stated earlier, the thickness of the cake formed during the experiments is in the order of few tenths of μm. It can be assumed that such a thin layer of cake will not disturb the cross-flow hydrodynamics. Solvent is solved using LB solver over the entire domain and velocity field is obtained. Instead of solving for solute over whole domain, only a small part in the vicinity of membrane is solved for solute concentration and the rest of the domain is assumed to have the bulk concentration.

The domain height considered for solving solute is taken as 10% of the filtration cell height. The sub domain is solved for distribution of solute using finite volume techniques explained in the Chapter 3. This will result in more than one control volumes to solve for solute inside one lattice of LBM solvent solver. Therefore, there is a need to interpolate the velocity field inside each lattice of LBM solver to use in finite volume solver for solute.

A linear interpolation for velocity field is used for both $x-$ and $y-$ directions. Even though linear interpolation in both directions is not mass conservative, the residuals are observed to be in the order of 10^{-8} which is assumed to be sufficient. Another important assumption made in this model is cross flow hydrodynamics are assumed to be remain unchanged inside 1 min of engineering time. So, time stepping is governed by solute finite volume solver and after every 1 min of engineering time LBM solver is used to obtain new velocity field as build up of cake reduces the flux through membrane and hence the cross flow hydrodynamics. The implementation details is given in Algorithm 4.

4.2.2 Rejection model for nano-filtration with ionic solutes

When the solute particles involved are sea salts, rejection model is more important than concentration polarisation phenomenon. The size of sea salts are in the order of few tenths of nanometer and they cannot be retained fully by membranes. There is always certain amount of solute passing through the membrane based on its size and membrane characteristics. If C_p is the concentration of solute passing through the membrane and C_w is the concentration of solute on the membrane surface, then rejection is defined as

$$R = 1 - \frac{C_p}{C_w} \tag{4.20}$$

input : Lattice points, Initilization of ρ, $\mathbf{u}$, f, g, D, ν
output: ρ, u, p, ϕ

while $\Delta t \leftarrow t + \Delta t$ **do**
  if *rem(t/60)=0* **then**
    while $res < tolerance$ **do**
      for $i \leftarrow 1$ **to** nx **do**
        for $j \leftarrow 1$ **to** ny **do**
          Solve NS equations for solvent using LBM
          ↓
          Compute macroscopic variables
          ↓
          Compute Residual, $res = \sum_{i,j}(u_n - u_{n+1})^2$
        end
      end
    end
  end
  Interpolate the velocity field inside the finite volume grid
  ↓
  Solve CD equation using velocity field obtained by FV technique
  ↓
  Compute volume fraction ϕ
  ↓
  Update viscosity using Eq.4.6 and compute the additional resistance offered by cake using Eq.4.7
end

Algorithm 4: Coupling of LBM solver for solvent and FV solver for solute in nano-filtration

The above relation for rejection is termed true or real rejection. Rejections observed during the experiments are generally termed as observed rejection (R_{obs}) which is

$$R_{obs} = 1 - \frac{C_p}{C_b} \tag{4.21}$$

where in Eq. 4.21, C_b is the bulk concentration of the solute. The difference in the true rejection and experimental rejection values comes from the fact that the concentration on the membrane wall is not the bulk concentration because of the concentration polarisation phenomenon.

The performance of any membrane is characterised by the rejection of different salts. Prediction of rejection is quite a complicated process. This process has lot of

phenomenon involved in it. This is generally done using extended Nersnt Planck equation along with equilibrium partition equations.

4.2.2.1 DSPM-DE model

DSPM-DE is the extension of DSPM (Donnan steric partitioning pore model) originally proposed by Bowen [3] and is based on extended Nernst Planck equation. This equation describes the variation of concentration inside the pores of membrane.

$$\frac{dc_i}{dx} = \frac{J_v}{D_i}[K_i c_i - C_{pi}] - \frac{z_i c_i F}{RT}\frac{d\psi}{dx} \tag{4.22}$$

In Eq. 4.22, F is Faraday constant, c_i is the concentration of species i inside the pore, J_v is the flux through the pores, C_{pi} is the concentration going out of membrane which is called as permeate concentration, z_i is the valency of ion and $\frac{d\psi}{dx}$ is the potential gradient which is given as

$$\frac{d\psi}{dx} = \frac{\sum_{i=1}^{n} z_i \frac{J_v}{D_i}[K_i c_i - C_{pi}]}{(F/RT)\sum_{i=1}^{n} z_i^2 c_i} \tag{4.23}$$

The smaller pore sizes of nano-filtration membranes decreases the convective and diffusive mobility of ions through the membrane. The effects are incorporated in Eq. 4.22 through hindrance factors K_i and D_i. They are expressed as follows

$$K_i = -0.301\lambda_i + 1.022 \tag{4.24a}$$
$$D_i = -1.705\lambda_i + 0.946 \tag{4.24b}$$
$$\lambda_i = \frac{r_{i,s}}{r_p} \tag{4.24c}$$

where in Eq. 4.24, λ_i is the steric hindrance factor of ion i which is the ratio of ion radius ($r_{i,s}$) to pore radius (r_p).

The concentration of ions inside the pore and outside the pore is correlated through equilibrium partition equation. The main difference between DSPM and DSPM-DE model is due to inclusion of dielectric exclusion effect in the partition coefficients. The equilibrium partition equation is as follows with c_i as pore concentration and C_i is the bulk concentration

$$\frac{c_i}{C_i} = \phi_i \exp\left(-\frac{z_i F}{RT}\Delta\psi_D\right) \exp\left(-\frac{\Delta W_i}{kT}\right) \tag{4.25}$$

Eq. 4.25 can be seen as three different phenomenon. ϕ_i represents steric (sieving) effect, $\Delta\psi_D$ gives Donnan exclusion effect and ΔW_i gives dielectric exclusion effect. The dielectric exclusion effect can be expressed by Born solvation energy barrier by

$$\Delta W_i = \frac{z_i^2 e^2}{8\pi\epsilon_0 r_s}\left(\frac{1}{\epsilon_p} - \frac{1}{\epsilon_b}\right) \tag{4.26}$$

where in Eq. 4.26 ϵ_p and ϵ_b are dielectric constants of pore and bulk solution respectively. The bulk dielectric constant is taken as 80 and choice of pore dielectric constant is debatable. It can be calculated by assuming there is a single layer of water molecules attached to the walls of pore. But this assumption might not always give the accurate results. In this work this is used as a fitting parameter to match the experimental results. Along with Eq. 4.25, 4.23, 4.22, there are two more equations to completely describe the rejection model. They are electroneutrality condition inside and in bulk solution.

$$\sum_{i=1}^{n} z_i C_i = 0 \tag{4.27a}$$

$$\sum_{i=1}^{n} z_i c_i + X_d = 0 \tag{4.27b}$$

Eq. 4.27 represents bulk and inside pore electro-neutrality respectively. X_d is the membrane charge density acquired by the membrane and it depends type of the membrane, bulk concentration and type of salt. It can be calculated by the experimentally by measuring the streaming potential at different concentrations and pressures. The membrane charge density directly dependent on zeta potential acquired by the membrane. pH and concentration are two main properties that influences the zeta potential of the membrane.

Another important phenomenon governing rejection of the membrane is the osmotic pressure developed during filtration process. As stated in earlier sections, osmotic pressure in the case of ionic solutes can be found out using Vant Hoff equation which can be expressed as

$$\Delta\Pi = RT(C_{i,w} - C_{i,p}) \tag{4.28}$$

where in Eq. 4.28, $C_{i,w}$ is the wall concentration and $C_{i,p}$ is the permeate concentration. Therefore, flux depends on the concentration of solute on either side of the membrane.

Modelling of rejection involves solving Eq. 4.27, 4.25, 4.22 together. But Eq. 4.22 needs the knowledge of permeate flux, C_p which is not known beforehand. Therefore, a iterative strategy is used to compute rejection coefficient. The implementation of the model is given in Algorithm 5.

input : C_p, **u**, Δt, $maxiter_p$, $maxiter_w$,tol_p, tol_w
output: C_p, C_w, v_w

while *iter* $\leftarrow$ $maxiter_p$ *and* $res_p > tolerance_p$ **do**
  Permeate concentration $C_p^{n+1} = C_p^n + \omega_p(C_p^{n+1} - C_p^n)$
  $\downarrow$
  while *iter* $\leftarrow$ $maxiter_w$ *and* $res_w > tolerance_w$ **do**
    Compute the osmotic pressure and update the flux using the net applied pressure
    $\downarrow$
    Solve unsteady convection diffusion equation using FV
    $\downarrow$
    Compute L2 norm for ϕ, $res_w = \sum_{i,j}(\phi_n - \phi_{n+1})^2$
  end
  Solve Donnan equilibrium partition equation on feed side using for pore concentration Eq.4.25,4.27
  $\downarrow$
  Solve extended extended Nernst Planck equation using Runge Kutta method, Eq.4.22
  $\downarrow$
  Solve Donnan equilibrium partition equation on permeate side using Eq.4.25,4.27 for the permeate concentration
  $\downarrow$
  Calculate Residual, $res_p = \sum_i(C_p^{n+1} - C_p^n)^2$
end

Algorithm 5: Coupling of concentration polarisation with DSPM-DE model

Solving for solvent part is omitted in this model. It is assumed that the cross-flow hydrodynamics will not have any significant effects on the either the rejection mechanism nor the flux. In addition, the solute is solved only in the boundary layer of the membrane where concentration polarisation effects are observed. The velocity profile is given by assuming a constant shear rate along the length of domain.

The solution procedure is started with a guessed value for permeate concentration, C_p. The osmotic pressure is calculated based on C_p and C_w using Vant Hoff equation 4.28. The flux is calculated based on new net pressure applied using osmotic pressure. The convection diffusion is solved for the first time step with permeate concentration as one of the boundary conditions. $L2$ norm for the concentration is computed and the solution loop is continued until the change in concentration in the domain is small enough. Hence, the loop is continued until a pseudo equilibrium is obtained.

Once the convection diffusion solver is converged, the wall concentration is known. Pore concentration on the feed side of the membrane is computed by solving Donnan equilibrium partition equation, Eq. 4.25 and electro-neutrality condition inside the pore, Eq. 4.27. The pore concentration throughout the length of pore is obtained solving extended Nernst Planck equation. This initial value problem is solved using fourth order Runge Kutta method to compute the pore concentration on the permeate side. Once again Donnan equilibrium partition equation, Eq. 4.25 is used along with electro-neutrality condition of bulk solution to compute the bulk permeate concentration. This is done until the permeate concentration converges to the specified tolerance.

Ideally, this has to be done for every ionic species present in the solution. For example, a solution of $NaCl$ has Na^+ and Cl^- ions in it. The concentration distribution of Na^+ ions and Cl^- ions has to be determined based on the diffusivity coefficients of respective ions. Both ions have different diffusivity coefficients and when solved convection diffusion equation for both ions separately, the resulting concentration in the bulk might not satisfy electro-neutrality condition, Eq. 4.27. To avoid this difficulty, the convection diffusion equation is solved for concentration of $NaCl$ as whole rather than solving for Na^+ and Cl^-. The diffusion coefficient of different salts is taken from work of Geraldes et al. [28]. Osmotic pressure is also calculated from the Geraldes work instead of using Vant Hoff equation.

Chapter 5

Results and Discussion

This chapter deals with results of different models discussed in Chapter 4. It starts with the results of benchmark problems for LBM solver and finite volume solver. The next section deals with the results of cake formation in micro-filtration. The kinetics of cake formation is discussed at different applied pressures. Later, concentration polarisation model with solute particle interactions is given. The results for osmotic pressure, gradient diffusion coefficient and particle distribution are discussed in detail. This is followed by the results of nano-filtration. First model discussed is the cake formation in nano-filtration and the final sets of results briefs about the rejection phenomenon in nano-filtration.

5.1 Validation of solvers

The developed LB and FV code are validated with standard benchmark problems. LB solver is validated with Poiseuille flow problem and lid driven cavity flow problem whereas FV solver for convection diffusion is validated with rotating pulse problem and problem demonstrating artificial diffusion using hybrid differencing scheme.

5.1.1 LB solver

The LB solver with $D2Q9$ lattice model is implemented with second order bounce back boundary conditions for wall. The pressure and velocity boundary conditions

are implemented according to Zou and He [15]. The solver is validated with the following benchmark problems.

5.1.1.1 Poiseuille flow

Poiseuille flow results when an incompressible fluid flows between two parallel plates. The analytical solution can be obtained from Navier-Stokes equation and is given by

$$u_x(y) = \frac{-G}{2\nu}\left[\left(\frac{h}{2}\right)^2 - |y|^2\right] \tag{5.1}$$

where in Eq. 5.1, G is the body force that is driving the fluid and h is the channel height. The geometry is shown in Fig. 5.1.

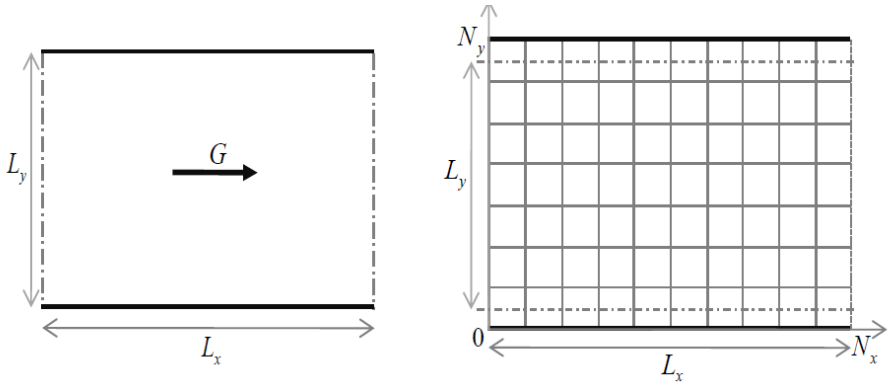

FIGURE 5.1: Domain geometry of Poiseuille flow

The problem is solved by a domain having 1 m in length and 0.24 m in height. Accordingly, 100 lattice units are made in $x-$ direction and 24 lattice units are made in $y-$ direction. The domain is filled with fluid and a body force, G of 0.00011 is given for the flow to develop. Periodic boundary conditions are used at inlet and outlet.

No-slip i.e. second order bounce back boundary condition is used for top and bottom walls. As discussed Chapter 2, second order bounce back assumes wall to be present in between fluid and solid nodes. Therefore, the effective height between the parallel plates in only 23 lattice units instead of 24. An initial condition of $\rho = 1$ and zero velocity condition is used all over the domain.

The flow is allowed to reach a steady state by setting a suitable tolerance for velocity in $x-$ direction. Different parameters used in the simulation are given in Table 5.1.

TABLE 5.1: Different Parameters used in Poiseuille flow problem

Parameters	
Lattice units in x-direction	100
Lattice units in y-direction	24
Viscosity, ν	0.016667
Relaxation parameter, τ	0.55
Body force, G	0.00011
Boundary conditions	
Inlet	Periodic BC
Outlet	Periodic BC
Walls	Second order bounce back
Initial conditions	
x-Velocity, u_x	0
y-Velocity, u_y	0
Density, ρ_0	1

The velocity profile obtained at various times before reaching steady state is shown in Fig. 5.2 .

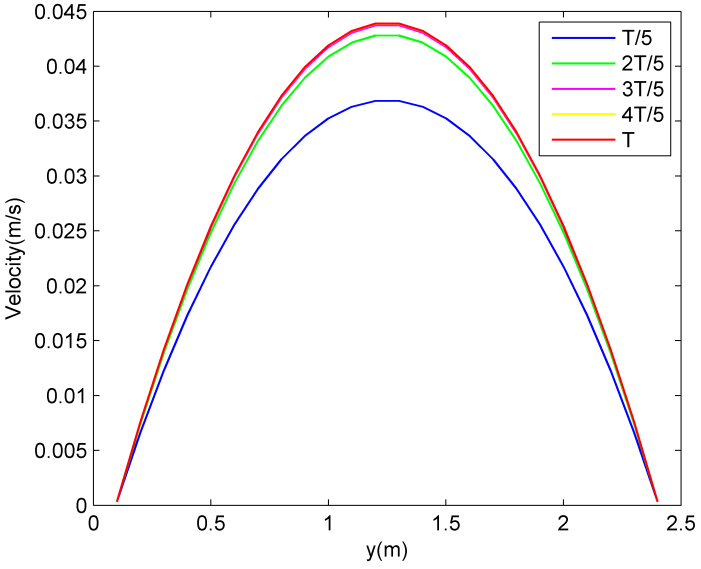

FIGURE 5.2: Development of Velocity profile at the middle section of channel along y-axis

At steady state the profile remains the same at any position in the $x-$direction. The contours of velocity in $x-$direction is also shown in Fig. 5.3. From the contours, the maximum velocity is 0.438 m/s which is at the center of the channel. The maximum velocity can be computed analytically from the Eq. 5.1 by using

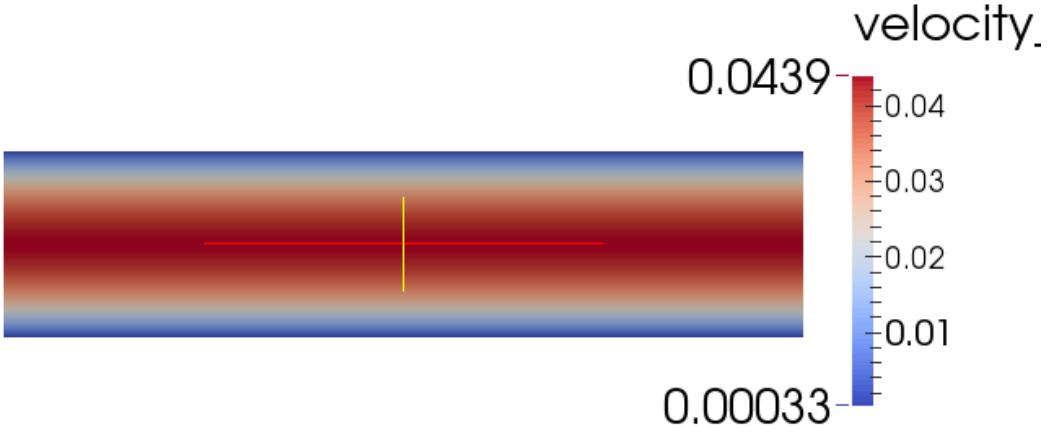

FIGURE 5.3: Contours of x-Velocity in Poiseuille flow

the values given in the Table 5.1 which gives a value of 0.436 m/s and is in very good agreement with the numerical solution.

5.1.1.2 Lid-driven cavity flow

Lid driven cavity problem is one of the standard benchmark problems in CFD. Ghia et al. [29] had done extensive work in the analysis of this problem. Even though there is no analytical solution is available, numerical results obtained are generally compared with that of Ghia et al.

The problem consists of a square cavity having 129 lattice units in both directions. The cavity is filled with a fluid of uniform density. No-slip boundary conditions are applied to two vertical sides and bottom side whereas the top side is given a horizontal velocity of 1 m/s. The geometry of the problem is shown in Fig. 5.4a and Table 5.2 has the different parameters used in the simulation.

The problem is solved at $Re = 100$. The velocity contours are shown in Fig. 5.4b The velocity in $x-$direction is plotted along the $y-$axis through the geometric center of the domain and compared to that of Ghia et al. results. Similarly, velocity in $y-$direction is plotted along $x-$axis through the geometric center. It can be seen from the Fig. 5.5 that the results are in good agreement with Ghia et al. results.

This concludes the validation results for LB solver. The next section deals with the results of validation test of finite volume convection diffusion solver.

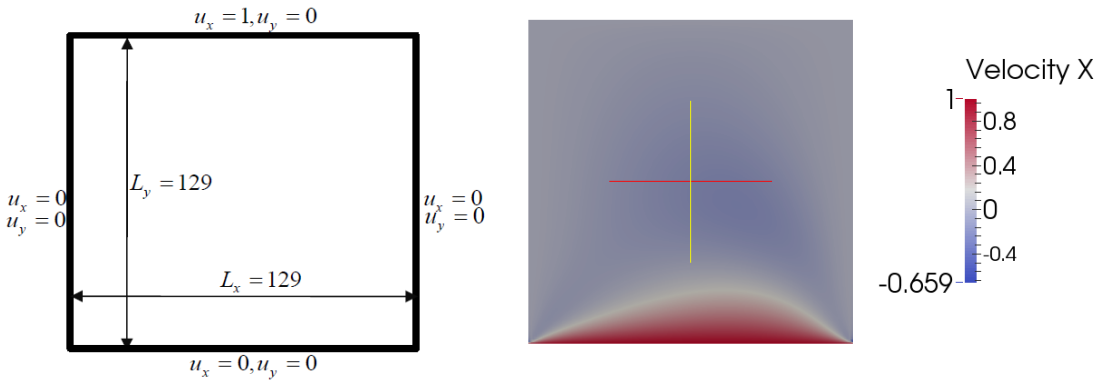

(A) Geomtery of the domain for lid driven cavity flow

(B) Contours of the $x-$velocity in lid driven cavity flow

FIGURE 5.4: Geometry and results of Lid driven cavity problem

TABLE 5.2: Different Parameters used in Lid driven cavity flow problem

Parameters	
Lattice units in x-direction	129
Lattice units in y-direction	129
Viscosity, ν	0.01
Relaxation parameter, τ	0.53
Reynolds number, Re	100
Boundary conditions	
Left boundary	Second order bounce back
Right boundary	Second order bounce back
Bottom boundary	Second order bounce back
Top boundary	Velocity BC, $u_x = 1$, $u_y = 0$
Initial conditions	
x-Velocity, u_x	0
y-Velocity, u_y	0
Density, ρ_0	1

5.1.2 FV solver

The finite volume solver for convection diffusion equation is validated with rotating pulse problem and the problem illustrating false diffusion.

5.1.2.1 Rotating pulse problem

This problem validates the transient convection diffusion equation which uses a hybrid differencing scheme and implicit time stepping. A square domain $(0, 1)$x$(0, 1)$

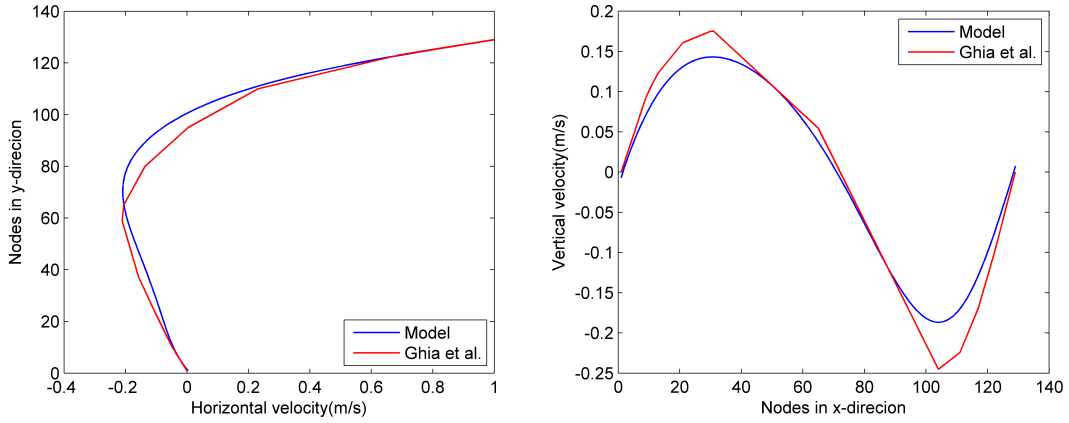

(A) Horizontal velocity taken along vertical axis through geometric center (B) Vertical velocity taken along horizontal axis through geometric center

FIGURE 5.5: Velocity plots taken along different axis

is considered with Dirichlet boundary conditions on all four edges. An initial condition for the field variable is given by

$$\phi(x, y, 0) = \exp\left[-((x - 0.25)^2 + y^2)/2\sigma^2\right] \tag{5.2}$$

In Eq. 5.2, σ is a constant and it governs the radius of the cone and it results in a cone with amplitude 1 centered around $(0.25, 0)$. The velocity field used is proportional to $(-y, x)$ with x and y are co-ordinates of the point. This gives a rotating convective field through which the cone rotates. The problem is solved for one complete rotation at two different grid spacing and a constant time step of 0.01. The contours of the initial condition of field variable is ahown in Fig.5.6. The parameters used are given in Table 5.3.

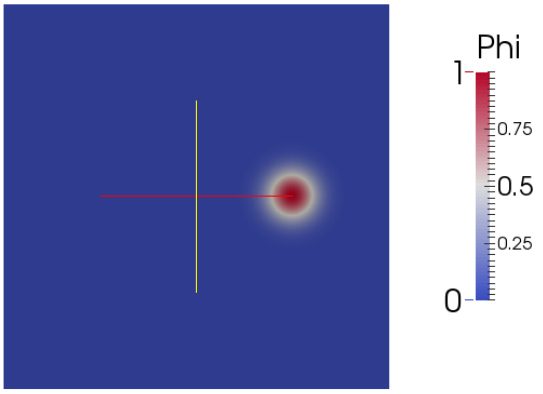

FIGURE 5.6: Initial condition of ϕ with the cone centered around $(0.25, 0)$

TABLE 5.3: Different Parameters used in rotating pulse problem

Parameters	
Divisions in x-direction	144,288
Divisions in y-direction	144,288
Diffusion coefficient, ν	0.0
Constant, σ	0.04
Velocity, u_c	1
Time step, Δt	0.01
Boundary conditions	
All boundaries	Dirichlet BC, $\phi = 0$
Initial conditions	
x-Velocity, u_x	$-yu_c$
y-Velocity, u_y	xu_c
Field variable, ϕ_0	Eq.5.2

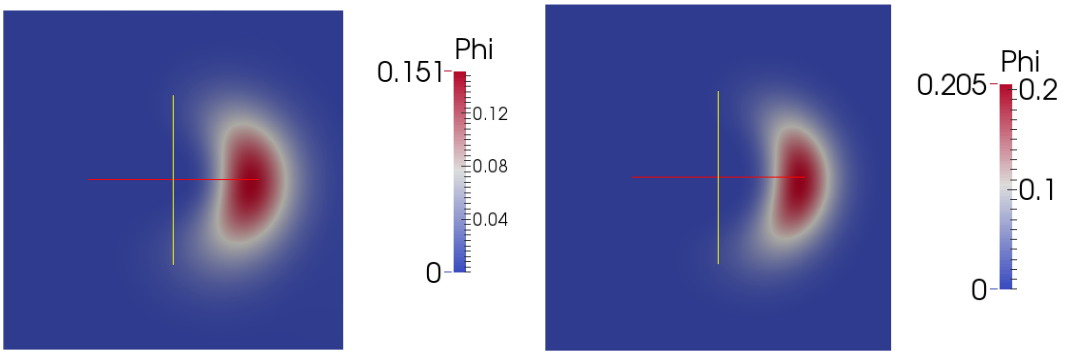

(A) Contours of field variable ϕ for 144x144 mesh

(B) Contours of field variable ϕ for 288x288 mesh

FIGURE 5.7: Contours of field variable

The contours of field variable, ϕ is shown in Fig. 5.7. for 144x144 and 288x288 space discretzations. Even though the diffusion is set to zero, it can be observed from the contours that the peak of the cone is decreased after one complete revolution. This is due to time stepping scheme in this which is implicit and is only first order accurate. When 144x144 discretization is used with a time step of 0.01, CFL number is 1.44 and it require more than 3000 time steps for one complete revolution. The errors at each time step builds up which results in huge decrease in the height of the cone. This can be observed from Fig. 5.7.

But the time stepping used is implicit so the solution is stable. When the space discretization is 288x288, CFL number becomes 0.72 but still the peak amplitude reduces after one revolution. This shows that the solver is behaving as expected and giving reasonable results.

5.1.2.2 False diffusion problem

A square domain of $(0,1)$x$(0,1)$ is considered. Dirichlet BC is applied to all boundaries. The field variable, ϕ is 0 along south and east boundaries and 100 along the west and north boundaries. A uniform velocity field is given over the whole domain where u_x=u_y=2 m/s and is parallel to the diagonal. The geometry of the problem in shown in Fig. 5.8 and different parameters are given in Table 5.4.

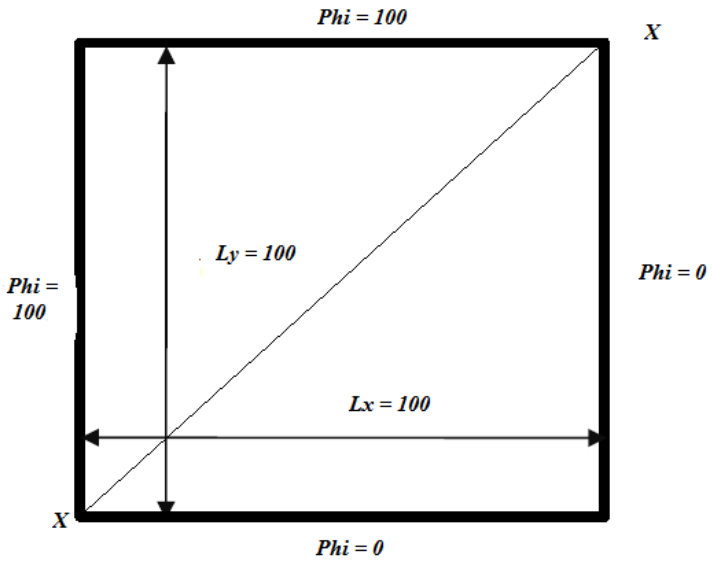

FIGURE 5.8: Domain geometry and shock occurs along diagonal X-X

A pure convective problem is considered with zero diffusion. There is no source term and therefore problem is solved for steady state. As the flow is parallel to the diagonal the value of ϕ at all points above the diagonal should be 100 and below the diagonal it should be zero. There should be a shock at the diagonal. But the hybrid difference scheme produces considerable amount of artificial diffusion and the shock get smeared. This can be illustrated by Fig. 5.9.

As shown in Fig. 5.9 the solution is smeared due to high artificial diffusion when the mesh is relatively coarse and it approaches the actual profile as the mesh is made finer. The smearing of the shock can be observed in the contours of ϕ shown in Fig. 5.10 for mesh of 48x48 and 192x192. The variation of ϕ along diagonal is more spread in the case of coarser 48x48 mesh and it is more sharp in the case of 192x192 mesh.

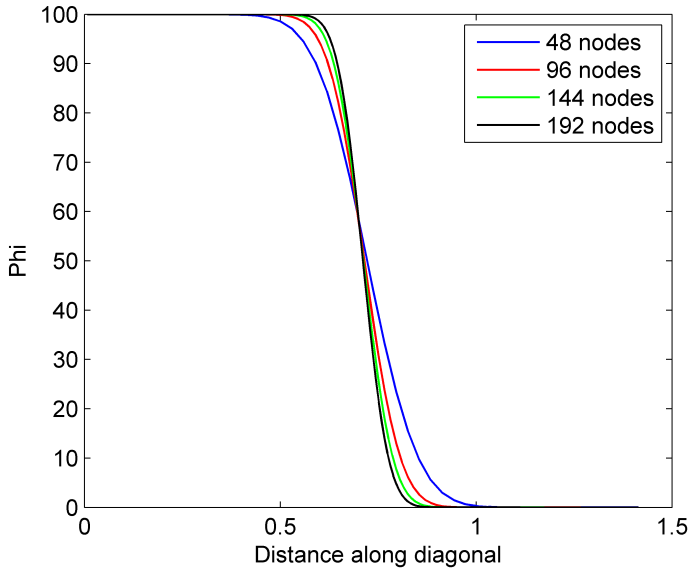

FIGURE 5.9: Variation of ϕ along the diagonal for different meshes

TABLE 5.4: Different Parameters used in false diffusion problem

Parameters	
Divisions in x-direction	48,96,144,192
Divisions in y-direction	48,96,144,192
Diffusion coefficient, ν	0.0
Velocity, u_c	2
Boundary conditions	
South and east boundaries	Dirichlet BC, $\phi = 0$
North and west boundaries	Dirichlet BC, $\phi = 100$

5.2 Micro-filtration results

This section describes the modelling of micro-filtration device and the different results of the model. This particular model is more focussed on cake formation at different applied transmembrane pressures. Different design modifications to the existing model are studied in terms of the amount of flux coming out of membrane.

5.2.1 Model description

The geometry of the filtration device is shown in the Fig. 5.11. The rectangular flow channel has a length, L of $90\mu m$ and a width, $2H_0$ of $36\mu m$. A pressure gradient of 3.0Pa/μm is used and it results in a cross flow with a aveage velocity of 0.32m/s. The thickness of the membrane δ_m is $1.2\mu m$. The length of the membrane

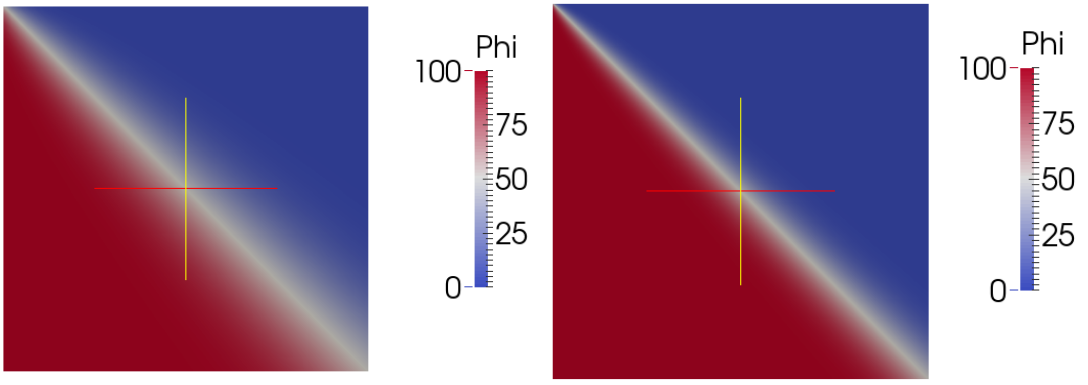

(A) Contours of field variable ϕ for 48x48 mesh (B) Contours of field variable ϕ for 192x192 mesh

FIGURE 5.10: Contours of field variable

is $30\mu m$ and solid walls at inlet side and outlet side are of lengths $15\mu m$ and $45\mu m$. The suspended particles have a mean radius of $2.5\mu m$ and therefore specific cake resistance can be calculated using Eq. 4.7. Pressure boundary conditions are used at the inlet, outlet and the permeate side. The flow is assumed to be fully developed when it enters the domain. Transmembrane pressure (TMP) is defined as pressure difference between either side of membrane at its half way point (L_0).

$$TMP = p_{in} - \frac{L_0}{L}(p_{in} - p_{out}) - p_{per} \tag{5.3}$$

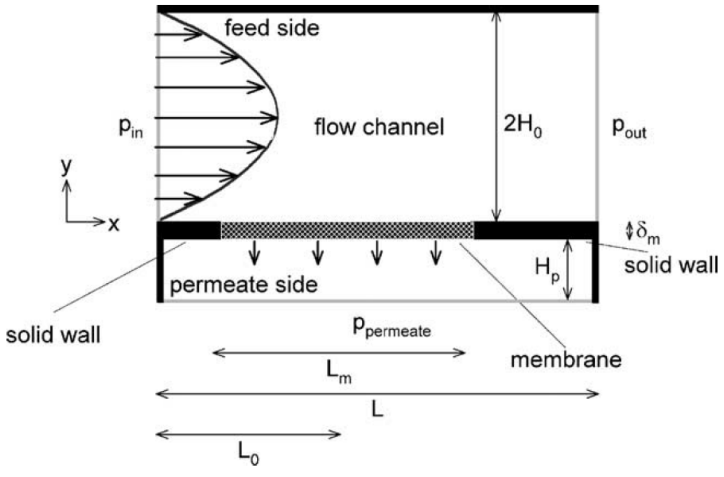

FIGURE 5.11: Geometry of micro-filtration rectangular filtration cell

Bounce back BC is used for fluid for solid walls and body force is applied to fluid for the membrane part as described in porous modelling in Chapter 2. In the case of solute, fixed inlet concentration is used as inlet and outflow BC at the outlet.

The top and bottom boundaries are treated as walls for solute and therefore it is assumed that all the solute particles are retained during filtration process.

This model is solved using LBM for both solute and solvent discussed in chapter 4. Shear induced diffusion is used as the particles are larger than $0.1\mu m$ and 0.6 is the maximum volume fraction for the solute. The different parameters used in the simulation are given in Table 5.5.

TABLE 5.5: Different Parameters used in micro-filtration

Parameters	
Lattice points in x-direction	301
Lattice points in y-direction	133
Diffusion coefficient, D	Eq.4.8
Kinematic viscosity of particle free medium, ν_0	10^{-5} m^2/s
Average velocity, U_0	0.324 m/s
Pressure difference , ΔP	270 Pa
Resistance of membrane, R_m	1.62x10^8 m^{-1}
TMP	1180, 1780, 2980, 4180 Pa
Inlet volume fraction, ϕ_b	0.5
Specific cake resistance, R_c	4.05x10^{13} m^{-2} from Eq.4.7
Boundary conditions	
Inlet for fluid	Pressure BC, p_{in}
Outlet for fluid	Pressure BC, p_{out}
Inlet for solute	Fixed volume fraction , ϕ_b
Outlet for solute	Outflow BC
Initial conditions	
x-Velocity, u_x	Fully developed Poiseuille flow induced by ΔP
y-Velocity, u_y	0
Solute volume fraction, ϕ_0	0.05

5.2.2 Results

5.2.2.1 Effect of transmembrane pressure on cake formation

The effect of transmembrane pressure on cake formation and flux kinetics is studied. The model is run at different TMPs of $1180, 1780, 2980, 4180$ Pa. The model is run at each TMP until steady state is reached. The permeate flux, v_p is the fluid velocity coming out of the membrane. In the simulations, the $y-$velocity at the lattice points immediately preceding the membrane is taken as permeate flux.

The length averaged flux $< v_w >$ is the average permeate flux over the length of the membrane.

$$< v_w >= \int_0^L u_y(x)dx \tag{5.4}$$

The variation of length averaged flux with time at different TMP is shown in Fig. 5.12 It can be observed from the plot that the variation of flux over time is negligible when TMP is lower than 1780 Pa.

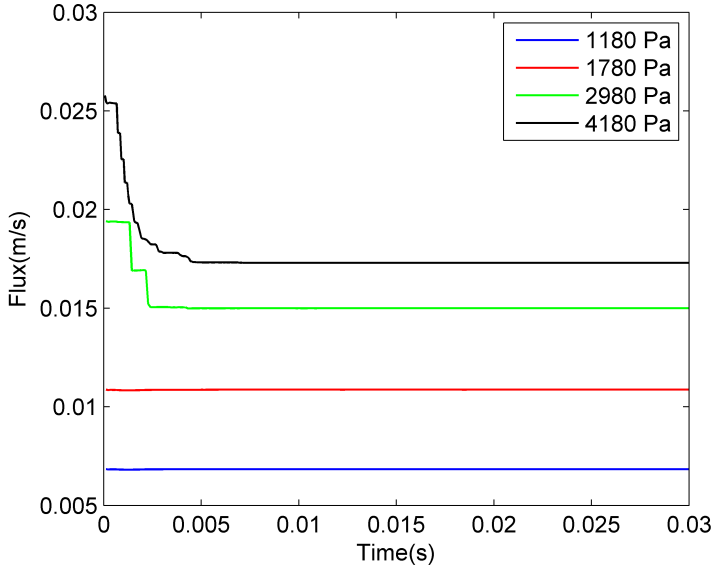

FIGURE 5.12: Flux decline with time at different TMPs in micro-filtration

At higher pressures initial flux is higher and then declines with time reaching a steady state. It can be inferred from the plot that there is almost no cake formation in the cases of TMP less than 1780 Pa. When TMP is 2980 Pa and 4180 Pa, there is significant drop in initial flux and hence cake layer has build up. This can be established by the concentration distribution contours which are shown in Fig. 5.13.

When TMP is 1180 Pa, it can be seen from Fig. 5.13a that there is no cake layer formed over the membrane. There is only concentration build up near the membrane vicinity which is termed as concentration polarisation. On the other hand when TMP is 4180 Pa, there is thick layer of cake formed over the membrane. In all the cases, concentration polarisation can be observed. The phenomenon of cake formation can be explained from Fig. 5.13. The concentration polarisation layer is always first stage of cake formation. When the applied pressure is high

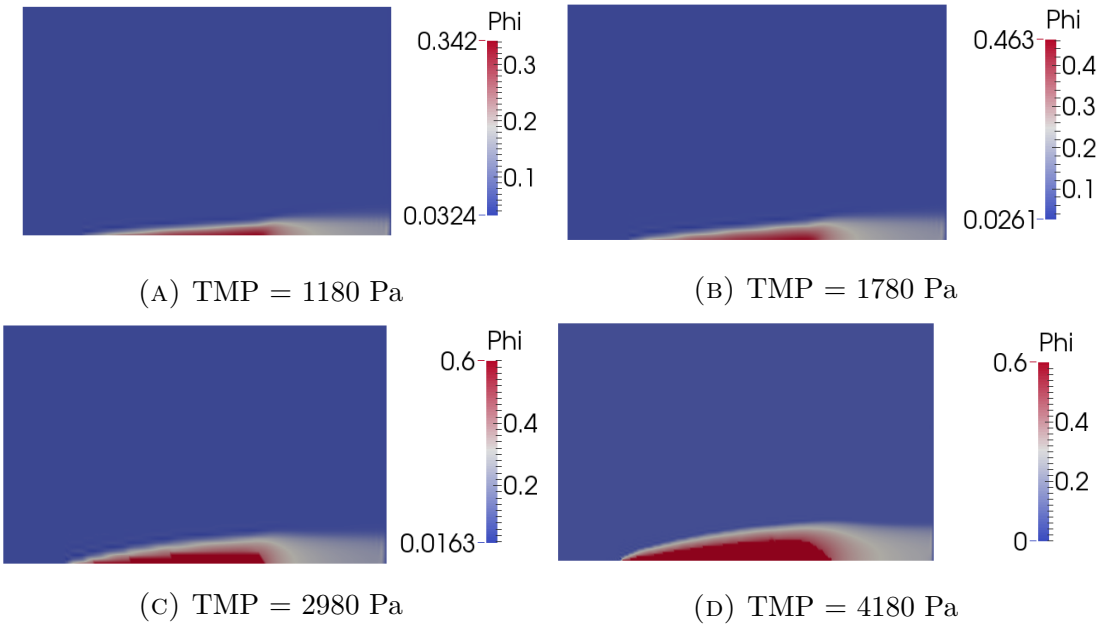

(A) TMP = 1180 Pa

(B) TMP = 1780 Pa

(C) TMP = 2980 Pa

(D) TMP = 4180 Pa

FIGURE 5.13: Concentration distribution at various TMPs in micro-filtration

enough, the concentration inside the polarised layer can go high enough to form a immobile cake layer. Another important point to make in this context is the formation of cake starts to form from right end of the membrane. This is due to higher convective force by fluid on solute particles in cross-flow direction. This is the possible reason for the cake layer thickness to be maximum towards the end of the membrane which is about two-thirds of membrane length.

The steady state flux for TMP 2980 Pa and 4180 Pa is close. But there is a significant difference between steady state flux for TMP 1780 Pa with that of 4180 Pa. This can be due to the cake free zone at the beginning of the membrane in the case of 1780 Pa where the flux is higher.

5.2.2.2 Dependence of membrane length

The simulations are carried out for different membrane lengths of $90\mu m$, $180\mu m$, $270\mu m$ and $360\mu m$ at TMP of 1780 Pa. The model is run till steady state is reached and the flux along the length of the membrane is plotted at steady state in Fig. 5.14.

It can be observed from the plot that flux at the end of the membrane is highest when length is $90\mu m$ and lowest when the length is $360\mu m$. This is due to the variation of TMP over the length of the membrane. From Eq. 5.3, TMP depends on the pressure difference that establishes cross-flow. As the pressure drops along

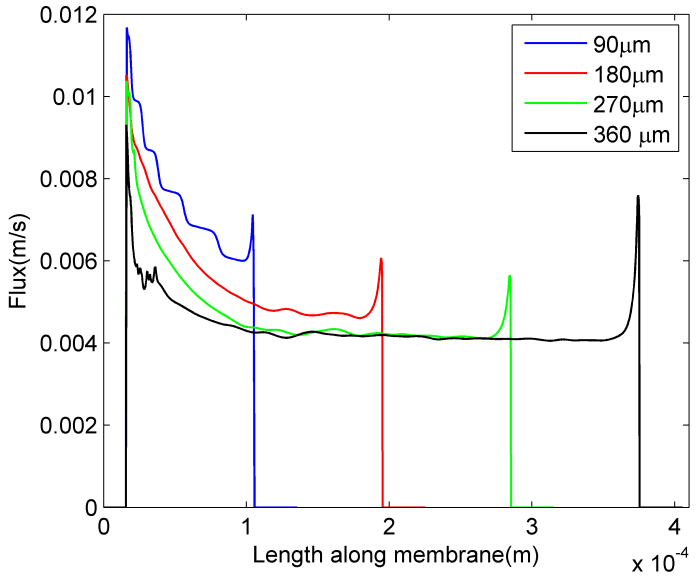

FIGURE 5.14: Variation of flux along the length at different membrane lengths in micro-filtration

the length of membrane, TMP decreases with maximum TMP at beginning of the membrane and lowest at the end of the membrane. This drop will be more significant when the length of membrane is $360\mu m$.

There is a small increase in the flux at the end of membrane and this can be due to the dispersion of concentration polarisation in the wake of cake formed. The length averaged steady state flux for different membrane lengths is shown in Fig. 5.15.

The length averaged flux decreases as the membrane length increases. This is because the pressure difference $(p_{in} - p_{out})$ is kept constant for all different membrane lengths. For a constant pressure difference, increasing the length of the filtration cell will decrease the cross-flow velocity of fluid according to Poisuelle law. Therefore, effectively there is less mass flow coming in when the membrane length is more which lowers the flux through the membrane at steady state.

5.2.2.3 Dependence of geometry of the filtration device

One particular advantage in this model is to be able to predict flux for any geometry. The analytical and semi-analytical methods discussed in the literature are only valid to standard filtration devices. This model can be used to optimize the design of the device to increase the steady state flux. This is discussed here with

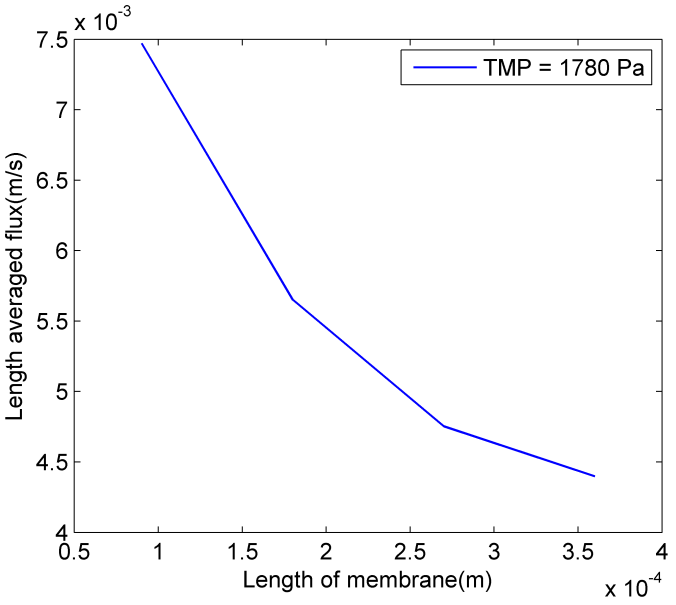

FIGURE 5.15: Variation of length averaged steady state flux with different membrane lengths in micro-filtration

some examples. Firstly, a model with the membrane length of $135\mu m$ is considered. It is stated in the earlier discussion that the flux at the end of membrane becomes slightly higher before falling to zero due to dispersion of concentration. Therefore, instead of having a single membrane, the membrane is divided into 3 parts of $33\mu m$ each with 2 solid walls of length $18\mu m$ separating them.

The flux along the length of the membrane is shown in Fig. 5.16 along with the concentration distribution. This modified design model is compared with the model having the continuous membrane of same length $135\mu m$. It can be observed that the steady state flux is improved with the case of discontinuous membrane due to multiple beginning and ends that increase the dispersion of solute.

This idea of dispersion of solute in concentration polarisation can be used to modify the design further to increase the flux. One of the improvements can be using obstacles in the filtration domain. Obstacles causes a slight turbulence that increases mixing of the solute particles. This is implemented using the discontinuous membrane design. Small triangular obstacles of height $2.7\mu m$ and length at base of $9.9\mu m$ are placed on the solid walls in between the membrane. The results for the steady state flux is shown in Fig. 5.17.

It can be seen from the variation of steady state flux with length of membrane that it does not have a significant influence on the flux compared to the earlier design. This can be due to increased resistance to flow. The barriers will narrow the flow channel there by reducing the shear rate in the domain. As the dominant

(A) Concentration distribution for the membrane with interspaces along its length which are separated by solid walls

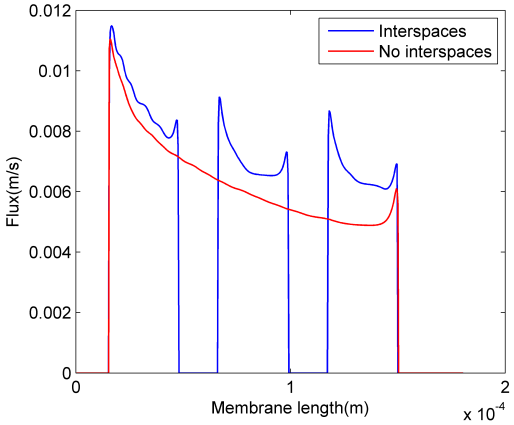

(B) Steady state flux of membrane with and without interspaces along the length of membrane

FIGURE 5.16: Model with interspaces along the membrane and its corresponding comparison with model of same length and without interspaces

diffusion mechanism in the case of micro-filtration is shear induced diffusion and it directly related to shear rate in the flow channel by Eq. 4.8. The decreased shear rate will decrease the back transport of the solute into the bulk and cake formation is more formidable now. This is supported by the fact that the flux obtained is slightly less than the earlier case.

Another possibility to improve flux is to use corrugated membranes. The corrugations are expected to increase the dispersion of the concentration polarisation layer. In this example, corrugations are made on the membrane surface with same material as the membrane. Because the membrane became thicker now the model is run at higher TMP than 1780 Pa. The steady state flux is shown in Fig. 5.18 and it can be observed that flux is increased by significant amount at the near end and the far end of each membrane. This indicates that the corrugations are favourable with membrane interspaces. The flux at the center of membrane is lower in the case of corrugated membranes when compared to the membrane without corrugations. This is again due to the reduced shear rate at that point.

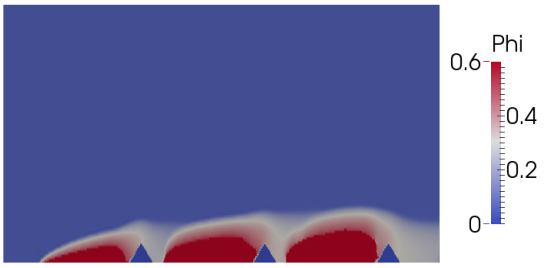

(A) Concentration distribution for the membrane with flow barriers along its length located on the solid walls between membranes

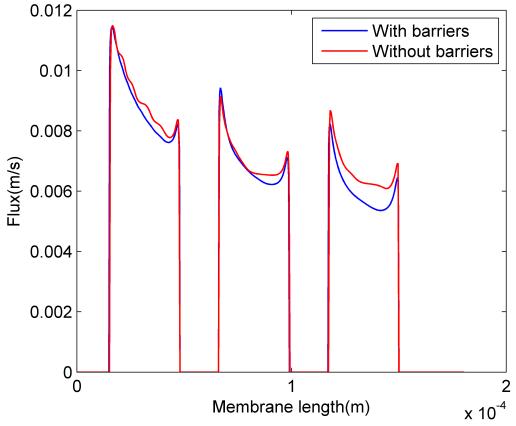

(B) Steady state flux of membrane with and without flow barriers along the length of membrane

FIGURE 5.17: Model with flow barriers along the membrane and its corresponding comparison with model of same length and without flow barriers in micro-filtration

The length averaged flux is over the whole membrane is higher in the case of corrugated membrane.

To conclude, this model could predict the cake formation for different types of geometries and different operating conditions. The model completely resolves the suspension flow and distribution of particles by shear induced diffusion producing more realistic results than existing models. This can be used in design optimization of filtrate systems to increase the flux through the membrane.

(A) Concentration distribution for the membrane with corrugated membranes along its length

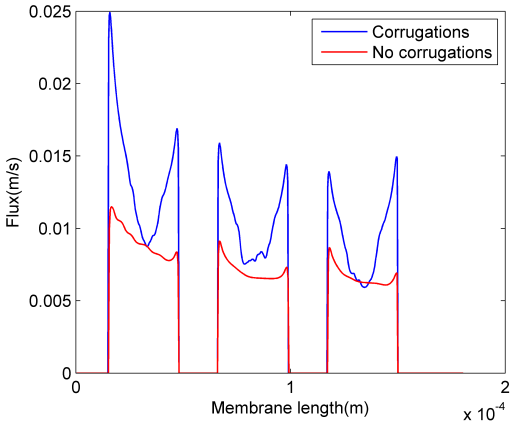

(B) Steady state flux of membrane with and without corrugations of the membrane along its length

FIGURE 5.18: Model with corrugated membrane and its corresponding comparison with model of same length and without corrugations in micro-filtration

5.3 Nano-filtration results with interacting solute particles

As discussed in the earlier chapters, the governing phenomenon in this model is osmotic pressure build up due to solute particles. Osmotic pressure in the case of micro-filtration can be safely neglected due to the bigger size of the particles. Results are presented for gradient diffusion coefficient, radial distribution function and osmotic compressibility. Following this discussion, nano-filtration results are presented for different concentrations and TMPs.

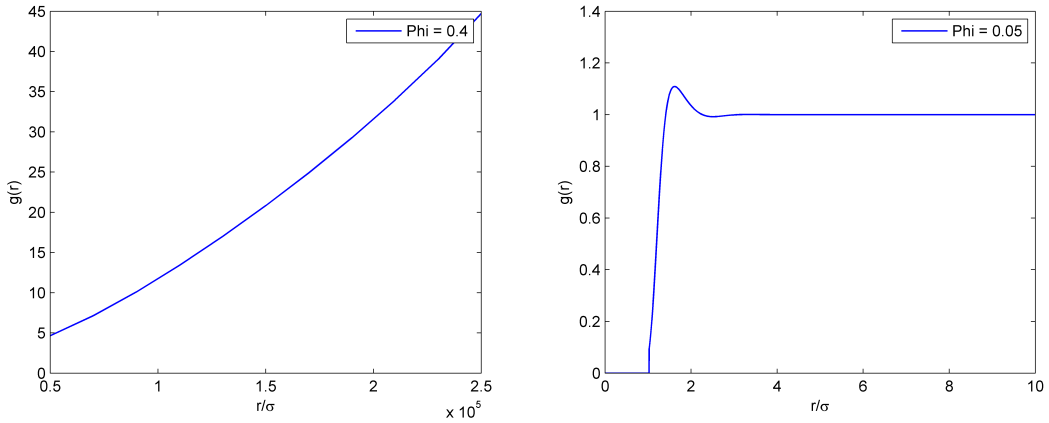

(A) Radial distribution function at $\phi = 0.4$ (B) Radial distribution function at $\phi = 0.05$

FIGURE 5.19: Radial distribution functions at different solute volume fractions and a particle charge z_p 0f -20 and concentration of 0.01M

5.3.1 Solution to OZ integral equation

The numerical procedure to solve OZ integral is briefed in the Appendix B. Long range DLVO interaction potential is used as stated earlier which comprises of van der Waals forces and electrostatic double layer forces. Different parameters used to compute potentials are given in Table 5.6.

TABLE 5.6: Different Parameters used in DLVO interaction potentials

Parameters	
Solute radius, r	3 nm
Charge number on particle, z_p	-20
Electrolyte concentration, $C_{EL}(M)$	0.05
Hamaker constant, $A(J)$	$1.65\text{x}10^{-21}$
Solute volume fraction, ϕ	0 - 0.4
Minimum equilibrium cut off distance , $d_0(nm)$	0.158 nm
Solvent dielectric constant, ϵ	78.54
Temperature,$T(K)$	298

The minimum cut off distance is used to prevent the divergence in van der Waals potential. OZ integral equation is solved for radial distribution function for the above parameters. The plot in shown in Fig. 5.19.

Fig. 5.19 shows the radial distribution function at two different solute volume fractions. When the volume fraction, ϕ is 0.4, $g(r)$ starts from very high value indicating that the probability of finding another solute particle is high. Whereas in the case of $\phi = 0.05$, $g(r)$ starts from almost zero because the solute concentration

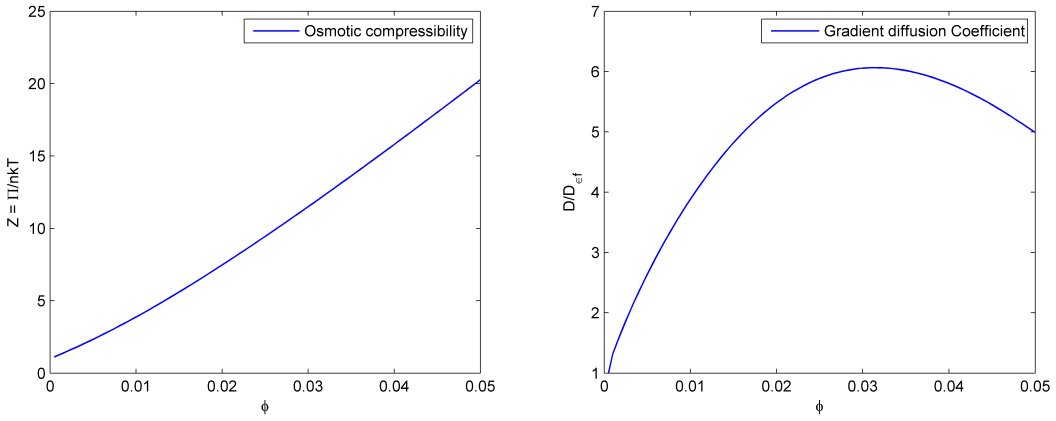

(A) Osmotic compressibility (B) Gradient diffusion equation

FIGURE 5.20: Osmotic pressure and gradient diffusion coefficient as function of solute volume fraction at particle charge z_p 0f -20 and concentration of 0.01M

is very low and probability of finding another solute particle in immediate vicinity is low. Therefore, it can be established that the plots are in line with theoretical predictions.

Once the radial distribution function is obtained, osmotic compressibility and gradient diffusion coefficient can be computed using Eqs. 4.11, 4.16, 4.17. Variation of osmotic pressure and diffusion coefficient with solute volume fraction is shown in Fig. 5.20.

The obtained gradient diffusion function can be fitted into a polynomial function using MATLAB™. The choice of the degree of polynomial can be made based upon the accuracy needed in residuals.

5.3.2 Model description

The geometry of the domain is the same as in Section 5.2. Pressure BCs are used for fluid whereas fixed inlet concentration BCs are used for solute. LB schemes are used to resolve both fluid and solute as discussed in Chapter 4. Different parameters used in the simulation are tabulated below

5.3.3 Results

The results of this model is mainly compared with that of Bhattacharjee et al.[7]. In their work, they solved the simplified convection diffusion equation with finite difference method and assuming a constant shear rate for the fluid and, hence, a

TABLE 5.7: Different Parameters used in osmotic pressure model in nano-filtration

Parameters	
Lattice points in x-direction	301
Lattice points in y-direction	133
Diffusion coefficient, D	Eq.4.16,Eq.4.9
Kinematic viscosity of particle free medium, ν_0	10^{-5} m^2/s
Peclet number, Pe	0.01
Shear rate, $\dot{\gamma}$	100
Resistance of membrane, R_m	1.67x10^{13} m^{-1}
TMP	50-250 kPa
Inlet volume fraction, ϕ_b	0.01-0.05
Boundary conditions	
Inlet for fluid	Pressure BC, p_{in}
Outlet for fluid	Pressure BC, p_{out}
Inlet for solute	Fixed volume fraction , ϕ_b
Outlet for solute	Outflow BC
Initial conditions	
x-Velocity, u_x	Fully developed Poiseuille flow induced by shear rate $\dot{\gamma}$
y-Velocity, u_y	0
Solute volume fraction, ϕ_0	0.01,0.05

simplified cross flow velocity field. The present model uses LB schemes to solve both fluid and solute. Results from both approaches are compared to see any possible differences.

There are some assumptions made when comparing the results of Bhattacharjee et al. with the present model. In their paper, certain details about domain geometry are not provided. The membrane length they used is unity and no data is available about the height of the domain. In the present work, the length of membrane used is $45\mu m$. This is chosen to have a more stable model and fundamentally the hydrodynamics of the model do not depend on the length of the membrane to a large extent. Therefore, all variables are non dimensionalised before comparing.

5.3.3.1 Variation of flux along the length of membrane

The simulations are run for parameters given in Tables 5.7,5.6. A TMP of $200kPa$ is used along with solute volume fraction of 0.01. The variation of permeate flux along the length of the membrane is shown in Fig. 5.21.

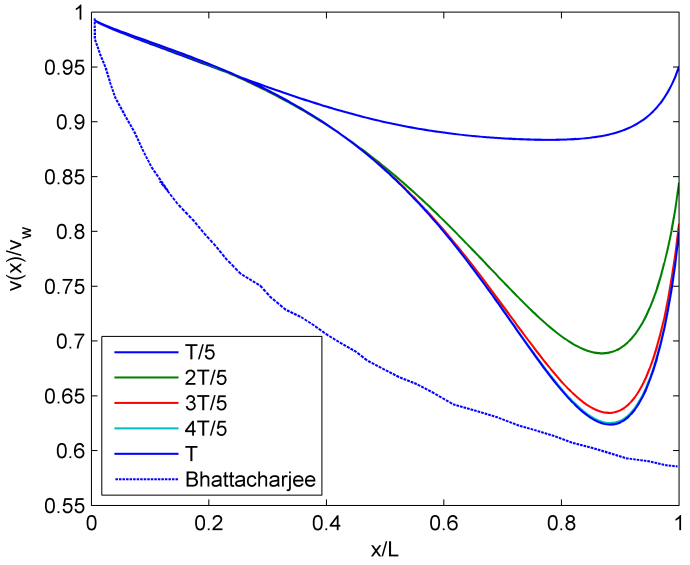

FIGURE 5.21: Variation of flux along the length of membrane at different times in osmotic nano-filtration model at charge density of $-20mC/m^2$ and 0.05M concentration os electrolyte and v_w is flux without any solute.

It can be observed that there is quite a difference between the results of present model and Bhattcharjee et al. The variation of flux in Bhattacharjee's model has approximately a quadratic trend. The slope of the curve is more steep at the beginning of the membrane and it flattens out after one thirds distance from beginning. The present model gives different trend of variation. On contrary, the curve is more flattened at the beginning and has a steep slope after the half way distance from the membrane. Also, it is worth noting that the flux increases slightly at the end of membrane. But the minimum value of non-dimensionlised flux obtained in both models is quite close which is 0.6.

The difference in the results can be due to several factors. Some of them are variation of TMP along the length of the membrane which is not considered in Bhattacharjee's model. In their paper it is stated that Peclet number in $x-$direction is as low as 0.01 in all the simulations. This confirms that the diffusive force is comparable with convective force in $x-$direction. But while solving convection diffusion equation, Bhattacharjee neglected the diffusive flux term in $x-$direction. This simplification is the possible reason for the flux variation trend. Due to the cross flow, the concentration build up starts from the end of the membrane rather than the beginning.

In the plot T is the time taken to reach steady state. At $T/5$, the flux variation is more identical to one from Bhattacharjee's work except for the end which increases slightly due to dispersion of concentration profile as discussed in previous model.

The lowest flux is obtained is around $0.75L$. As the time goes on, the minimum flux over the length decreases and at the same time shifts towards the end of membrane. At steady state, the minimum obtained is just before $0.9L$. The convective force is always same but the diffusive force increases as concentration builds up. This diffusive force will tend to move the peak concentration towards the end of the membrane. The peak concentration is at the beginning of the membrane in Bhattachrajee's model whereas it is the end in the present model. The variation of solute volume fraction over the length of the membrane is shown in the Fig.5.22.

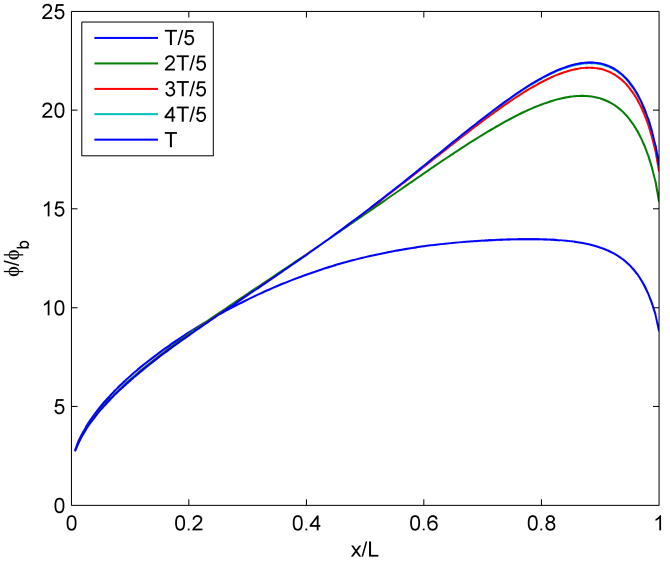

FIGURE 5.22: Variation of solute volume fraction along the length of membrane at different times in osmotic nano-filtration model at charge density of $-20mC/m^2$ and 0.05M concentration os electrolyte and ϕ_b is bulk volume fraction

The peak volume fraction is exactly at the same point as the minimum flux is observed. Hence, the results obtained by the model are very much consistent. The evolution of concentration profile at different times can be visualised as shown in Fig. 5.23.

5.3.3.2 Dependence of flux with TMP

The variation of flux at different TMPs is studied with the present model and compared with Bhattacharjee's model. All the solute parameters are used as in Table 5.6 except for particle charge. A surface charge density ($z_p e/4\pi r_p^2$) of $-20mC/m^2$ is used in present simulations. Rest of the operating conditions and parameters are kept the same. The variation plot is shown in Fig. 5.24.

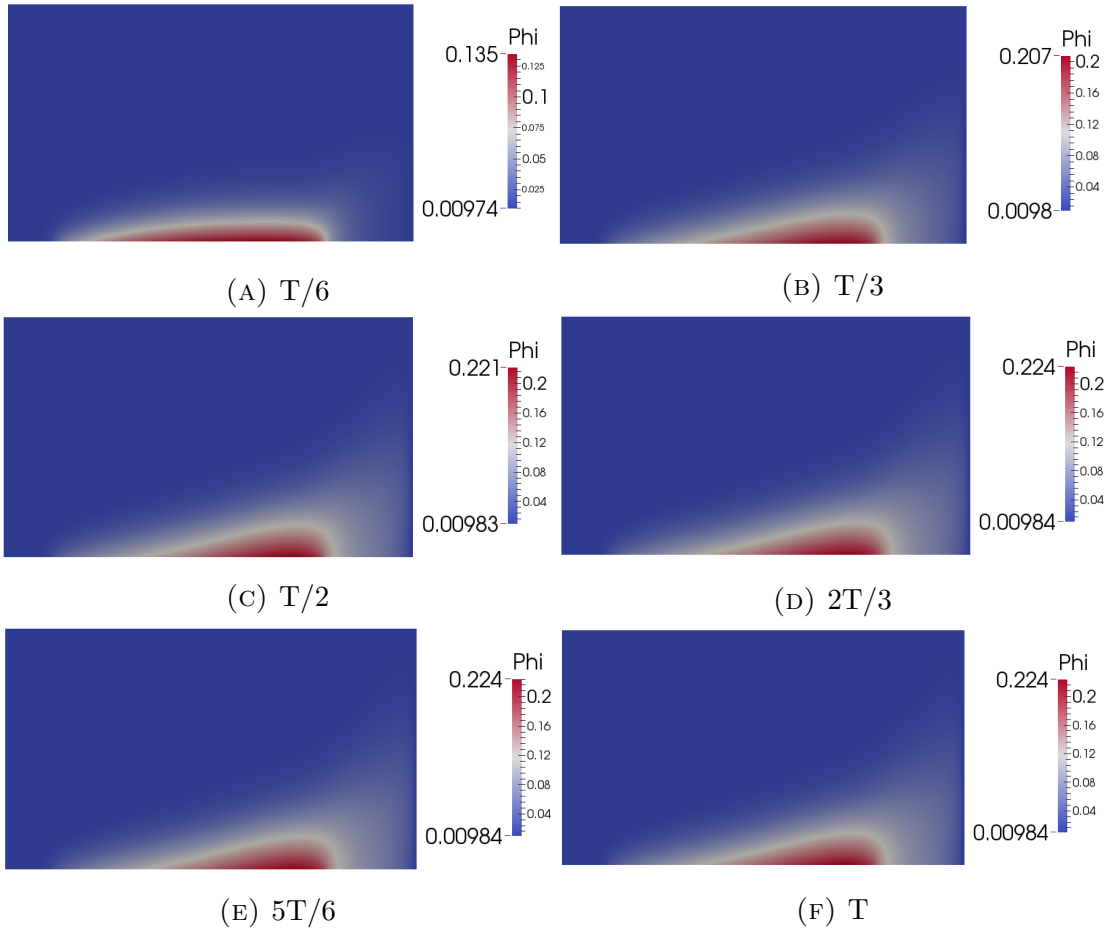

(A) T/6 (B) T/3

(C) T/2 (D) 2T/3

(E) 5T/6 (F) T

FIGURE 5.23: Evolution of concentration polarisation layer in osmotic pressure governed model when TMP is 200kPa and bulk volume fraction is 0.01. Particle charge is -20 and electrolyte concentration os 0.01M

Results from the both models are remarkably same with very small deviation. Therefore, it can be inferred from the plot that the present model is very much successful in predicting steady state flux. The TMP is kept below $250kPa$ to avoid the formation of cake layer. The present model can deal with the cake formation even when TMP is more than $250kPa$ whereas Bhattacharjee's model falls short of it.

Therefore, it can be concluded that the present model is more complete model being able to resolve both fluid and solute and at the same time being able to handle osmotic pressure and cake formation in one single model.

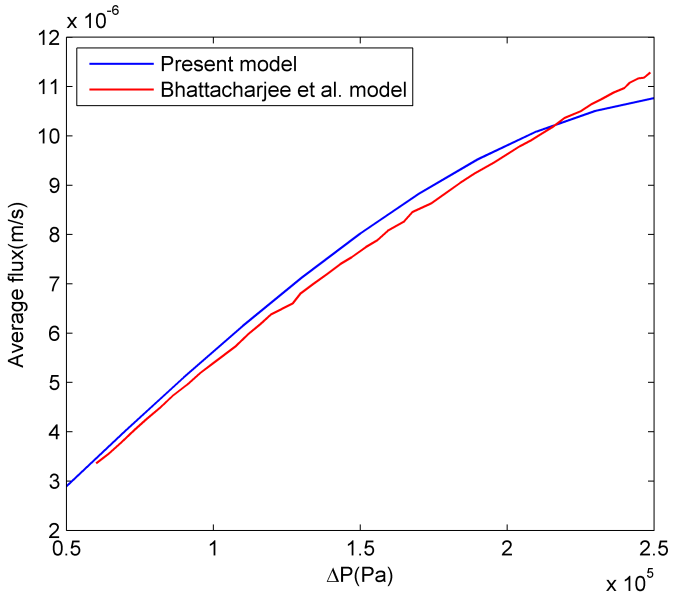

FIGURE 5.24: Variation of steady state flux with TMP in osmotic nano-filtration model at charge density of $-20mC/m^2$ and 0.05M concentration os electrolyte

5.4 Cake prediction in nano-filtration

When the size of solute particles is in the order of few tens of nanometer, the osmotic pressure acting against the TMP is very low. This is because the osmotic pressure is inversely proportional to cube of radius of the solute particle ($\Pi \propto 1/r_p^3$). Therefore, when the TMP is high enough the formation of cake is inevitable.

5.4.1 Model description

The domain geometry considered here is taken from the work of Marion et al.[6]. Marion has done experimental study on the formation of cake with interacting solute particles. In their work the experimental data is used to validate the model they developed for predicting the kinetics of the cake formation. The experimental data is taken from the work and the simulations are performed with present model.

The length of the filtration cell is $12.7cm$ and the height is approximately $1cm$. In the present work only $1/3^{rd}$ of the length is considered to decrease the computational cost. Nevertheless, it proved to be a reasonable assumption in the results. The radius of the solute particles is $60nm$. The Brownian diffusion for the solute particles is in the order of 10^{-12}. The Peclet number in both $x-$ and $y-$directions is more than 1 on a grid spacing as low as 10^{-6}. Hence, the back transport mechanism in the model is almost negligible and this is one of the important reasons

for formation of cake. OZ integral is solved for the present solute particle with the data available from paper [6] to compute the gradient diffusion coefficient. The results showed that the variation of diffusion with particle volume fraction is not significant. So, a constant diffusion model is used rather than using gradient diffusion coefficient.

As stated in earlier Chapter 2 that LB scheme for convection diffusion becomes unstable when the diffusion coefficient is low. The scaling of parameters in LB scheme needs to run a stable model demands a high computational cost. Hence, convection diffusion equation for the solute is solved using FV techniques described in Chapter 3. Fluid is resolved using LB schemes. The algorithm used in coupling both LB and FV techniques is given in Chapter 4. Operating conditions and different parameters used in the model are given in Table 5.8.

TABLE 5.8: Different Parameters used in cake formation model in nano-filtration

Parameters	
Lattice points in x-direction	481
Lattice points in y-direction	89
Finite volume centers for FV CD solver in y-direction	96
Diffusion coefficient, D	3.6x10^{-12} from Eq.4.9
Kinematic viscosity of particle free medium, ν_0	10^{-5} m^2/s
Average cross flow velocity, U_0	0.0001 m/s
Resistance of membrane, R_m	8.11x10^{11} m^{-1}
Specific resistance of the cake layer, R_c	1.23x10$^{17}m^{-2}$
TMP	77 kPa
Inlet volume fraction, ϕ_b	4x10^{-5}
Boundary conditions	
Inlet for fluid	Pressure BC, p_{in}
Outlet for fluid	Pressure BC, p_{out}
Inlet for solute	Fixed volume fraction , ϕ_b
Outlet for solute	Outflow BC
Initial conditions	
x-Velocity, u_x	Fully developed Poiseuille flow with average velocity U_0
y-Velocity, u_y	0
Solute volume fraction, ϕ_0	4x10^{-5}

The cross flow velocity is calculated by computing the mass flow rate depending on the Reynolds number reported by Marion by assuming the diameter of pipe to be around $8mm$. As the present simulations are in $2-D$, velocity per unit

width of the filtration cell is computed and obtained as $10^{-4}m/s$. The specific cake resistance is computed assuming the cake formation occurs at a volume fraction of 0.63. The reason behind this assumption is the interactions of solute particles. Because of different forces acting between the particles they rest in equilibrium with certain distance which depends on relative strength of repulsive electrostatic double layer forces and attractive van der Waals forces. This distance is assumed to be $1nm$ and porosity is calculated using the relation.

$$\epsilon_c = 1 - \phi_{max} \left(\frac{2a_p}{2a_p + h_{eq}} \right)^3 \tag{5.5}$$

where in Eq. 5.5, ϕ_{max} is 0.64 which is maximum packing fraction for non interacting particles and a_p is the radius of solute particle and h_{eq} is the equilibrium distance between solute particles.

5.4.2 Results

The model is run at an inlet volume fractions 4x10^{-5}. The variables of interest in the present case is decline of flux with time. The results from the model is compared with that of experimental data. The plot of flux versus time is shown in Fig. 5.25.

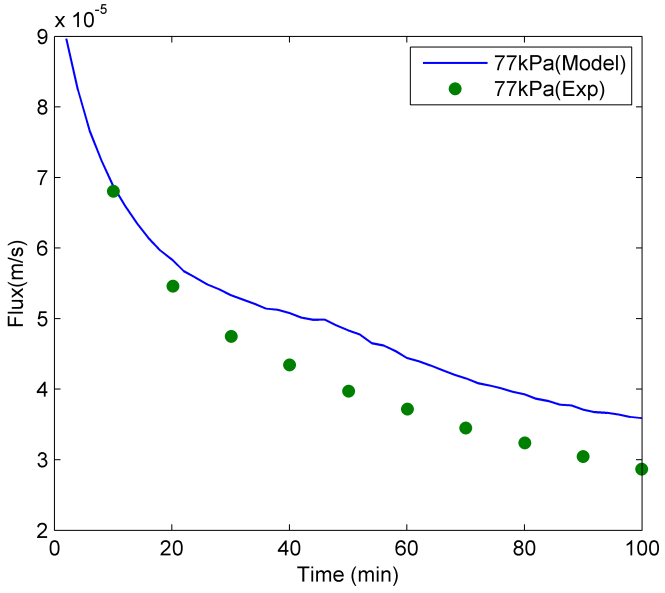

FIGURE 5.25: Flux decline with time in the case of 60nm particle size and bulk volume fraction is 4x10^{-5} under TMP of 77kPa

It can be observed that the model and experimental data is very much in agreement. Other important variables in this study is fouling half life membrane ($t_{1/2}$). This time is defined as the time required for the permeate flux to reduced by half of initial value. This fouling time is defined with another parameter which is $3\tau_m$ where τ_m is time required for flux to become $v_0/\sqrt{2}$. The experimental values and values obtained from the model are given in Table 5.9.

TABLE 5.9: Fouling life values of experiment and model

Variable	Exp Data	Model
τ_m	667 s	700 s
$t_{1/2}$	2000 s	2800 s
v_{100}/v_0	0.31	0.35

Marion's model is based on simplification done to convection diffusion equation by using appropriate boundary conditions which ends up with a ordinary differential equation (ODE) which can be integrated in time. The experimental values of porosity are used to fit the model data to experimental data. Hence, a knowledge of experiment is necessary beforehand in the model of Marion et al. In the present model, no experimental data is used in modelling and still able to predict the cake formation to a good accuracy. This is because of resolving all the possible components in the filtration system. This shows the versatility of the present model. This is confirmed by simulating another experiment with fairly different operating conditions.

The experimental data considered here is extracted from the work of Hong et al.[30]. The solute particle diameter in their experiments is $150nm$ and $300nm$. Because of the larger particles, the diffusion of the particles is even less compared to previous model. The paper reported of almost zero interactions between solute particles and hence a constant diffusion is used in simulations. The TMP is varied between $61 - 20kPa$. The filtration cell is cylindrical in their experiments but a rectangular channel is used in the present study as a simplified $2 - D$ model. The height of the channel if $7mm$ and a length of $0.6cm$ is used to reduce computational cost. It is also stated in the paper that cross flow velocity almost has no influence of flux decline. Therefore cross flow velocity is chosen based on the stability limits of the model. The inlet volume fraction is 10^{-4} in all cases. Membrane resistance is around $10^{12}m^{-1}$ and specific cake resistance is computed using a porosity (ϵ_c) of 0.37 from Eq. 4.7.

The results of flux decline at three different TMPs is shown in Fig. 5.26a along with the corresponding experimental data.

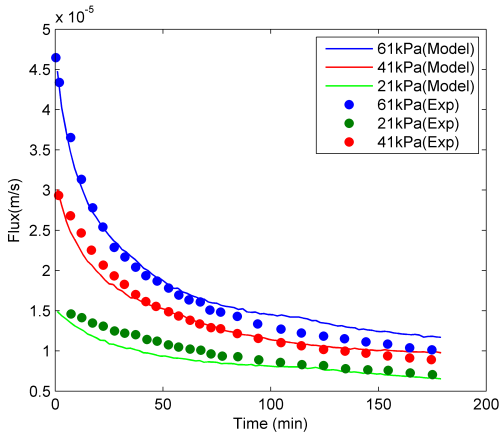

(A) Flux decline with time in the case of 150nm particle size under TMP of 21-61kPa

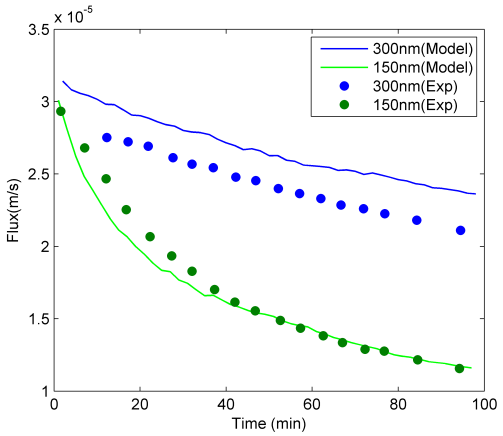

(B) Flux decline with time in the case of 150nm and 300nm particle size under TMP of 41 kPa

FIGURE 5.26: Results of flux decline for different TMPs and different particle sizes and bulk volume fraction is 10^{-4}. Experimental data of Hong et al.

The results of flux decline with time for different sizes of solute particles are shown in Fig. 5.26b. As the size of the particle increases, specific cake resistance decreases based on Eq. 4.7. Hence it can be observed in the results that the flux decline in the case of $300nm$ diameter particles is not significant when compared to that of $100nm$ diameter particles.

It can be concluded from the plot that the model results are in a very good agreement with the experimental data. In their paper, Hong et al. used a different approach in modelling the flux decline compared to Marion et al. Both of their approaches are formulated based upon the operating conditions of the experiments. For instance, Marion's model takes the account of interactions between the solute particles and used the equilibrium distance (h_{eq}) at different conditions to compute porosity and thereby varying the specific cake resistance with time. On the other hand, Hong et al. also simplified the convection diffusion equation by applying appropriate boundary conditions and then calculating the pressure drop across cake layer by using cake resistance thickness and treating permeate flux as time dependent variable. They used constant porosity in all calculations.

The present model could match the results of both experiments using same approach unlike the different approaches the authors took in [6] and [30]. Therefore, it can be established that the present model is more generally in its approach and can be applied to variety of operating conditions without any major changes to the model.

5.5 Nano-filtration rejection model

When the solute particles are ionic in nature or when the size of certain organic solute particles is much smaller than the size of the pores of the membrane, rejection of the solute characterises the membrane. In the present model, rejection of sea salts like $NaCl$ and Na_2SO_4 are computed and compared with experimental data.

The algorithm of the model is explained in Chapter 4. As mentioned earlier, instead of solving for solute distribution of each ionic species, whole salt is treated as one entity and solved based on diffusion coefficient and osmotic pressure provided by Geraldes et al.[28]. Table 5.10 gives the different properties of different salts considered in present work.

TABLE 5.10: Properties of salts provided by Geraldes

Salt	Diffusion coefficient $(10^{-9}m^2/s)$	Osmotic pressure $(10^5 Pa)$
$NaCl$	$1.61(1-14\omega)$ for $\omega < 0.006$,1.45 for $\omega > 0.006$	805.1ω
Na_2SO_4	$1.23(1-0.76\omega^{0.4})$	$337.8\omega^{0.95}$

The solution algorithm involves solving system of non-linear equations in each iteration. Non-linear system of equations results from equilibrium partition equations and electro-neutrality equations Eqs. 4.25, 4.27. The equations are solved using hybrd1 subroutine which is the part of minpack library [31]. The subroutine uses modified Powell hybrid method [32] and Jacobian is calculated using forward-difference approximation.

5.5.1 Model description

As stated earlier, solving for the fluid part is eliminated in rejection modelling. Hence, only convection diffusion equation is solved for computing the distribution of concentration in the boundary layer of the membrane. This is followed by DSPM-DE model to estimate the permeate concentration. The convection diffusion equation is solved in the domain height approximately 10% of the filtration domain. Two commercial membranes are used in the present work namely NF90 and NF270. Various properties of these membranes are given in Table 5.11.

The properties of individual ions that are necessary in DSPM-DE model are given in Table 5.12.

TABLE 5.11: Properties of nano-filtration membranes NF90 and NF270

Membrane	Permeability (m/s.bar)	Thickness /Porosity	Pore size (nm)	Zeta potential (mV) at pH = 7
NF90	1.68x10^{-6}	0.18	0.55	-26.2 - -30.3
NF270	4.18x10^{-6}	0.157	0.71	-12.1 - -15.2

TABLE 5.12: Properties of different types of ions

Ion type	Diffusion coefficient (m^2/s)	Radius (nm)	Valency
Na^+	1.33x10^{-9}	0.184	+1
Cl^-	2.03x10^{-9}	0.120	-1
SO_4^{-2}	1.06x10^{-9}	0.231	-2

The rejection of different salts at different operating conditions are calculated and compared with the experimental data. The results are presented in the following section.

5.5.2 Results

The rejection model is first checked with the results available from literature. The model is used to compute the rejection of $NaCl$ at different bulk concentrations and different TMPs. The experimental data is taken from the work of Mohammad et al.[33]. The effective membrane charge density has to be computed experimentally using streaming potential measurements. But in their work, Mohammad et al. fitted the experimental salt rejection data to compute membrane charge density. The obtained values are fitted through Freundlich isotherm form which depends on the bulk concentration. The fits for both membranes are as follows

$$|X_d| = 3.259 C_b^{0.6985} \tag{5.6a}$$

$$|X_d|/C_b = 1.107 \exp(-0.0056 C_b) \tag{5.6b}$$

In Eq. 5.6, first one is for NF90 and second fit is for NF270 membrane respectively. The charge density is computed at every concentration and is used in computation of rejection coefficient.

In the work of Mohammad et al. mass transfer of the solute ions is considered and not the concentration polarisation. The wall concentration is calculated by the following relation

$$\frac{C_w - C_b}{C_p - C_b} = \exp(\frac{J_v}{k}) \tag{5.7}$$

where in Eq. 5.7, J_v is permeate flux and k is mass transfer coefficient. Mass transfer coefficient depends on filtration cell domain and operating conditions of the experiment. Unlike this approach, the wall concentration in present work is computed by solved convection diffusion equation which makes more physical sense. When the inlet concentration is high, the concentration polarisation phenomenon is significant and has to be taken into account. Hence doing so, there are some observations were made in two approaches.

Mohammad et al. computed the dielectric exclusion effect from Eq. 2.31 and pore dielectric constant is estimated using the relation proposed by Bowen and Welfoot.

$$\epsilon_p = 80 - 2(80 - \epsilon^\star)\left(\frac{d}{r_p}\right) + (80 - \epsilon^\star)\left(\frac{d}{r_p}\right)^2 \tag{5.8}$$

In Eq. 5.8, $\epsilon^\star$ is taken as 6 and ϵ_b as bulk dielectric constant which is 80. DSPM-DE model gave unrealistic results when this relation is used to estimates ΔW_i in the present model. One possible reason might be the effective membrane charge density which is fitted back from rejection results which uses the above relation in computing dielectric exclusion effect. Therefore, pore dielectric constants are chosen for each concentration to obtain the best fit for the rejection coefficient.

Table 5.13 gives the values of ϵ_p for different concentrations of $NaCl$ for NF270 membrane.

TABLE 5.13: Fitted values of ϵ_p at different NaCl for NF270 membrane concentrations

Concentration (mol/m^3)	ϵ_p
427	35.6
342	38.9
256	43.6
171	45.7
85	45.9

The variation of ϵ_p is quite narrow compared to concentration, nut nevertheless it takes values more than 33.1 which results from Eq. 5.8. As there are no

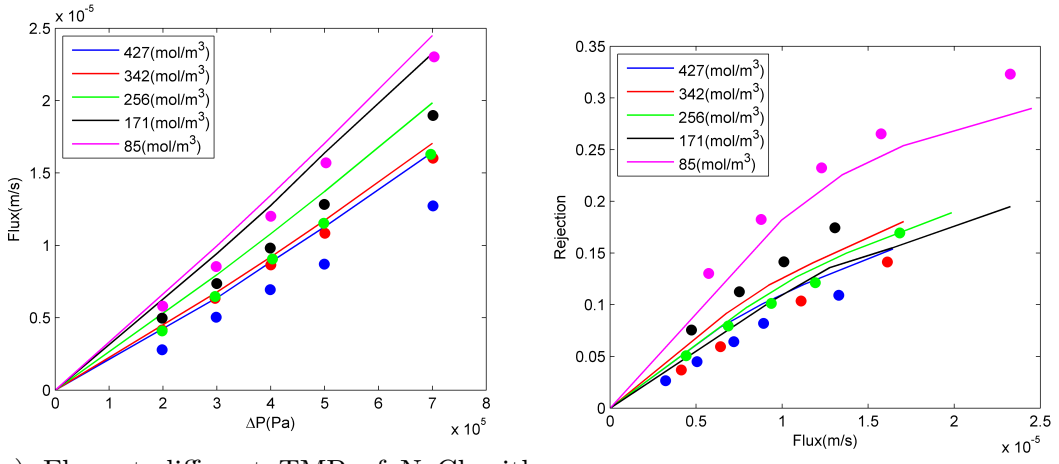

(A) Flux at different TMP of NaCl with NF270

(B) Rejection of NaCl in NF270 membrane

FIGURE 5.27: Flux and rejection data of NaCl at various concentrations and TMPs in NF270 membrane. Dots represent experimental data by Mohammad et al. and solid lines indicate model

streaming potential measurements from the work of Mohammad et al., it is quite difficult to establish the obtained pore dielectric constants are correct. But the combined effect of the membrane charge density and the above ϵ_p values produced the reasonable rejection results.

The rejection and steady state flux of $NaCl$ at different TMPs with NF270 membrane is shown in Fig. 5.27.

The model predicts the rejection and flux at various pressures and concentration to a good agreement with experimental data. This shows the fitting of ϵ_p is reasonable and justified. The use of data given by Gerldes [28] for osmotic pressure and diffusion coefficient is also well agreed. The rejection coefficients vary along the length of the membrane and are calculated taking the mean of the entire membrane. The variation and concentration polarisation plots are discussed in next set of results where the experimental data is obtained from the collaborators of present work.

The same procedure is followed for NF90 membrane for predicting flux. The pore dielectric constant ϵ_p is chosen to fit the experimental rejection. The fitted values of ϵ_p are given in Table 5.14.

The dielectric constant of pore in the case of NF90 membrane is higher than in the case of NF270 membrane for same concentration of solute. This is due to difference in membrane charge density between the both membranes. NF90 has relatively higher membrane charge density values compared to NF270. Hence, the

TABLE 5.14: Fitted values of ϵ_p at different NaCl for NF90 membrane concentrations

Concentration (mol/m^3)	ϵ_p
342	47.9
256	45.6
171	43.7
85	42.0

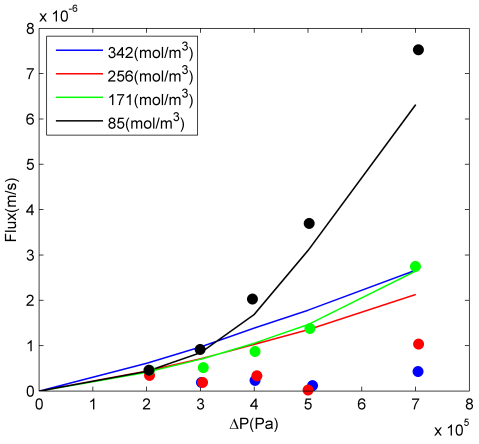

(A) Flux at different TMP of NaCl with NF90

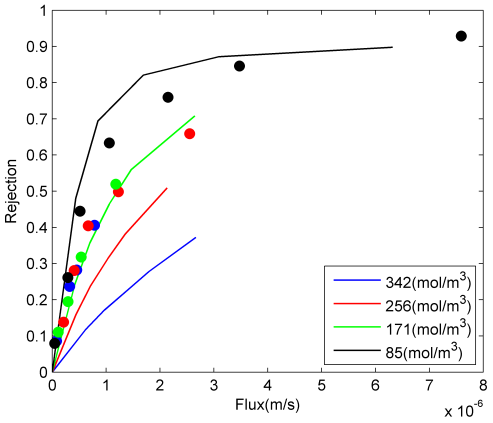

(B) Rejection of NaCl in NF90 membrane

FIGURE 5.28: Flux and rejection data of NaCl at various concentrations and TMPs in NF90 membrane. Dots represent experimental data by Mohammad et al. and solid lines indicate model

concentration of counter-ions (ions having opposite sign as membrane) decreases on the membrane and eventually inside the pore. Lower counter ions inside the pore lowers the interactions between co ions (ions having same sign of charge as membrane) and counter ions decreases the interaction energy. The decrease in interaction energy which is Born solvation energy in the present case is possible when the pore dielectric constant is lower.

The flux and rejection of NF90 membrane for $NaCl$ is shown in Fig. 5.28.

The experimental results provided by the collaborators of the present work are discussed below. The membranes used by them are also NF90 and NF270. The value of zeta potential is available in the for these membranes for $NaCl$. The values are tabulated in Table 5.11. The membrane charge density is not available with the experimental data and hence computed analytically assuming that the zeta potential does not vary much with TMP. pH is kept constant in all cases through out each experiment. Membrane charge density is related to zeta potential by

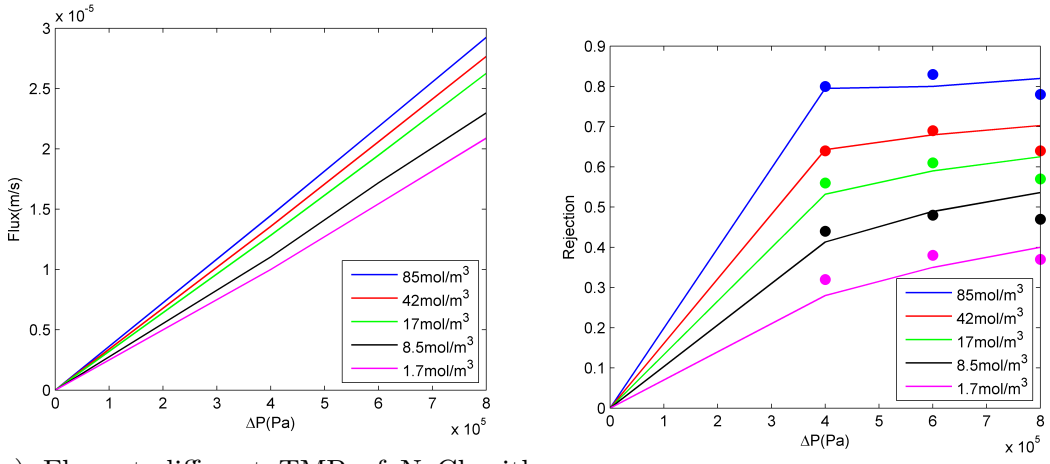

(A) Flux at different TMP of NaCl with NF270

(B) Rejection of NaCl in NF270 membrane

FIGURE 5.29: Flux and rejection data of NaCl at various concentrations and TMPs in NF270 membrane. Dots represent experimental data and solid lines indicate model

$$X_d = 2\left[2\epsilon_0\epsilon_b kT\sum_i C_i N_A\left(\exp\left(-\frac{z_i e\zeta}{kT}\right)-1\right)\right]^{0.5}/r_p F \tag{5.9}$$

In Eq. 5.9, ζ is zeta potential, C_i is the concentration of i^{th} ion, r_p is radius of pore.

The value of dielectric pore constant is kept fixed at 48 at all the concentrations. The ionic concentrations involved in the present experiments are very dilute and hence there will not be much interactions between co ions and counter ions inside the pore. The results for flux and rejection are shown un Fig. 5.29.

In this case the variation of permeate concentration along the length of the membrane is studied. Two cases with bulk concentration at $5g/L$ and $1g/L$ are presented here. The variation of C_P is shown in Fig. 5.30.

The variation is as expected with lowest permeate concentration at the beginning of the membrane and increasing along the length. The trend of permeate concentration is almost identical in both cases when bulk concentration is $5g/L$ and $1g/L$. These plots proves that the concentration polarisation cannot be neglected while modelling rejection phenomenon especially when the bulk concentration is significant. In the case of dilute solutions, concentration polarisation can be safely neglected.

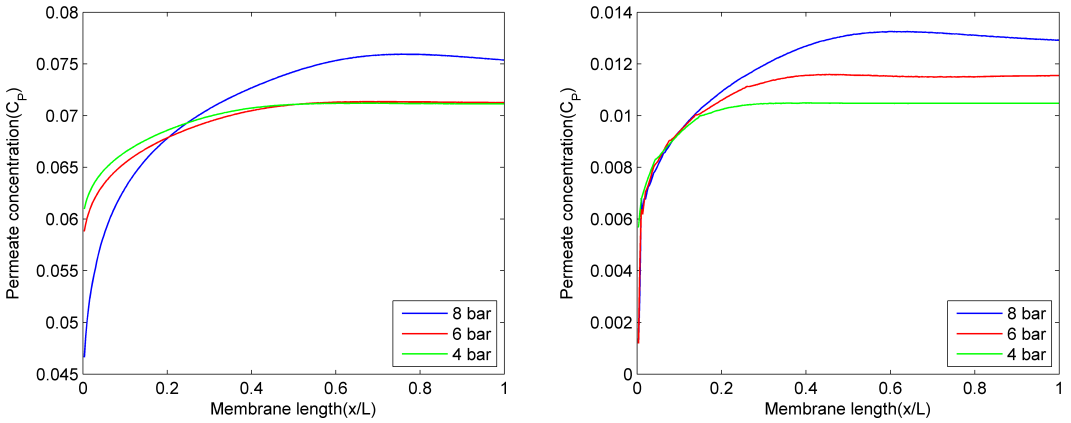

(A) Variation of C_P along membrane length when bulk concentration is 5g/L

(B) Variation of C_P along membrane length when bulk concentration is 1g/L

FIGURE 5.30: Variation of C_P along membrane length for different bulk concentrations and different TMPs for $NaCl$ in NF270 membrane

Chapter 6

Conclusions and Future work

The importance of filtration process is briefed along with the challenges faced in simulating the process. Membrane filtration is discussed in detail and phenomena like concentration polarisation and cake formation is explained in detail.

Lattice Boltzmann methods along with finite volume techniques are used to model the membrane filtration process. The results of micro filtration in a micro sieve are presented for different TMPs and possible design optimizations are studied. Lattice Boltzmann schemes which are used to resolve both solute and fluid has given a very good results and can be used in industrial applications to study the membrane filtration more in detail. But one drawback with LB schemes is complexity involved in using non-uniform lattice grids. The scaling necessary for the LB schemes can be a bottleneck to implement them for different membrane filtration cases. For example, consider a micro-filtration model in practical filtration cell which has dimensions of around 10cmx1cm. Because of high aspect ratio of the filtration cell, the number of lattice points required to simulate the process resolving the scales as low as μm is difficult. The simulations demands a lot of computational resources and also results in stability issues. One solution to increase the stability of LB schemes is to use multiple relaxation time schemes. In the present work, only single relaxation time is used and some stability issues are experienced. Another solution is to use turbulence model while solving for fluid. Turbulence model increases the relaxation parameter above the stability limit of 0.5 giving more stable results. In this work,finite volume techniques are introduced to address the shortcomings of the LB schemes.

A coupled LB finite volume solver for resolving fluid and solute particles respectively is introduced in modelling cake formation in nano-filtration. This model uses

LB implementation for fluid and finite volume techniques for solute and this implementation could capture the cake formation resolving to a scale of few tenths of micro meter without losing generality of the solution process. The model is validated with experimental results from two different experiments. The results from both simulations agreed with the corresponding experimental data within 20%. Therefore, this model can be regarded as more general model having a wide applicability range.

Osmotic pressure governed model is also implemented with LB schemes for both fluid and solute. There are no direct relations to compute the osmotic pressure for non-ionic solute particles where as Vant Hoff equation can be used in the case of ionic solutes. The numerical procedure to evaluate osmotic pressure using OZ integral equation and virial equation of state is briefed. This solution will help in the case when there is no or very less experimental data is available for osmotic pressure of solute particles. Various results like variation of flux with TMP and along the length of the membrane are discussed in detail and compared with other models. There are some differences are observed in the results especially in the case of concentration distribution over the membrane. But the computed flux at various TMPs are in very good agreement with the models available in literature. This shows that the assumptions such as constant shear rate, constant TMP over the whole domain has some major influences on the results.

Another important model in membrane filtration is rejection modelling in nano-filtration. DSPM-DE model is implemented in the present work to compute the rejection coefficient. Only convection diffusion equation is solved assuming a constant cross flow velocity. The assumption can be justified by the fact that the rejection coefficient is membrane specific and salt specific property. An iterative strategy is implemented to compute the permeate flux from convection diffusion equation and DSPM-DE model. The rejection results for NF90 and NF270 membranes are presented for $NaCl$ salt at different TMPs and bulk concentrations. It is observed that rejection of $NaCl$ is more in the case of NF90 than in NF270. This is due to the steric hindrance NF90 offering to ions because of its smaller pore size. It is observed that rejection decreases as the solution becomes more concentrated. The influence of pore dielectric constant on rejection is explained with the example of $NaCl$ for two different membranes.

All the different models implemented in present work namely cake formation in micro-filtration, cake formation in nano-filtration, osmotic pressure model and rejection model fundamentally used same approach in solving the problem. Resolving fluid by Navier Stokes equations and solute by convection diffusion equation. The techniques employed to do so are chosen to increase the applicability of the

model. This approach of solving membrane filtration in a couple manner can be used to develop the generic models with wide applicability and can be used as black boxes in industry. The excellent results obtained for different cases shows the vast range of applicability of the model and further research can be made to look into the drawbacks stated.

Appendix A

Scaling in LBM

The variables in the LB schemes are often scaled to lattice units. The relation between two system for common variables used in LB simulation are outlined below.

TABLE A.1: Relation between lattice units and physical units

Variables	Physical units	Lattice units	Relationship
Density	$\rho = \rho_0$	$\bar{\rho} = 1$	$\rho = \rho_0 \bar{\rho}$
Density function	$f_i = \rho / w_i$	$\bar{f}_i = 1/w_i$	$f_i = \rho_0 \bar{f}_i$
Relaxation time	τ	$\bar{\tau}$	$\tau = \bar{\tau} \Delta t$
Lattice spacing	δx	$\bar{\Delta} x = 1$	-
Time step	δt	$\bar{\Delta} t = 1$	-
Lattice speed	$c = \frac{\Delta x}{\Delta t}$	$\bar{c} = 1$	-
Viscosity	$\nu = \frac{1}{3}\left(\bar{\tau} - \frac{1}{2}\right)\frac{\Delta x^2}{\Delta t}$	$\bar{\nu} = \frac{1}{3}\left(\bar{\tau} - \frac{1}{2}\right)$	$\nu = \bar{\nu}\frac{\Delta x^2}{\Delta t}$

Appendix B

Numerical solution to OZ integral equation

The three dimensional correlation functions can be treated as one dimensional functions for radially symmetric interaction potentials. DLVO interaction potential is radially symmetric in nature and hence the symmetric function $\gamma(r)$ can be expressed as one dimensional sine transform

$$\gamma(r) = \frac{1}{2\pi^2} \int_0^\infty k^2 \tilde{\gamma}(k) \frac{sin(kr)}{kr} dk \tag{B.1}$$

and its corresponding inverse is

$$\tilde{\gamma}(k) = 4\pi \int_0^\infty r^2 \gamma(r) \frac{sin(kr)}{kr} dr \tag{B.2}$$

where tilde function denotes the Fourier transformed function. Now the numerical techniqu to solve OZ integral equation using the Fourier transforms Eq.B.1, B.2 is discussed below

Let r be the real space and k be te Fourier space. The real space is discretized into N intervals with Δr as step size. The corresponding step size in Fourier space, Δk will be

$$\Delta k = \frac{\pi}{N\Delta r} \tag{B.3}$$

The discrete Fourier transform pair corresponding to Eq.B.1 and B.2 are given by

$$\tilde{F}_j = 4\pi\Delta r \sum_{i=1}^{N-1} F_i sin\left(\frac{\pi ij}{N}\right), j = 1, 2, ..., N-1 \tag{B.4a}$$

$$F_i = \frac{\Delta k}{2\pi^2} \sum_{j=1}^{N-1} \tilde{F}_j sin\left(\frac{\pi ij}{N}\right), i = 1, 2, ..., N-1 \tag{B.4b}$$

The Fourier transformations can be computed by fast Fourier transforms. In this work, MATLAB^{TM}is used to compute fast Fourier transforms.

Different correlation functions are expressed as $C_i = r_i c_i$, $H_i = r_i h_i$ and $\Gamma_i = r_i \gamma_i$ where $\gamma_i = h_i - c_i$. Using HNC closure

$$C_i = r_i \left[exp\left(-\beta E(r) + \frac{\Gamma_i}{r_i}\right) - \frac{\Gamma_i}{r_i} - 1\right] \tag{B.5}$$

The Fourier transformation of the OZ integral yields the following relation

$$\tilde{\Gamma}_j = \frac{n\tilde{C}_j^2}{k_j - n\tilde{C}_j} \tag{B.6}$$

In Eq.B.6, n is the number density of the solute particles. The solution procedure starts with a guessed value for Γ_i and C_i can be computed using Eq.B.5 with the knowledge of interaction potential $E(r)$. The Fourier transformed function of C_i is calculated using fast Fourier transforms and $\tilde{\Gamma}_j$ is calculated from Eq.B.6. The computed $\tilde{\Gamma}_j$ in Fourier space is inverse transformed back to real space and compared to the old estimate. This is done until convergence criterion is met at every point in real space r. The new guess at the end of each iteration can be under relaxed to obtain a faster convergence rate.

$$\Gamma_i^{m+1} = \omega\Gamma_i^{m-1} + (1-\omega)\Gamma_i^m \tag{B.7}$$

where in Eq.B.7, m is the iteration number and ω is the weight and its value should be between 0 and 1. After the method has converged, γ_i and h_i can be computed by

Γ_i and C_i. The radial distribution function is related to pair correlation function as follows

$$g_i = 1 + h_i \tag{B.8}$$

Bibliography

[1] Lianfa Song. Flux decline in crossflow microfiltration and ultrafiltration: mechanisms and modeling of membrane fouling. *Journal of Membrane Science*, 139(2):183–200, February 1998.

[2] S. Nakao Tsuru, T. and S. Kimura. Calculation of ion rejection by extended nemst-planck equation with charged reverse osmosis membranes for single and mixed electrolyte solutions. *Journal of Chemical Engineering*, 24(4):511–517, January 1991.

[3] R. Bowen, W. and H. Mukhtar. Characterisation and prediction of separation performance of nanofiltration membranes. *Journal of Membrane Science*, 112 (2):263–274, April 1996.

[4] R. A. Mohammad Bowen, W. and N. Hilal. Characterisation of nanofiltration membranes for predieflve purposes use of salts, uncharged solutes and atomic force microscopy. *Journal of Membrane Science*, 126(1):91–105, April 1997.

[5] J. C. Chen Bhattacharjee, S. and M. Elimelech. Couple model of concentration polarisation and pore transport in crossflow nanofiltration. *American Institute of Chemical Engineers*, 47(12):2733–2745, December 2001.

[6] M. Marion B.H. Jeong E. M. V. Hoek Kim, S. Crossflow membrane filtration of interacting nanoparticle suspensions. *Journal of Membrane Science*, 284 (1):361–372, November 2006.

[7] A. S. Kim M. Elimelech Bhattacharjee, S. Concentration polarisation of interacting solute particles in cross flow membrane filtration. *Journal of Colloidal and Interface Science*, 212(1):81–99, April 1999.

[8] M.T. Morrissey Huang, L. Finite element analysis as a tool for crossflow membrane filter simulation. *Journal of Membrane Science*, 155(1):19–30, March 1999.

[9] M.M. Clark Lee, Y. A numerical model of steady-state permeate flux during cross-flow ultrafiltration. *Desalination*, 109(3):241–251, June 1997.

[10] V.A. Barker O. Hassager Hansen, M. Spectral element simulation of ultrafiltration. *Chemical Engineering Science*, 53(17):3099–3115, September 1998.

[11] V.A. Semiao M.N. de Pinho Geraldes, V.M. Nanofiltration mass transfer at the entrance region of a slit laminar flow. *Industrial and Engineering Chemistry Research*, 37(12):4792–4800, November 1998.

[12] A. Bastiaanse J. Swarts G. Brans R.G.M. van der Sman R.M. Boom Kromkamp, J. A suspension flow model for hydrodynamics and concentration polarisation in crossflow microfiltration. *Journal of Membrane Science*, 253 (1):67–79, May 2005.

[13] Li-Shi Luo X. He. Theory of latttice boltzmann method: From the boltzmann equation to the lattice equation. *Physical Review E*, 56(6):6811–6815, December 1997.

[14] M. Krook P. L. Bhatnagar, E. P. Gross. A model for collision process in gases. i. small amplitude processes in charged and neutral one component systems. *Physical Review E*, 94(3):511–525, May 1954.

[15] X. He Q. Zou. Pressure and velocity boundary condition for the lattice boltzmann methods. *Journal Physics of Fluids*, 9(6):1591–1598, June 1997.

[16] P. Lallemand M. Bouzidi, M. Firdaouss. Momentum transfer of a lattice boltzmann fluid with boundaries. *Journal Physics of Fluids*, 13(11):3452–3459, June 2001.

[17] Michael Junk and Zhaoxia Yang. One-point boundary condition for the lattice boltzmann method. *Physical Review E*, 72(6):066701, December 2005.

[18] R. Zhang H. Chen Y. Li, R. Shock. Numerical study of flow past an impulsively started cylinder by the lattice-boltzmann method. *Journal of Fluid Mechanics*, 519:273–300, November 2004.

[19] D. Hanel O. Filipova. Boundary-fitting and local grid refinement for lattice-bgk models. *International Journal of Modern Physics C*, 9(8):1271–1279, 1998.

[20] W. Shyy R. Mei, Li-Shi Luo. An accurate curved boundary treatment in the lattice boltzmann method. *Journal of Computational Physics*, 155(2):307 – 330, 1999.

[21] D. M. Freed. Lattice-boltzmann method for macroscopic porous media modeling. *International Journal of Modern Physics C*, 9(8):1491–1498, 1998.

[22] F. R. Phelan Jr. M. A. A. Spaid. Lattice boltzmann methods for modeling microscale flow in fibrous porous media. *Physics of Fluids*, 9(9):2468–2474, 1997.

[23] HSL. A collection of fortran codes for large scale scientific computations, http://www.hsl.rl.ac.uk/.

[24] J. K. Reid I. S. Duff. The multifrontal solution of unsymetric sets of linear equations. *SIAM J. Sci. and Stat. Computational*, 5(3):633–641, 1984.

[25] R. H. Davis C. A. Romero. Global model of crossflow microfiltration based on hydrodynamic particle diffusion. *Journal of Membrane Science*, 39(2): 157–185, 1988.

[26] J. Moon B. Kwon J. Cho, I. S. Kim. Determining brownian and shear induced diffusivity of nano- and micro- particles for sustainable membrane filtration. *Desalination*, 188(1):213–216, 2006.

[27] I. R. McDonald J. P. Hansen. Theory of simple liquids. *Academic Press, London*, 1976.

[28] M. N. Pinho V. Geraldes, V. Semiao. Flow and mass transfer modelling of nanofiltration. *Journal of Membrane Science*, 191(1):109–128, 2001.

[29] C. Y. Shin U. Ghia, K. N. Ghia. High-re solutions for incompressible flow using navier-stokes equations and a multigrid method. *Journal of Computational Physics*, 48(1):387–411, 1982.

[30] M. Elimelech S. Hong, R. S. Faibish. Kinetics of permeate flux decline in crossflow membrane filtration of colloidal suspensions. *Journal of Colloid and Interface Science*, 196:267–277, 1997.

[31] B. S. Garbow K. E. Hillstrom J. J. More, D. C. Sorensen. The minpack project, in sources and development of mathematical software. *Prentice-Hall*, pages 88–111, 1984.

[32] M. J. D. Powell. A hybrid method for nonlinear equations. In P. Rabinowitz, editor, *Numerical methods for Nonlinear algebraic equations*. Gordon and Breach, 1970.

[33] H. Al-Zoubi N. A. Darwish A. W. Mohammad, N. Hilal. Prediction of permeate fluxes and rejections of highly concentrayed salts in nanofiltration membranes. *Journal of Membrane Science*, 196:289–300, 1997.